

WAVE – CURRENT– FLOATING STRUCTURE INTERACTION STUDY: UNIFORM
FLOW MODEL EXTENSION AND ITS COMPARISON WITH FULLY NONLINEAR
SIMULATIONS

A Dissertation

by

FARID PUTRA BAKTI

Submitted to the Office of Graduate and Professional Studies of
Texas A&M University
in partial fulfillment of the requirements for the degree of

DOCTOR OF PHILOSOPHY

Chair of Committee,	Moo-Hyun Kim
Committee Members,	Jeffrey M. Falzarano
	HeonYong Kang
	Alan B. Palazzolo
Head of Department,	Sharath Girimaji

December 2020

Major Subject: Ocean Engineering

Copyright 2020 Farid Putra Bakti

ABSTRACT

The wave-current (or wave-forward speed) interaction study is an effort to incorporate essential coupling effects between the unsteady waves problem and the steady flow problem into the floating structure's dynamic. The linear solution that only considers the coupling effect with the uniform flow is still considered the most practical way of incorporating the interaction effect. This so-called Uniform Flow (UF) approximation model is valid for a slender body under relatively low current speed. By considering the UF approximation, the interaction effect can be reduced to the solution of a wave-only problem (i.e., zero speed solution) and its correction factors. This approximation is implemented into the existing in-house 3-D BEM code in the frequency domain. Noting the UF approximation model's versatility and simplicity, we extend the existing model to cover a broader range of applications.

First, a practical approach to incorporate forward speed and hydro-elasticity effect in the frequency domain was developed. By utilizing the discrete-module-beam (DMB) method, flexible structures are partitioned into multiple rigid bodies connected by beam elements. The forward speed effect is taken into consideration in the multi-body hydrodynamics through the UF-based simplified method. The present numerical results compare well with published experimental and FEM-BEM coupling method. Several parametric studies were also conducted to quantify the forward speed effect on the structure's elastic behavior.

Then, a formulation for the second-order difference-frequency wave load in the presence of a steady uniform current is presented. The free-surface integral is not included in evaluating the difference-frequency force quadratic transfer function (QTF) considering its relatively negligible

contribution compared to other terms, significantly reducing the computational cost. The importance of properly incorporating the uniform flow effects into both the boundary value problem and the force formulation was underscored even for the small uniform flow speed.

Finally, all of the results except for the hydro elasticity study were compared against the completely nonlinear CFD method. The CFD results show several phenomena not captured by the BEM, such as the Kelvin ship's wave, nonlinear body motion, and breaking waves. However, due to its lower computation requirements, BEM is still preferred in the majority of cases.

DEDICATION

This dissertation is dedicated to my mother, my sisters, and my brother. Also, to my father, Dr. HangTuah Salim, who taught me the importance of curiosity and education, who still serves as a source of motivation even after he passed, whose name is always in my prayer.

And to all students out there who are anxious about the outcome of their struggle, always know that this is only one fragment of a larger picture in our life.

ACKNOWLEDGMENTS

First and foremost, my gratitude goes to my committee chair, Dr. Moo-Hyun Kim, for his support, guidance, and countless scholarly advice. I will not be able to finish this work without his vast source of knowledge, expertise, and patience to guide my research journey every step of the way ever since I was just a fresh graduate with minimum research experience.

I am thankful to my committee members. Dr. HeonYong Kang, who was always there to provide technical support during the development of the codes, Dr. Jeffrey Falzarano, whose papers and works provided the fundamental insights in which this work was built, and Dr. Alan Palazzolo, whose courses has a significant influence on my understanding of dynamic's problem.

My gratitude goes to my colleagues, especially Dr. Chungkuk Jin, with whom I write many papers together and, in doing so, has driven me to be productive in the final phase of my study. I also extend my gratitude to Dr. Amitava Guha, Dr. Donghwan Lee, and Dr. Y.H (Allen) Liu, whose works and insights constitute a significant part of this study. I thank Dr. Arcandra Tahar and Dr. Prahoro Nurjahyo for their recommendation in getting into my current research group and for their countless career, academics, and research advice. Also, thanks to the Ocean and Civil Engineering Staffs, especially Lisa Wilson, Caleb Mullins, and Laura Byrd, who has always been very helpful around the office.

I am thankful to the Indonesia Endowment Fund for Education or also known as LPDP (Lembaga Pengelola Dana Pendidikan) that supported me during the majority of my study. I am also thankful for the wider Indonesian community in the USA, especially in College Station, who

always treated me like family, provided much needed emotional support, and made me feel at home.

Above all, I am grateful to my parents, sisters, brother, and other family members, whose faith in me makes me believe in myself. The unwavering supports they provided from afar and the warmth they provided whenever I come home helped me countless times to overcome the hurdles in my study. Last but not least, I would like to specifically thank Raysha, whose faith, encouragements, motivational talks, and many other countless supports kept me motivated and made it easier to overcome all the hardships.

CONTRIBUTORS AND FUNDING SOURCES

Contributors

This work was supported by a dissertation committee consisting of Prof. Moo-Hyun Kim [advisor], Prof Jeffrey Falzarano of the Department of Ocean Engineering, Dr. HeonYong Kang of the Department of Ocean Engineering, and Prof. Allan Palazzolo of the Department of Mechanical Engineering.

The original 3-D BEM code for linear wave radiation and diffraction problems without the uniform flow interaction effect was originally developed by Dr. Donghwan Lee (2005). The hydroelasticity program for wave only case and its validations in Section 3 was developed in tandem with Dr. Chungkuk Jin. The Wigley ship hull data in Section 2 were partially provided by Dr. Amitava Guha.

Funding Sources

Graduate study was partially supported by the Indonesia Endowment Fund for Education or also known as LPDP (Lembaga Pengelola Dana Pendidikan) grant No: PRJ-4038/LPDP.3/2016.

TABLE OF CONTENTS

	Page
ABSTRACT.....	ii
DEDICATION.....	iv
ACKNOWLEDGMENTS	v
CONTRIBUTORS AND FUNDING SOURCES	vii
TABLE OF CONTENTS.....	viii
LIST OF FIGURES	xi
LIST OF TABLES.....	xv
1. INTRODUCTION.....	1
1.1. Summary	1
1.2. General Description of the Wave-Uniform Flow Interaction Problem with Linearized Interaction Effect	4
1.3. References	11
2. THE FIRST ORDER WAVE-UNIFORM FLOW INTERACTION PROBLEM	12
2.1. Background and Literature Review.....	12
2.2. Methodology	15
2.2.1. The First Order Boundary Value Problem	15
2.2.2. 1st Order Hydrodynamic Loading and Equation of Motion	19
2.2.3. Numerical Implementation.....	22
2.3. Case Study.....	27
2.3.1. Case Definition	27
2.3.2. Results and Discussions.....	29
2.4. Summary	33
2.5. References	34
3. PRACTICAL APPROACH OF LINEAR HYDRO-ELASTICITY EFFECT ON VESSEL WITH FORWARD SPEED IN THE FREQUENCY DOMAIN	37
3.1. Background and Literature Review.....	37
3.2. Structural Dynamics and Hydro-elastic Coupling	41

3.2.1. Discrete Body Hydroelasticity Method (DBM)	41
3.2.2. Equation of Motions	45
3.2.3. Modal Analysis.....	46
3.3. Wave and Uniform Current Hydrodynamics	48
3.3.1. Boundary Value Problem for Multi Body Wave Interaction with Uniform Flow	48
3.3.2. Hydrodynamic Forces and Coefficients	52
3.4. Validations	54
3.4.1. Case Definition.....	54
3.4.2. Validation of DMB Hydro-elasticity Model for Zero Forward Speed Case	59
3.4.3. Validation of DMB Hydro-elasticity Model with Forward Speed Case	61
3.5. Parametric Study on the Forward Speed Effect on the Ship Hydro-elastic Behavior ...	63
3.5.1. Forward Speed Effect on the Modal Characteristics	63
3.5.2. Forward Speed Effect on the Vertical Bending Moment	66
3.5.3. Forward Speed Effect on Hydro-elastic Response in Random Waves	69
3.5.4. Additional Demonstration of the Present Method's Practicality: damaged hull simulation	73
3.6. Conclusions	75
3.7. References	77
4. SECOND-ORDER DIFFERENCE-FREQUENCY WAVE LOADS ON A FLOATING BODY IN UNIFORM CURRENT	82
4.1. Background and Literature Review.....	82
4.2. The Second Order Problem	84
4.3. The Second-Order Wave Loading.....	91
4.4. Implementation.....	94
4.5. Validation	97
4.6. Case Study.....	101
4.7. Comparisons with Other Approximation Methods	105
4.8. Conclusions	111
4.9. References	112
5. RANS CFD SIMULATION OF WAVE-UNIFORM CURRENT INTERACTION WITH SLENDER BODY	116
5.1. Background and Literature Review.....	116
5.2. Theory and Implementations.....	117
5.2.1. Navier-Stokes Equation.....	117
5.2.2. Reynold Averaged Navier-Stokes and Turbulence Closure Model	118
5.2.3. Volume of Fluid	123
5.2.4. Boundary and Initial Condition	125
5.2.5. Wave Forcing Zone	127
5.2.6. Overset Mesh and Dynamic Fluid-Body Interaction	128
5.2.7. Time Stepping Considerations	131
5.2.8. Computational Domain and Meshing Considerations.....	132
5.3. Case Definition.....	134

5.4. Results and Discussion.....	136
5.4.1. Wave Height Calibration.....	136
5.4.2. Uniform Flow Problem	137
5.4.3. Wave and Uniform Flow Interaction Problem	138
5.5. Conclusion.....	144
5.6. References	144
6. GENERAL CONCLUSIONS.....	147

LIST OF FIGURES

	Page
Fig. 1.1. Description of the coordinate systems.....	5
Fig. 1.2. Illustration of wave-forward speed problem and wave-current interaction problem interchangeability.....	6
Fig. 2.1. Force amplitude (top) and phase (bottom) validation of the present study against similar approach from ref.[23,25] and experiment data from ref.[31] for slender Wigley hull with $Fn = 0.2$	29
Fig. 2.2. RAO amplitude (top) and phase (bottom) validation of the present study against similar approach from ref.[23,25] and experiment data from ref.[31] for slender Wigley hull with $Fn = 0.2$	30
Fig. 2.3. Force amplitude (top) and phase (bottom) validation of the present study against similar approach from ref.[23,25] and experiment data from ref.[31] for blunt Wigley hull with $Fn = 0.2$	31
Fig. 2.4. RAO amplitude (top) and phase (bottom) validation of the present study against similar approach from ref.[23,25] and experiment data from ref.[31] for blunt Wigley hull with $Fn = 0.2$	32
Fig. 2.5. Comparison between the UF approximations with weakly nonlinear time domain rankine panel UF BEM from ref.[14].....	33
Fig. 3.1. Illustration of Discrete Module Beam (DMB) method	43
Fig. 3.2. Illustration of bending moment on DMB method	46
Fig. 3.3. Automated iteration method to solve the “wet” modal characteristics	48
Fig. 3.4. Shallow-draft barge shape as defined in Yago & Endo [41].....	55
Fig. 3.5. Wigley hull shape as defined in Riggs et. al. [42].....	56
Fig. 3.6. Cross sections of the structures, and geometric properties definitions	58
Fig. 3.7. Vertical displacement and bending moment validation for shallow barge case	59

Fig. 3.8. Wigley hull hydro-elastic model comparisons for zero forward speed case. The FEM results are from ref. [19], while the modal superposition results are from ref. [42]	61
Fig. 3.9. Elasticity effect with forward speed with respect to the rigid-body base of [19]	63
Fig. 3.10. The forward-speed and water-contact effects on the mode shapes of Wigley hull.....	64
Fig. 3.11. The forward speed effect on the Wigley hull added mass (subscript index = mode, superscript index=section; superscript 1,2 means hydrodynamic interaction between section 1 and 2; subscript 5,3 means pitch-heave mode coupling).....	65
Fig. 3.12. Vertical bending moments of Wigley hull depending on the wave length, location of the ship's section, and forward speed	67
Fig. 3.13. Vertical bending moments along the length of Wigley hull for various wave lengths and forward speeds	68
Fig. 3.14. Two wave spectra used in random wave simulation	69
Fig. 3.15. Three consecutive time series snapshots of the Wigley hull's maximum M_y and vertical displacements for various forward speeds and two different wave spectra	71
Fig. 3.16. Time series of bending moments at mid-ship with (right) and without (left) forward speed in swell sea.....	72
Fig. 3.17. The damaged hull effect on the wet modes of Wigley hull.....	73
Fig. 3.18. Time series of bending moments at mid-ship with (right) and without (left) forward speed and with (red) and without (blue) damage in operational sea	75
Fig. 3.19. Frequency domain analysis of bending moments at mid-ship with (right) and without (left) forward speed and with (red) and without (blue) damage in operational sea.....	75
Fig. 4.1. Hull shape of the Wigley I (left) and Wigley II (right)	98
Fig. 4.2. Amplitudes comparisons of the difference frequency force and moment QTFs for Wigley II (Blunt), considering the free surface integral (bullets) and without free surface integral (solid lines)	99
Fig. 4.3. Validation of the main-diagonal QTFs with forward speed. EUT results are from ref.[30], MDLHydro results are from ref.[37], and Experiment results are from ref.[36].....	100

Fig. 4.4. The uniform flow effect on the complete QTF of the total wave loading of Wigley I.....	102
Fig. 4.5. The uniform flow effect on the complete QTF of the total wave loading of Wigley II.....	103
Fig. 4.6. Wigley II – uniform flow effect on difference frequency surge force components and total exciting force.....	104
Fig. 4.7. Wigley II – uniform flow effect on difference frequency heave force components and total exciting force.....	104
Fig. 4.8. Wigley II – uniform flow effect on difference frequency pitch moment components and total exciting force.....	105
Fig. 4.9. Main diagonal comparisons of the difference frequency surge QTF between the Aranha’s method and the present study	106
Fig. 4.10. Comparisons of the off-diagonal difference-frequency QTFs between various approximation methods – surge of Wigley II hull.....	108
Fig. 4.11. Comparisons of the off-diagonal difference-frequency QTFs between various approximation methods - heave of Wigley II hull.....	109
Fig. 4.12. Comparisons of the off-diagonal difference-frequency QTFs between various approximation methods - pitch of Wigley II hull	109
Fig. 4.13. Irregular wave’s spectra and the corresponding slowly varying force power spectra density	110
Fig. 4.14. Time series comparison between the present method, and Newman’s approximation method.....	110
Fig. 5.1. Variables description in RANS formulation	119
Fig. 5.2. Description of boundary layer	121
Fig. 5.3. First cell definition with regards to the computed y value	123
Fig. 5.4. Grid requirements in VOF method.....	125
Fig. 5.5. Boundary conditions.....	126
Fig. 5.6. Overset mesh cell type	130

Fig. 5.7. Computational domain	132
Fig. 5.8. Mesh refinement regions	133
Fig. 5.9. Calibration of the simulated wave's height and period.....	136
Fig. 5.10. Steady waves (Kelvin-ship wave) pattern illustration (Tow Case).....	137
Fig. 5.11. Steady waves run up along the Wigley hull. Experiment result is from ref.[22].....	138
Fig. 5.12. Wave's profile when the body is at the wave's peak for $\lambda/L = 2$, without (top) and with uniform flow (bottom) effect.....	139
Fig. 5.13. Forces and moment time series for $\lambda/L=2$. Experiment result is from ref.[22].....	140
Fig. 5.14. Motion comparisons between the present CFD simulation with the present BEM method and experiment results from ref.[22].....	141
Fig. 5.15. Non-linearity in surge force time series for unrestrained heave and pitch for $\lambda/L=1.25$	141
Fig. 5.16. Motion visualization comparison between wave only case (left) and wave with uniform flow case (right) for $\lambda/L = 1.25$	142
Fig. 5.17. Surge drift force for $Fn = 0.0$ case. Experiment result is from ref.[22].....	143
Fig. 5.18. Surge drift force for $Fn = 0.2$ case. Experiment result is from ref.[22].....	143

LIST OF TABLES

	Page
Table 2.1. The 0th and 1st order variables	15
Table 2.2. Differences between potential formulations Vs. source distribution formulation	25
Table 2.3. Validation and preliminary result cases	28
Table 3.1. Summary of differences between the reference [19] and present methods	41
Table 3.2. Main particulars of the shallow-draft barge case	55
Table 3.3. Main particulars of Wigley hull case	56
Table 3.4. Equivalent geometry for equivalent beam model	58
Table 3.5. Dry natural period comparisons between FEM model and equivalent beam model.....	59
Table 3.6. The forward-speed and water-contact effects on the natural periods of Wigley hull	64
Table 3.7. Statistical values from the random wave simulation results	70
Table 3.8. The damaged hull effect on the wet natural periods of Wigley hull.....	73
Table 4.1. The 2nd order variables	85
Table 4.2. Particulars of the Wigley hulls.....	98
Table 4.3. Approximation-methods to calculate the off-diagonal QTFs	108
Table 5.1. Hull's Particulars	134
Table 5.2. Case definitions.....	135
Table 5.3. Recorded wave's height and period for each of λ/L cases.....	137
Table 5.4. Steady displacements	138

1. INTRODUCTION

1.1. Summary

Hydrodynamic problems have long been an important design factor for offshore structures. Wave, current, along with wind forcing are the main forces that are acting on these structures. These forces can be differentiated into two main categories: the Bernoulli pressure-driven forces and the viscous drag forces. For structures with large displacements such as tanker ships, semi-submersibles, and FPSOs, the time-varying inviscid Bernoulli pressure forces exerted by the wave field and the structures' motion typically dominates the dynamics. On the other hand, the steady shear and drag forces from the viscous effect are typically dominated by the ocean current or the relative velocity between a seafaring vessel and its surrounding environments. Common practices in the industry suggested that these two problems to be treated separately. The inviscid forces can be solved in the time or frequency domain using the less expensive potential theory simulation tools, and the viscous forces resolved by utilizing CFD simulation tools or experiments. However, various aspects are not taken into account using these approaches; one of them is the coupled interaction effect between steady uniform flow with the wave field. To address this problem, we developed a potential theory-based Boundary Element Method simulation tool that is able to account for the wave-uniform flow interaction effect at low to moderate speed. We then proposed extensions of the method to improve its applicability to encompass a broader array of problems.

To solve the wave-uniform flow interaction problem, potential theory for inviscid, incompressible, irrotational flow is used as the framework, and the Laplace equation is used as the governing equation. In the steady, Kelvin ship wave problem, Brard [1] consider a linearized free

surface condition where the steady perturbation can be considered small, and therefore its multiplication can be neglected by considering small uniform flow or slender body ($\partial/\partial x \ll \partial/\partial y$ or $\partial/\partial z$) Using the same assumptions, Salvesen et. al., [2] then proposed a uniform flow – wave interaction solution where the multiplication between the steady perturbation and the unsteady potential can be neglected for the rest of the boundary conditions (e.g., body boundary). By considering the linearized boundary value problem, the complexity of the problem is significantly reduced. This so called Neumann-Kelvin problem is referred to as the uniform flow (UF) approximation in this study, due to the lack of the steady perturbation in the final formulation.

The linearized boundary value problem is then solved using the boundary element method (BEM), specifically the free surface green's function BEM. The free surface BEM method uses a Green's function that satisfies all the boundary conditions of the problem, except on the body boundary, which is problem specific. Thus, the free surface Green function significantly reduced computation requirement since the domain discretization is only needed on the body boundary. With additional assumptions, the uniform flow effect can be readily calculated from the zero speed results. Therefore, the UF method can be implemented as a post-processing tool to any fluid-structure interaction simulation code, including the aforementioned frequency domain free surface BEM method. The Uniform flow approximation method's versatility opens up many new possibilities for it to be applied to other linear problems. However, for non-linear problems, the UF approximation needed additional efforts to be implemented since all the non-linear hydrodynamic coefficients do not solely comprise the output from zero uniform flow simulation results. Due to these reasons, the extension of the present UF method to increase its applicability to a broader range of problems poses a challenging and interesting research topic.

This study comprises four different chapters, all of which aim to answer all of the issues posed above. In the second chapter, we will detail the derivation of the linear UF model, highlighting the model's differences with the standard wave diffraction problem and its application to several test cases to validate the results obtained from the in-house simulation tool.

In the third chapter, we explore the possibility of applying the UF model to the linear hydroelasticity problem. This problem is particularly interesting since large seafaring vessels such as Super Tankers typically undergo a noticeable elastic deformation when traveling across the sea. For this problem, the vessel forward speed is hypothesized to affect the elastic deformation and the internal forces of the body. A method was proposed so that the forward speed effect on the hydro elasticity problem can be straightforwardly applied using any standard potential theory simulation tools without any drastic changes. For this reason, the discrete body method was adopted and applied alongside the newly formulated UF model for multibody.

In the fourth chapter, we increase the UF model's application range to solve the second order problem in wave slope while keeping the first-order accuracy in wave-uniform flow interaction. By expanding the Uniform flow approximation up to the second-order and solving the problem in the frequency domain, we can save computational time while expanding the scheme's accuracy. Although several studies have expanded the UF model to include the second-order forces, the second-order QTF formulation, including second-order diffraction in the frequency domain, is still rare. Through this investigation, we can assess the performance of the Uniform flow approximation in various sea conditions.

In the fifth and final chapter, we investigate the wave-current interaction problem using a fully non-linear CFD method. The commercial RANS based CFD code STAR-CCM+ is used. Like in the potential theory, the CFD method can readily calculate the inviscid linear wave-current

interaction problem. On top of that, the CFD can also capture the highly non-linear phenomena such as breaking waves, large motion, and shear forces, all of which are not considered in the UF approximation method. To highlight the non-linearity of the problem, a case of wave exciting force at the pitch resonance frequency is selected. The CFD results are also validated against the corresponding in-house BEM code and experiment data.

To summarize, this study is aimed to extend the application range of the linear wave-uniform flow interaction model while still maintaining its core advantages. This core advantages include its compatibility with the frequency domain – potential theory based – free surface BEM that is relatively straight forward to be applied and computationally less expensive compared to other methods.

1.2. General Description of the Wave-Uniform Flow Interaction Problem with Linearized Interaction Effect

In this study, three different coordinate systems are used. The first is the earth fixed-inertial coordinate system $\mathbf{X} = (X, Y, Z)$, the second is the body fixed-non-inertial coordinate system $\mathbf{x} = (x, y, z)$, and the last is the inertial coordinate system that is fixed to the mean body position or the body position at rest $\bar{\mathbf{x}} = (\bar{x}, \bar{y}, \bar{z})$, as illustrated in Fig. 1.1. The Z , z , and \bar{z} are pointing upwards, with Z_0 defined as the vertical position of the origin of $\bar{\mathbf{x}}$.

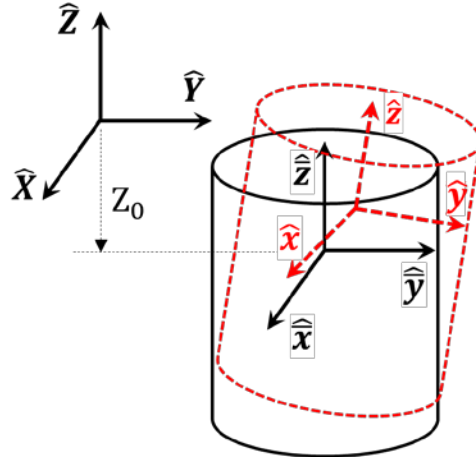


Fig. 1.1. Description of the coordinate systems

Assuming that the fluid is incompressible, irrotational, and inviscid, the fluid's flow can be described with velocity potential function $\Phi(\mathbf{x}, t)$. The relation between the velocity potential and fluid's velocity flow field are:

$$\nabla\Phi(\mathbf{X}, t) = \mathbf{V}(\mathbf{X}, t) = \frac{\partial\Phi}{\partial Z}\hat{\mathbf{i}} + \frac{\partial\Phi}{\partial Y}\hat{\mathbf{j}} + \frac{\partial\Phi}{\partial X}\hat{\mathbf{k}} \quad (1.1)$$

The velocity potential should satisfy the mass conservation, which can be represented as the Laplace equation as below:

$$\nabla^2\Phi = 0 \quad (1.2)$$

The pressure is calculated from the velocity potential, following the unsteady form of Bernoulli's equation:

$$P(\mathbf{X}, t) = -\rho \left(\frac{\partial\Phi}{\partial t} + \frac{1}{2}\nabla\Phi \cdot \nabla\Phi + g\mathbf{X} \cdot \hat{\mathbf{k}} \right) \quad (1.3)$$

where ρ is the fluid density, g is the gravitational acceleration, and $\hat{\mathbf{x}}$ is the position vector in the inertial frame of reference. The exact free surface elevation ζ can be derived by considering gauge pressure $P(z = \zeta, t) = 0$ as below:

$$\zeta(X, Y) = -\frac{1}{g} \left(\frac{\partial \Phi}{\partial t} + \frac{1}{2} \nabla \Phi \cdot \nabla \Phi \right)_{z=\zeta} \quad (1.4)$$

Considering wave and steady flow interaction problem, we decompose the total velocity potential into unsteady wave potential $\phi_w(\mathbf{x}, t)$ and steady potential $\phi_{st}(\mathbf{x})$. The present uniform-flow-based method considers steady potential perturbation caused by the body to be insignificant compared to the uniform flow, such that:

$$\Phi(\mathbf{X}, t) = \phi_w(\mathbf{X}, t) + \phi_{st}(\mathbf{X}) \quad (1.5)$$

$$\phi_{st}(\mathbf{X}) = \phi_{sB}(\mathbf{X}) + \phi_U(\mathbf{X}) = \phi_{sB}(\mathbf{X}) - U\mathbf{X} \quad (1.6)$$

where U , ϕ_U , and ϕ_{sB} , are the uniform flow magnitude uniform flow potential, and the perturbed steady flow potential due to interaction between the uniform flow with the body, respectively. The uniform flow can also be considered as current speed or negative ship speed, as can be seen on Fig. 1.2.

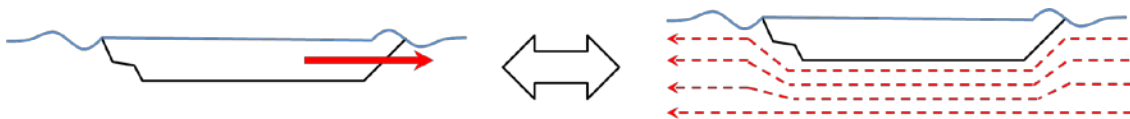


Fig. 1.2. Illustration of wave-forward speed problem and wave-current interaction problem interchangeability

The steady velocity potential satisfies all the appropriate boundary conditions and the Laplace equation. The boundary conditions are then linearized following [1] and [2] by considering slender body ($\partial/\partial x \ll \partial/\partial y$ or $\partial/\partial z$) or small uniform flow. The linearized boundary condition

assumes the steady perturbation to be small, and thus the multiplication between the steady perturbation and the unsteady perturbation (e.g., ϕ_{sB} and ϕ_w) are neglected. This approximation significantly reduces the complexity of the problem at the expense of losing some coupling information between the steady and unsteady solutions. However, in many practical engineering applications, this approximation can still provide meaningful first-cut results, such as in [2-7]. These approximations are referred to as the uniform flow (UF) approximation for the remainder of the study.

For the wave diffraction-radiation problem, the only source of the unsteady potential terms is from the gravity waves and its interaction with the floating body. The total wave potential in eq.(1.5) can further be separated as:

$$\phi_w(\hat{\mathbf{x}}, t) = \phi_I(\hat{\mathbf{x}}) + \phi_S(\hat{\mathbf{x}}) + \phi_R(\hat{\mathbf{x}}) \quad (1.7)$$

$$\phi_R(\hat{\mathbf{x}}, t) = \boldsymbol{\eta} \cdot \boldsymbol{\phi}_r = \sum_{i=1}^6 \eta_i \phi_{ri}(\hat{\mathbf{x}}, t) \quad (1.8)$$

$$\boldsymbol{\eta} = (\eta_1, \eta_2, \dots, \eta_6) = (\boldsymbol{\xi}, \boldsymbol{\alpha}) = (\xi_x, \xi_y, \xi_z, \alpha_x, \alpha_y, \alpha_z) \quad (1.9)$$

where ϕ_I , ϕ_S , ϕ_R , $\boldsymbol{\eta}$, $\boldsymbol{\xi}$, $\boldsymbol{\alpha}$ are the incident wave potential, scattered wave potential, radiated wave potential, the generalized body motion vector, body's translation vector, and body's rotation vector, respectively. The scattered wave potential is for deformed waves by the fixed body. The radiation potential is for wave generated by the body motion.

Assuming small non linearity, the velocity potential at each order with respect to the incident wave's slope ϵ can be obtained by employing the perturbation theory:

$$\Phi = \Phi^{(0)} + \epsilon \Phi^{(1)} + \epsilon^2 \Phi^{(2)} \quad (1.10)$$

The 0th order potential $\Phi^{(0)}$ is associated with the steady potential by the uniform flow. Utilizing separation of variables and assuming harmonic motions, the first and second-order velocity potentials can be expressed by the sum of its harmonic component as follow:

$$\Phi^{(0)}(\hat{\mathbf{x}}, t) = \phi_{\text{st}}(\hat{\mathbf{x}}) = \phi_{\text{sB}}(\mathbf{X}) - \mathbf{U}\mathbf{X} \quad (1.11)$$

$$\Phi^{(1)}(\hat{\mathbf{x}}, t) = \phi_{\text{w}}^{(1)}(\hat{\mathbf{x}}, t) = \text{Re} \sum_{i=1}^N \phi_i(\hat{\mathbf{x}}) e^{i\omega_{e_i} t} \quad (1.12)$$

$$\Phi^{(2)}(\hat{\mathbf{x}}, t) = \phi_{\text{w}}^{(2)}(\hat{\mathbf{x}}, t) = \text{Re} \sum_{i=1}^N \sum_{j=1}^N \left\{ \phi_{ij}^{-}(\hat{\mathbf{x}}) e^{i(\omega_{e_i} - \omega_{e_j})t} + \phi_{ij}^{+}(\hat{\mathbf{x}}) e^{i(\omega_{e_i} + \omega_{e_j})t} \right\} \quad (1.13)$$

where $\phi_i(x)$ is the first order velocity potential, obtained from the 1st order boundary value problem in the presence of the incident wave with a frequency ω_{e_i} . ϕ_{ij}^{-} represents the second-order difference frequency potential and ϕ_{ij}^{+} represents the second-order sum-frequency potential, both are obtained from the 2nd order boundary value problem in the presence of the bichromatic incident wave with a frequency pair of ω_{e_i} and ω_{e_j} . ω_e is the encounter frequency, defined as follow:

$$\omega_e = \omega_0 + kU \cos \beta_{cw} \quad (1.14)$$

where ω_0 , U , k , and β_{cw} is the wave frequency without the presence of the uniform flow, the wavenumber, and the angle between the uniform flow and wave heading, respectively. As an example, if the wave and uniform flow are from the opposite direction, similar to the vessel with a forward speed in following seas ($\beta_{cw} = 180^\circ$), ω_e will be lower than ω_0 . The directional spreading of the incident wave is not considered in this study, and a uni-directional wave is considered for the second-order problem ($\beta_i = \beta_j$). The exact boundary conditions are described as follow:

- Free surface boundary condition:

$$\frac{\partial \Phi}{\partial \mathbf{n}} = \frac{\partial \Phi}{\partial z} = \nabla_h \Phi \cdot \nabla_h \zeta + \frac{\partial \zeta}{\partial t} \quad \text{on } S_F(z = \zeta) \quad (1.15)$$

- Bottom boundary condition:

$$\frac{\partial \Phi}{\partial \mathbf{n}} = \frac{\partial \Phi}{\partial z} = 0 \quad \text{on } S_h(z = -h) \quad (1.16)$$

- Body boundary condition:

$$\frac{\partial \Phi}{\partial \mathbf{n}} = \frac{\partial \mathbf{x}}{\partial t} \cdot \mathbf{n} \quad \text{on } S_B \quad (1.17)$$

- Far-field boundary condition:

$$\lim_{|\mathbf{x}| \rightarrow \infty} \sqrt{|\mathbf{x}|} \left(\frac{\partial}{\partial t} - ik \right) (\Phi_R + \Phi_S) \quad \text{on } S_{|\mathbf{x}| \rightarrow \infty} \quad (1.18)$$

where \mathbf{n} is the unit normal direction of the boundary surface, $\partial \Phi / \partial \mathbf{n} = \nabla \Phi \cdot \mathbf{n}$ is the fluid velocity in the \mathbf{n} direction, and $\nabla_h = \partial / \partial x \hat{\mathbf{i}} + \partial / \partial y \hat{\mathbf{j}}$ is the horizontal gradient vector. Note that even though the far field condition is written as (1.18), it is not exact in the presence of uniform flow.

We define $P(\bar{\mathbf{x}})_{S_B}$ as the pressure on the exact body surface S_B with respect to the inertial frame of reference $\bar{\mathbf{x}}$, such that $\bar{\mathbf{x}} \in S_B$. $P(\bar{\mathbf{x}})_{S_B}$ can be related to the pressure on the body's mean position $P(\mathbf{x})_{S_{B_0}}$ by employing the multivariate Taylor expansion as follow:

$$P(\bar{\mathbf{x}})_{S_B} = P(\mathbf{x})_{S_{B_0}} + (\bar{\mathbf{x}} - \mathbf{x}) \cdot \nabla P(\mathbf{x})_{S_{B_0}} \quad (1.19)$$

Applying the same Taylor expansion on the free surface and the body boundary condition, we can describe the exact free surface with respect to the still water level $z = 0$, and the body boundary with respect to the body's mean position $S_B = S_{B_0}$ as follow:

$$\frac{\partial \Phi}{\partial \mathbf{n}} \Big|_{S_B} = \frac{\partial \Phi}{\partial \mathbf{n}} \Big|_{S_{B_0}} + (\bar{\mathbf{x}} - \mathbf{x}) \cdot \nabla \frac{\partial \Phi}{\partial \mathbf{n}} \Big|_{S_{B_0}} \quad (1.20)$$

$$\begin{aligned}
\zeta(x, y) &= -\frac{1}{g} \left(\frac{\partial \Phi}{\partial t} + \frac{1}{2} \nabla \Phi \cdot \nabla \Phi \right)_{z=\zeta} \\
&= -\frac{1}{g} \left(\frac{\partial \Phi}{\partial t} + \frac{1}{2} \nabla \Phi \cdot \nabla \Phi \right)_{z=0} + \frac{1}{g^2} \left(\frac{\partial \Phi}{\partial t} + \frac{1}{2} \nabla \Phi \cdot \nabla \Phi \right)_{z=0} \frac{\partial}{\partial z} \left(\frac{\partial \Phi}{\partial t} + \frac{1}{2} \nabla \Phi \cdot \nabla \Phi \right)_{z=0}
\end{aligned} \tag{1.21}$$

Forces and moment are calculated by integrating the pressure on the exact body surface up to the exact free surface as follow:

$$\begin{aligned}
\mathbf{F} &= - \iint_{S_B} P \bar{\mathbf{n}} \, dS \\
&\cong \left(\iint_{S_{B0}} dS \right) (P^{(0)} + \epsilon P^{(1)} + \epsilon^2 P^{(2)}) (\bar{\mathbf{n}}^{(0)} + \epsilon \bar{\mathbf{n}}^{(1)} + \epsilon^2 \bar{\mathbf{n}}^{(2)}) + \\
&\quad \left(\int_{wl} dl \int_{\epsilon \zeta_r^{(1)} + \epsilon^2 \zeta_r^{(2)}} dz \right) (P^{(0)} + \epsilon P^{(1)} + \epsilon^2 P^{(2)}) (\bar{\mathbf{N}}^{(0)} + \epsilon \bar{\mathbf{N}}^{(1)} + \epsilon^2 \bar{\mathbf{N}}^{(2)})
\end{aligned} \tag{1.22}$$

$$\begin{aligned}
\mathbf{M} &= - \iint_{S_B} P (\bar{\mathbf{x}} \times \bar{\mathbf{n}}) \, dS \\
&\cong \left(\iint_{S_{B0}} dS \right) (P^{(0)} + \epsilon P^{(1)} + \epsilon^2 P^{(2)}) ((\bar{\mathbf{x}} \times \bar{\mathbf{n}})^{(0)} + \epsilon (\bar{\mathbf{x}} \times \bar{\mathbf{n}})^{(1)} + \epsilon^2 (\bar{\mathbf{x}} \times \bar{\mathbf{n}})^{(2)}) + \\
&\quad \left(\int_{wl} dl \int_{\epsilon \zeta_r^{(1)} + \epsilon^2 \zeta_r^{(2)}} dz \right) (P^{(0)} + \epsilon P^{(1)} + \epsilon^2 P^{(2)}) ((\bar{\mathbf{x}} \times \bar{\mathbf{N}})^{(0)} + \epsilon (\bar{\mathbf{x}} \times \bar{\mathbf{N}})^{(1)} + \epsilon^2 (\bar{\mathbf{x}} \times \bar{\mathbf{N}})^{(2)})
\end{aligned} \tag{1.23}$$

where $\zeta_r = \zeta - \bar{z}$ is the relative wave elevation, $\bar{\mathbf{n}}$ is the body's unit-normal vector in the inertial frame of reference $\bar{\mathbf{x}}$, \mathbf{n} is the body's unit-normal vector in the body-fixed frame of reference \mathbf{x} , and $\bar{\mathbf{N}} = \bar{\mathbf{n}} / \sqrt{1 - \bar{n}_z}$. Note that for the body-fixed frame of reference, $\mathbf{n}^{(0)} = \mathbf{n}^{(1)} = \mathbf{n}^{(2)} = \mathbf{n}$. The waterline integral is included to account for the instantaneous wave elevation with respect to the undisturbed sea level and instantaneous body position. For shorthand writing purposes, we also introduce the generalized force vector \mathbf{F}' and unit-normal vector \mathbf{n}' that is defined as:

$$\mathbf{F}' = (F'_1, F'_2, \dots, F'_6) = (\mathbf{F}, \mathbf{M}) \tag{1.24}$$

$$\mathbf{n}' = (n'_1, n'_2, \dots, n'_6) = (\mathbf{n}, \mathbf{n} \times \mathbf{x}) = (n_x, n_y, n_z, \{n_y z - n_z y\}, \{n_z x - n_x z\}, \{n_x y - n_y x\}) \quad (1.25)$$

To solve the exact-non-linear boundary value problem in the frequency domain, we decompose the problem into each order of non-linearity with respect to ϵ and successively solve it from the lowest to the highest order. The linear solution (1st order in wave slope and in wave-uniform flow interaction) and its extension to the hydroelasticity problem is explained in the 2nd and 3rd section. While the weak second order solution (2nd order in wave slope and 1st order in wave-uniform flow interaction) is explained in the 4th section.

1.3. References

- [1] R. Brard, "Representation of a given ship form by singularity distributions when the boundary condition on the free surface is linearized," *Journal of Ship Research*, vol. 16, no. 1, pp. 79-92, 1972.
- [2] N. Salvesen, E. Tuck, and O. Faltinsen, "Ship motions and sea loads," vol. 78, ed, 1970, pp. 250-287.
- [3] R. F. Beck and A. E. Loken, "Three-dimensional effects in ship relative-motion problems," *Journal of Ship Research*, vol. 33, no. 4, pp. 261-268, 1989.
- [4] M. Kashiwagi, "Prediction of Surge and its Effect on Added Resistance by Means of the Enhanced Unified Theory," *Trans West-Japan Society of Naval Architects*, no. 89, pp. 77-89, 1995.
- [5] A. Papanikolaou and T. Schellin, "A three-dimensional panel method for motions and loads of ships with forward speed," *Ship Technology Research (Schiffstechnik)*, vol. 39, no. 4, pp. 145-155, 1992.
- [6] A. Guha and J. Falzarano, "The effect of hull emergence angle on the near field formulation of added resistance," *Ocean Engineering*, vol. 105, pp. 10-24, 2015.
- [7] A. Guha and J. Falzarano, "Estimation of hydrodynamic forces and motion of ships with steady forward speed," *International Shipbuilding Progress*, vol. 62, no. 3-4, pp. 113-138, 2016.

2. THE FIRST ORDER WAVE-UNIFORM FLOW INTERACTION

PROBLEM

2.1. Background and Literature Review

The wave-current interaction (or wave-forward speed interaction) study is an effort to incorporate important features of the coupling effect between the wave diffraction and uniform flow problem into floating structure's dynamic analysis. Hirdaris et. al. [1] shows in his study that out of 175 papers that are used as references, roughly 20% of them are related to the wave-forward speed or wave-current interaction problem, signifying its importance in both the industry and in academia. Wave uniform flow interaction can become an important design factor through several ways, including: the change of magnitude of exciting forces, hydrodynamic damping, added mass, RAO, and added resistance.

The wave-uniform flow problems can be resolved through numerical hydrodynamic simulation considering different level of fidelities. Several attempts were done to try to take into account both the linear and non-linear wave-uniform flow coupling terms on both the free surface boundary condition and the body boundary condition. New free surface green function were developed to take into account the uniform flow effect to the free surface boundary condition either in the frequency domain [2-5], or the time domain [6, 7]. These green function will preserve the advantages of having the free surface green function where discretization is only needed on the body surface. However, due to the high oscillation tendency on the free surface green function, the complexity of integrating the value, and non-reliable result when there is a ship wave propagating

upstream from the ship, several additional numerical technique and additional precautions are needed when applying these green functions.

Several studies resort to the application of the rankine panel method (RPM) to resolve the coupled wave-uniform flow boundary value problem, where the green function is conditioned to satisfy all the boundary condition except on the free surface and the body surface boundary [8-10]. This method is highly compatible with the time domain method, and non-linearity effect such as steady Kelvin ship wave effect on the unsteady diffraction problem can be simulated [8, 10]. Variation of this method can be found on ref. [11, 12], where rankine source function is placed on the offset from the boundary surfaces to avoid singularity from the rankine source. By using the RPM method in the time domain, accurate results for non-slender structure such as floating offshore platform can be achieved [13-15]. Despite the aforementioned benefits of using time domain or rankine panel method, the drawbacks of higher computational time due to time stepping and additional free surface panels persist.

Timman & Newman [16] and Ogilvie & Tuck [17] shows that the wave-uniform flow coupling effect on the body boundary condition can be formulated into the well-known “m” terms. In addition, Ogilvie & Tuck [17] shows the equation for the wave-forward speed interaction where the steady perturbation to the uniform flow is described as the double body potential and linearized by considering small uniform flow magnitude. On the other hand, Brard et. al. [18], introduced an approximate method where the boundary condition in the steady wave (e.g., Kelvin’s ship waves) and uniform flow interaction problems are linearized by considering negligible interaction with the steady perturbation. This so called Neumann-Kelvin problem can be satisfied when body is either thin or slender, subjected to small uniform flow, or combinations of the two [19-24]. Salvesen [19], then applied the same Neumann-Kelvin approximation to the unsteady waves

problem using the 2D strip theory. In this study, the same linearized wave-uniform flow coupling problem as in the Brard et. al. [18] and Salvesen [19] is called as the Uniform Flow (UF) approximation, due to only uniform flow coupling effect with the wave's perturbation is considered.

The resulting hydrodynamics coefficient in the UF approximation is found to be only depends on the zero speed solution and correction factors that also only depends on zero speed solutions [19]. From here, the advantages of using UF approximation is clear, that is, it can account for the linear wave-uniform flow interaction effect by using the zero-speed hydrodynamic computation tools. Even though UF approximation is simpler compared to the double body linearization, Kim & Kim [22] shows in his study that UF approximation generally have comparable performance to its double body approximation counterpart.

Loken [21], Papanikolaou [16] and Guha [23, 25] further increase the robustness of the Salvesen [19] UF approximation method, by applying it in the potential flow based 3D boundary element method (BEM) in the frequency domain [26]. The study take advantage of the free surface green function where the green function is conditioned to satisfy all the governing and boundary equation except the body boundary condition. By doing this, the computation cost reduced greatly because no time integration is needed, and discretization is only needed on the body surface. On this method, the coupling terms between the wave and uniform flow is ignored by considering thin slender body condition, so that the free surface green function for zero uniform flow case can still be used. The linear frequency domain BEM can also be coupled with either RANS or time domain BEM simulation tools to take into account weak nonlinearity that come from the incident wave and hydrostatic forces [27, 28].

Considering the versatility and practicality of the UF approximation method, this study will focus on the possibilities of extending the frequency domain UF 3D free surface BEM to wider range of cases where unsteady waves and steady uniform flow interaction are important, while also maintaining its advantages as mentioned in the earlier paragraphs.

2.2. Methodology

2.2.1. The First Order Boundary Value Problem

By considering eq.(1.3) – (1.10), and considering the Taylor expansion in eq.(1.19) – eq.(1.21), the 0th and 1st order variables can be found in Table 2.1 below.

Table 2.1. The 0th and 1st order variables

Var.	$O(\epsilon^0)$	$O(\epsilon^1)$
\bar{n}	$\bar{n}^{(0)} = \mathbf{n} = (n_x, n_y, n_z)$	$\bar{n}^{(1)} = \boldsymbol{\alpha}^{(1)} \times \mathbf{n}$
\bar{x}	$\bar{x}^{(0)} = \mathbf{x} = (x, y, z)$	$\bar{x}^{(1)} = \boldsymbol{\xi}^{(1)} + \boldsymbol{\alpha}^{(1)} \times \mathbf{x}$
$\bar{x} \times \bar{n}$	$(\bar{x} \times \bar{n})^{(0)} = (\mathbf{x} \times \mathbf{n})$	$(\bar{x} \times \bar{n})^{(1)} = \boldsymbol{\xi}^{(1)} \times \mathbf{n} + \boldsymbol{\alpha}^{(1)} \times (\mathbf{x} \times \mathbf{n})$
$P(\bar{x})_{SB}$	$P(\bar{x})_{SB}^{(0)} = -\rho \left(\frac{U^2}{2} + g\{z + Z_o\} \right)_{SB_0}$	$P(\bar{x})_{SB}^{(1)} = -\rho \left(\frac{\partial \phi_w^{(1)}}{\partial t} - U \frac{\partial \phi_w^{(1)}}{\partial x} + g \bar{x}^{(1)} \cdot \hat{\mathbf{k}} \right)_{SB_0}$
$\zeta(\bar{x}, \bar{y})$	$\zeta(\bar{x}, \bar{y})^{(0)} = 0$	$\zeta(\bar{x}, \bar{y})^{(1)} = -\frac{1}{g} \left(\frac{\partial \phi_w^{(1)}}{\partial t} - U \frac{\partial \phi_w^{(1)}}{\partial x} \right)_{z=0}$

By substituting the variables from eq.(1.6)- eq.(1.9), and Table 2.1 into the boundary conditions in eq.(1.15)-eq.(1.18), the 1st-order boundary conditions can be obtained by keeping all the $O(\epsilon^1)$ terms and neglecting the ϕ_{SB} terms as follows:

- Free surface boundary condition:

$$\left[g \frac{\partial}{\partial z} + \left(\frac{\partial}{\partial t} - U \frac{\partial}{\partial x} \right)^2 \right] \phi_w^{(1)} = LF = 0 \quad \text{on } S_F (z = 0) \quad (2.1)$$

- Bottom boundary condition:

$$\frac{\partial \phi_w^{(1)}}{\partial z} = 0 \quad \text{on } S_h (z = -h) \quad (2.2)$$

- Body boundary condition of the scattering potential:

$$\frac{\partial \phi_S^{(1)}}{\partial \mathbf{n}} = - \frac{\partial \phi_I^{(1)}}{\partial \mathbf{n}} \quad \text{on } S_B = S_{B0} \quad (2.3)$$

- Body boundary condition of the radiation potential:

$$\eta_k^{(1)} \frac{\partial \phi_{\tau k}^{(1)}}{\partial \mathbf{n}} = \frac{\partial \eta_k^{(1)}}{\partial t} \eta'_k + U \eta_k^{(1)} \mathbf{m}_k \quad , k=1,2,\dots,6 \quad \text{on } S_B = S_{B0} \quad (2.4)$$

where the \mathbf{m} terms come from the interaction between the zeroth-order potential with the 1st order normal direction (see Table 2.1 for definitions and [16] or [17] for details), and is defined as:

$$(\mathbf{m}_1, \mathbf{m}_2, \mathbf{m}_3) = (\mathbf{n} \cdot \nabla) \nabla \phi_{st} \quad (2.5)$$

$$(\mathbf{m}_4, \mathbf{m}_5, \mathbf{m}_6) = (\mathbf{n} \cdot \nabla) \times (\mathbf{x} \times \nabla \phi_{st}) \quad (2.6)$$

As shown by Salvesen et. al., [19], for the UF interaction model, the \mathbf{m} terms are reduced to:

$$m_j = (0, 0, 0, 0, n_3, -n_2) \quad (2.7)$$

For the case without uniform flow, the body boundary condition of the radiation potential is reduced to:

$$\eta_k^{(1)} \frac{\partial \phi_{rk}^{0(1)}}{\partial \mathbf{n}} = \frac{\partial \eta_k^{(1)}}{\partial t} \mathbf{n}'_k, \quad k=1,2,\dots,6 \text{ on } S_B = S_{B0} \quad (2.8)$$

- Far-field boundary condition:

$$\lim_{|\mathbf{x}| \rightarrow \infty} \sqrt{|\mathbf{x}|} \left(\frac{\partial}{\partial t} - ik_e \right) \left(\phi_R^{(1)} + \phi_S^{(1)} \right) \quad \text{on } S_{|\mathbf{x}| \rightarrow \infty} \quad (2.9)$$

By using eq.(2.8) (definition of $\phi_{rk}^{0(1)}$) and by substituting the \mathbf{m} terms definition in eq.(2.7) to the radiation body boundary conditions in eq.(2.4), the relation between the radiation potential with uniform flow $\phi_{rk}^{(1)}$ and the radiation potential with zero forward speed $\phi_{rk}^{0(1)}$ can be written as follows:

$$\phi_{rk}^{(1)} = \begin{cases} \phi_{rk}^{0(1)} & \text{for } k < 5 \\ \phi_{rk}^{0(1)} + U\phi_{rk}^{0(1)} & \text{for } k = 5 \\ \phi_{rk}^{0(1)} - U\phi_{rk}^{0(1)} & \text{for } k = 6 \end{cases} \quad (2.10)$$

The linear free surface boundary condition can be reduced back to the same form as the case without uniform flow, if $\omega_e \gg U(\partial/\partial x)$:

$$\left[g \frac{\partial}{\partial z} + \left(\frac{\partial}{\partial t} - U \frac{\partial}{\partial x} \right)^2 \right] \phi_w^{(1)} \cong \left[g \frac{\partial}{\partial z} + \frac{\partial^2}{\partial t^2} \right] \phi_w^{(1)} = LF^0 = 0 \quad (2.11)$$

The $\omega_e \gg U(\partial/\partial x)$ condition above can be fulfilled if one or the combination of the following conditions is fulfilled: (1) high encounter frequency ω_e , (2) low uniform flow magnitude U , (3)

slender body. In other words the longitudinal derivatives ($\partial/\partial x$) have to be small compared to the transversal derivatives ($\partial/\partial y$ & $\partial/\partial z$). Furthermore, even though the far-field boundary condition is written as eq.(2.9), it is not exact in the presence of forward speed. For the results presented in this study, a pragmatic approach was taken in that both eq.(2.9) and the 0-speed free-surface condition are assumed to be satisfied to develop the numerically simpler approach. The same approach was also applied in [20, 21, 23, 25]. Several important implications due to these assumptions and approximations are:

1. Zero-speed free surface green function can be used.
2. Only body boundary conditions need to be fulfilled by the radiation and scattering potentials; therefore, no free surface discretization is needed.
3. No additional steps compared to the zero-speed case are needed to solve the steady wave potentials.
4. The change in wave's diffraction forces, added mass, and hydrodynamic damping due to the wave-current interactions can be treated as correction terms to the 0-speed values.

Therefore, $\phi_{S_i}^{(1)}$ and $\phi_{rk_i}^{(1)}$ can be obtained by solving the same body boundary condition as the one for the zero-speed case but evaluated at ω_{e_i} . From eq.(2.11), the first order incident wave at a given frequency ω_0 follows the Airy's linear wave theory as follow:

$$\phi_{I_i} = \frac{igA_i \cosh(k_i(z+h))}{\omega_{0_i} \cosh(k_i h)} e^{-ik_i \cdot x} \quad (2.12)$$

where A denotes the incident wave's amplitude, h denotes the water depth, $\mathbf{k}_i = k_i(\cos \beta_i \hat{\mathbf{i}} + \sin \beta_i \hat{\mathbf{j}})$ denotes the wave number where $\omega_{0_i}^2 = gk_i \tanh(k_i h)$, and β_i denotes the wave heading angle of incidence to the positive x-axis.

2.2.2. 1st Order Hydrodynamic Loading and Equation of Motion

After solving the first order potentials ϕ_{I_i} , ϕ_{S_i} , and $\phi_{rk_i}^0$, the 1st order forces and moments are obtained by collecting the $O(\epsilon^1)$ terms in eq.(1. 22)- eq.(1. 23):

$$\mathbf{F}^{(1)} = \mathbf{F}'_{1-3} = \iint_{S_{B0}} P^{(1)} \bar{\mathbf{n}}^{(0)} dS + \iint_{S_{B0}} P^{(0)} \bar{\mathbf{n}}^{(1)} dS \quad (2.13)$$

$$\begin{aligned} &= -\rho \iint_{S_{B0}} \left(\frac{\partial \phi_w^{(1)}}{\partial t} - U \frac{\partial \phi_w^{(1)}}{\partial x} \right) \mathbf{n} dS \\ &\quad - \rho g \iint_{S_{B0}} (\boldsymbol{\xi}^{(1)} + \boldsymbol{\alpha}^{(1)} \times \mathbf{x}) \cdot \hat{\mathbf{k}} \mathbf{n} dS \\ &\quad - \rho g \iint_{S_{B0}} (z + Z_o) (\boldsymbol{\alpha}^{(1)} \times \mathbf{n}) dS \\ &\quad + \rho \iint_{S_{B0}} \frac{U^2}{2} (\boldsymbol{\alpha}^{(1)} \times \mathbf{n}) dS \end{aligned}$$

$$\mathbf{M}^{(1)} = \mathbf{F}'_{4-6} = \iint_{S_{B0}} (\bar{\mathbf{x}} \times \bar{\mathbf{n}})^{(0)} P^{(1)} dS + \iint_{S_{B0}} (\bar{\mathbf{x}} \times \bar{\mathbf{n}})^{(1)} P^{(0)} dS \quad (2.14)$$

$$\begin{aligned} &= -\rho \iint_{S_{B0}} (\mathbf{x} \times \mathbf{n}) \left(\frac{\partial \phi_w^{(1)}}{\partial t} - U \frac{\partial \phi_w^{(1)}}{\partial x} \right) dS \\ &\quad - \rho g \iint_{S_{B0}} (\mathbf{x} \times \mathbf{n}) (\boldsymbol{\xi}^{(1)} + \boldsymbol{\alpha}^{(1)} \times \mathbf{x}) \cdot \hat{\mathbf{k}} dS \\ &\quad - \rho g \iint_{S_{B0}} (\boldsymbol{\xi}^{(1)} \times \mathbf{n}) (z + Z_o) dS - \rho g \iint_{S_{B0}} [\boldsymbol{\alpha}^{(1)} \times (\mathbf{x} \times \mathbf{n})] (z + Z_o) dS \\ &\quad + \rho \iint_{S_{B0}} (\boldsymbol{\xi}^{(1)} \times \mathbf{n}) \frac{U^2}{2} dS + \rho \iint_{S_{B0}} [\boldsymbol{\alpha}^{(1)} \times (\mathbf{x} \times \mathbf{n})] \frac{U^2}{2} (\boldsymbol{\alpha}^{(1)} \times \mathbf{n}) dS \end{aligned}$$

where $\mathbf{F}' = (F'_1, F'_2, \dots, F'_6)$ is the generalized force vector, as defined in eq.(24). Similar to the eq.(12), the total time-varying forces and moments are defined as $\mathbf{F}'_T{}^{(1)}(t) = \text{Re} \sum_{i=1}^N \mathbf{F}'_i e^{i\omega_{e_i} t}$.

The first term in both 1st order force and moment formula is the 1st order hydrodynamic forces. The hydrodynamic forces can be further decomposed into the Froude-Krylov wave exciting force $\mathbf{F}'_I^{(1)}$ consisting of $\phi_I^{(1)}$, the scattered wave exciting force $\mathbf{F}'_S^{(1)}$ consisting of $\phi_S^{(1)}$, and the added mass $[\mathbf{A}]$ and hydrodynamic damping $[\mathbf{B}]$ consisting of $\phi_{r_k}^{(1)}$. Meanwhile, the rest of the terms are the hydrostatic terms that contribute to the 1st order hydrostatic stiffness $[\mathbf{K}_h]$. Considering eq.(2.5)-(2.10), the 1st order hydrodynamic load components can be simplified into (see [19] for detailed derivations):

- Incident wave exciting force:

$$\begin{aligned} F'_{I_k}{}^{(1)} &= \rho \iint_{S_{B0}} \left(\frac{\partial \phi_I^{(1)}}{\partial t} - U \frac{\partial \phi_I^{(1)}}{\partial x} \right) n'_k dS & (2.15) \\ &= \rho i \iint_{S_{B0}} (\omega_e - Uk \cos \beta_{w_o}) \phi_I^{(1)} n'_k dS \\ &= i \omega_0 \rho \iint_{S_{B0}} \phi_I^{(1)} n'_k dS \end{aligned}$$

- Scattered wave exciting force, with uniform flow correction:

$$F'_{S_k}{}^{(1)} = \rho \iint_{S_{B0}} \left(\frac{\partial \phi_S^{(1)}}{\partial t} - U \frac{\partial \phi_S^{(1)}}{\partial x} \right) n'_k dS \quad (2.16)$$

The spatial derivative in the convective term in the scattered wave's loading can be avoided by utilizing Stoke's theorem, as shown in ref.[17, 19]:

$$F'_{S_k}{}^{(1)} = i \omega_e \rho \iint_{S_{B0}} \phi_S^{(1)} n'_k dS - \rho \iint_{S_{B0}} U m_k \phi_S^{(1)} dS \quad (2.17)$$

Or, by using the Haskind's relation, it can also be written as:

$$\begin{aligned}
F_{S_j}^{(k)} &= -\rho \iint_{S_{B0}} \frac{\partial \phi_I^{(1)}}{\partial n} \phi_{r_k}^{0(1)} dS && \text{for } k = 1, 2, 3, 4 && (2.18) \\
&= -\rho \left\{ \iint_{S_{B0}} \frac{\partial \phi_I^{(1)}}{\partial n} \phi_{r_k}^{0(1)} dS + \frac{\rho U}{i\omega_e} \iint_{S_{B0}} \frac{\partial \phi_I^{(1)}}{\partial n} \phi_{r_3}^{0(1)} dS \right\} && \text{for } k = 5 \\
&= -\rho \left\{ \iint_{S_{B0}} \frac{\partial \phi_I^{(1)}}{\partial n} \phi_{r_k}^{0(1)} dS - \frac{\rho U}{i\omega_e} \iint_{S_{B0}} \frac{\partial \phi_I^{(1)}}{\partial n} \phi_{r_2}^{0(1)} dS \right\} && \text{for } k = 6
\end{aligned}$$

- Hydrodynamic damping and added mass, with uniform flow correction:

$$F_{r_k}^{\prime(1)} = \sum_{m=1}^6 \left(A_{km} - \frac{i}{\omega_e} B_{km} \right) \eta_m^{(1)} \quad (2.19)$$

where,

$$\left(A_{km} - \frac{i}{\omega_e} B_{km} \right) = i\omega_e \rho \iint_{S_{B0}} \phi_{r_m}^{(1)} n'_k dS - \rho \iint_{S_{B0}} U m_k \phi_{r_m}^{(1)} dS \quad (2.20)$$

where the 6×6 added mass matrix $[\mathbf{A}] = A_{km}$ and hydrodynamic damping $[\mathbf{B}] = B_{km}$ can be rewritten in terms of its relationship with the added mass and hydrodynamic damping without the uniform flow as follow:

$$\left(A_{km}^0 - \frac{i}{\omega_e} B_{km}^0 \right) = i\omega_e \rho \iint_{S_{B0}} \phi_{r_m}^{0(1)} n'_k dS \quad (2.21)$$

$$A_{15} = A_{15}^0 - \frac{U}{\omega_e^2} B_{13}^0 \quad A_{26} = A_{26}^0 + \frac{U}{\omega_e^2} B_{22}^0 \quad B_{15} = B_{15}^0 + U A_{13}^0 \quad B_{26} = B_{26}^0 - U A_{22}^0$$

$$A_{51} = A_{51}^0 + \frac{U}{\omega_e^2} B_{31}^0 \quad A_{62} = A_{62}^0 - \frac{U}{\omega_e^2} B_{22}^0 \quad B_{51} = B_{51}^0 - U A_{31}^0 \quad B_{62} = B_{62}^0 + U A_{22}^0$$

$$A_{35} = A_{35}^0 - \frac{U}{\omega_e^2} B_{33}^0 \quad A_{46} = A_{46}^0 + \frac{U}{\omega_e^2} B_{24}^0 \quad B_{35} = B_{35}^0 + U A_{33}^0 \quad B_{46} = B_{46}^0 - U A_{24}^0$$

$$\begin{aligned}
A_{53} &= A_{53}^0 + \frac{U^2}{\omega_e^2} B_{33}^0 & A_{64} &= A_{64}^0 - \frac{U}{\omega_e^2} B_{42}^0 & B_{53} &= B_{53}^0 - UA_{33}^0 & B_{64} &= B_{64}^0 + UA_{42}^0 \\
A_{55} &= A_{55}^0 + \frac{U^2}{\omega_e^2} A_{33}^0 & A_{66} &= A_{66}^0 + \frac{U^2}{\omega_e^2} A_{22}^0 & B_{55} &= B_{55}^0 + \frac{U^2}{\omega_e^2} B_{33}^0 & B_{66} &= B_{66}^0 + \frac{U^2}{\omega_e^2} B_{22}^0
\end{aligned} \quad (2.22)$$

The 1st order motions are needed to calculate the 2nd order force and moment. The 1st order motion can be obtained by solving the following equation of motion:

$$[\mathbf{M} + \mathbf{A}(\omega_e)]\ddot{\boldsymbol{\eta}}^{(1)} + [\mathbf{B}(\omega_e)]\dot{\boldsymbol{\eta}}^{(1)} + [\mathbf{K}_h]\boldsymbol{\eta}^{(1)} = \mathbf{F}'_I^{(1)} + \mathbf{F}'_S^{(1)} \quad (2.23)$$

where $[\mathbf{M}]$ and $[\mathbf{K}_h]$ are the 6×6 mass and hydrostatic stiffness matrix, respectively. The equation solves for 6×1 motion vector $\boldsymbol{\eta}^{(1)}$ at each frequency component ω_{e_i} , where the total motion is defined as $\boldsymbol{\eta}_T^{(1)}(t) = \text{Re} \sum_{i=1}^N \boldsymbol{\eta}^{(1)} e^{i\omega_{e_i} t}$. We can see that the hydrodynamic forces due to radiation potential and the hydrostatic forces can be moved to the left-hand side due to its dependency on the body's motion.

2.2.3. Numerical Implementation

To solve the first order disturbance potentials ϕ_{S_i} and $\phi_{rk_i}^0$, the boundary element method is used. Boundary Element Method can be derived using two different ways, by the velocity potential or Green's formulation and the source distribution formulation. An in-house program that was originally developed for linear zero speed wave diffraction-radiation problem was used as a base code. In the linear wave diffraction-radiation problems without uniform flow, the Green's formulation BEM is used. For the problems involving uniform flow interaction and second order wave's problem, however, the source distribution method is more proper to be used due to reasons explained in this sub-section.

The Green's formulation can be derived by applying the Divergence theorem to Ψ , where Ψ is a continuously differentiable vector field, as follow:

$$\iiint_{V_V} (\nabla \cdot \Psi) dV = \iint_{S_V} (\mathbf{F} \cdot \mathbf{n}) dA \quad (2.24)$$

where the left hand side is a volume integral over the enclosed volume V_V , the right hand side is the surface integral over the boundary of the volume V_V , and \mathbf{n} is a normal directional vector of the boundary of the volume V_V with (+) value pointing outward. In our problem, V_V encompasses all the fluid domain, while S_V consist of far field, sea bottom, free surface, and body surface boundaries.

Letting $\Psi = \phi \nabla G - G \nabla \phi$ where both ϕ and G are both a scalar function which derivative denotes the flow's velocity field, and with both satisfies Laplace equation, we obtain,

$$\iiint_{V_V} \nabla \cdot (\phi \nabla G - G \nabla \phi) dV = \iint_{S_V} (\phi \nabla G - G \nabla \phi) \cdot \mathbf{n} dA \quad (2.25)$$

$$\iiint_{V_V} (\phi \nabla^2 G - G \nabla^2 \phi + \nabla \phi \nabla G - \nabla \phi \nabla G) dV = \iint_{S_V} (\phi \nabla G - G \nabla \phi) \cdot \mathbf{n} dA$$

$\nabla^2 \phi = \nabla^2 G = 0$ from Laplace equation and $\nabla G \cdot \mathbf{n} = \frac{\partial G}{\partial n}$ = velocity projected into the normal direction of the body. $\frac{\partial G}{\partial n}$ contains singularity terms that need to be excluded from the integral solution and solved by using residual analysis. $\frac{\partial \phi}{\partial n}$ can be obtained from the normal velocity of the fluid on the body's surface V_n . the above equation can be rewritten into:

$$2\pi\phi + \iint_{S_V} \phi \frac{\partial G}{\partial n} dA = \iint_{S_V} G V_n dA \quad (2.26)$$

In panel method, the continuous surface of a body is represented as the summation of quadrilateral or triangular panels. Further assumption is made by considering that the magnitude

of the velocity potential ϕ is constant on each panel. With these considerations, the discretization of the integral equation can be written as:

$$2\pi\phi(\mathbf{x}_i) + \sum_{j=1}^{N_p} \phi(\mathbf{x}_j) \frac{\partial G(\mathbf{x}_j, \mathbf{x}_i)}{\partial n_j} A_j = \sum_{j=1}^{N_p} G(\mathbf{x}_j, \mathbf{x}_i) V_{nj} A_j \quad (2.27)$$

where N_p, j, i, A, n are the total number of the boundary panel, index of the position vector of the source panel, index of the position vector of the calculated panel / field points, area of the panel, and normal direction of the panel with positive pointing into the fluid domain respectively. $G(\mathbf{x}_j, \mathbf{x}_i)$ is a function that can be obtained by solving the partial differential equation in the Boundary Value Problem in the previous section while also fulfilling the Laplace condition.

Considering the linearity of the potential velocity formulation of the flow field, the total potential velocity at a field point can be defined as a summation of the potential velocity imposed by the source points originated from the boundaries. This methodology in formulating the boundary element method also called the source distribution method. This formulation is written as:

$$\phi(\mathbf{x}_i) = \iint_{A_B} \sigma(\mathbf{x}_j) G(\mathbf{x}_i, \mathbf{x}_j) dA \quad (2.28)$$

where $\sigma(\mathbf{x}_j)$ is the source strength of the potential velocity. By taking the normal derivative with respect to the collocation point i , we have,

$$V_{ni} = \frac{\partial \phi(\mathbf{x}_i)}{\partial n_i} = \iint_{A_B} \frac{\partial (\sigma(\mathbf{x}_j) G(\mathbf{x}_i, \mathbf{x}_j))}{\partial n_i} dA \quad (2.29)$$

Using the same discretization method as the Green's method and assuming that the magnitude of the source strength σ is constant on each panel, the discretization of the integral equation of the eq.(2.29) above can be written as:

$$2\pi\sigma(\mathbf{x}_i) + \sum_{j=1}^{Np} \sigma(\mathbf{x}_j) \frac{\partial G(\mathbf{x}_i, \mathbf{x}_j)}{\partial n_i} A_j = V_{ni} \quad (2.30)$$

The equation above will solve for $\sigma(\mathbf{x}_i)$. One can then obtain the potential velocity from the source strength by using the definition of the potential velocity of:

$$\phi(\mathbf{x}_i) = \sum_{j=1}^{Np} \sigma(\mathbf{x}_j) G(\mathbf{x}_i, \mathbf{x}_j) A_j \quad (2.31)$$

The differences between the Green's and source distribution formulation can be summarized into Table 2.2 below:

Table 2.2. Differences between potential formulations Vs. source distribution formulation

Difference	Green's/potential formulation	Source Distribution formulation
What the matrix solve	Velocity potential ϕ_i	Source strength σ_i
Right hand side	$\sum_{i=1}^{NPAN} \frac{\partial \phi_j}{\partial n_j} \iint_{A_j} G(\vec{x}_j, \vec{x}_i) dA_j$	$\frac{\partial \phi_i}{\partial n_i}$
Left hand side coefficient matrix	$\iint_{A_j} \frac{G(\vec{x}_j, \vec{x}_i)}{\partial n_j} dA_j$	$\iint_{A_j} \frac{G(\vec{x}_i, \vec{x}_j)}{\partial n_i} dA_j$
Velocity potential calculation	Directly from the matrix	$\phi_i = \sum_{j=1}^{NPAN} \sigma_j \iint_{A_j} G(\vec{x}_i, \vec{x}_j) dA_j$
Highest order derivative on the equation for velocity calculation	$\iint_{A_j} \frac{G(\vec{x}_j, \vec{x}_i)}{\partial n_j \partial x_j} dA_j$	$\iint_{A_j} \frac{G(\vec{x}_j, \vec{x}_i)}{\partial x_j} dA_j$

Note that the source distribution formulation require additional step to solve for the velocity potential. However, since the flow's velocity calculated from the Green's method require a second order derivative of the Green's function, it will be more prone to discontinuity. For these reasons, in this study, all 1st order wave's potentials will be calculated using the Green's formulation, while the 1st order wave's potential spatial derivatives will be calculated using the source distribution formulation. For both boundary element's formulation, the green function $G(\mathbf{x}_i, \mathbf{x}_j)$ remain the same, which are:

$$G(\mathbf{x}_i, \mathbf{x}_j) = G_{so}(\mathbf{x}_i, \mathbf{x}_j) + G_{so2}(\mathbf{x}_i, \mathbf{x}_j) + G_{fs}(\mathbf{x}_i, \mathbf{x}_j) \quad (2.32)$$

$$G_{so}(\mathbf{x}_i, \mathbf{x}_j) = \frac{1}{\sqrt{(x_i-x_j)^2+(y_i-y_j)^2+(z_i-z_j)^2}} \quad (2.33)$$

$$G_{so2}(\mathbf{x}_i, \mathbf{x}_j) = \frac{1}{\sqrt{(x_i-x_j)^2+(y_i-y_j)^2+(z_i+z_j)^2}} \quad (2.34)$$

$$G_{fs}(\mathbf{x}_i, \mathbf{x}_j) = \frac{2\nu}{\pi} \int_0^\infty \frac{e^{k(z_i+z_j)}}{k-\nu} J_0(kR) dk + i2\pi\nu J_0(\nu R) \quad (2.35)$$

G_{so} is the rankine / source Green's function that satisfies the Laplace equation. G_{so2} is the image rankine green function with respect with the x-y plane so that the fluid particle that's on the free surface $z = \zeta$ will stay on the free surface. G_{fs} is the free surface Green function that satisfy all the previous conditions mentioned before, along with the free surface boundary condition and the far field radiation condition. Among many others, the derivation of the green function can be found in [29, 30].

By only using the G_{so} and G_{so2} alone, we can solve the boundary value problem by utilizing eq.(2.29)-(2.31) and apply it to all boundary surfaces, which include the free surface and the body

surface. This approach is called the rankine panel BEM. Since the change in the boundary condition does not change the green function's formulation, this approach can handle different boundary condition with relative ease if done properly. However, this method also have disadvantages when it comes to computation time, number of computation points, and also required additional treatments to fulfill the bottom boundary and far field radiation condition.

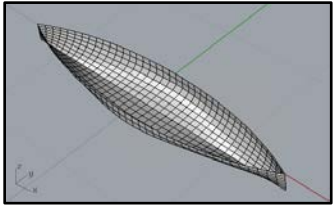
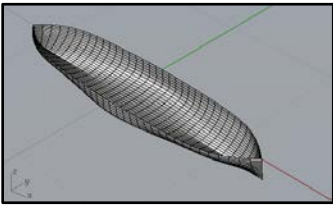
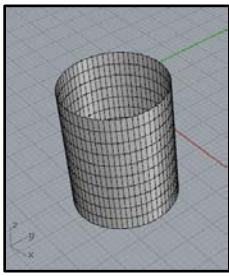
The approach that is used in the present study is called the Free Surface Green's function panel BEM, or Green's panel BEM for short. This approach take into account G_{fs} so that all boundary conditions except the body boundary condition are satisfied. Note that the G_{fs} in the eq.(2.35) was derived by only considering the FSBC without any uniform flow effect (see eq.(2.11)).

2.3. Case Study

2.3.1. Case Definition

Case study was done to see how the Uniform flow approximation performed against other method and against experimental results. These test studies can be summarized in Table 2.3 above. CASE 1 and CASE 2 is compared against the same Uniform flow approximation numerical simulation that was done by another independent study on ref. [23, 25], and experimental results for both the exciting force and the motion [31]. For force calculation, additional CASE 3 are used to inspect the robustness of the Uniform flow approximation against higher order methods. CASE 3 is compared against a UF approximation in time domain quadratic boundary element method (ref. [14]).

Table 2.3. Validation and preliminary result cases

NAME	HULL TYPE	BEM PANEL	CASE DETAIL
CASE 1	Slender Wigley		<ul style="list-style-type: none"> • $L = 2 \text{ m}$ • $B = 0.3 \text{ m}$ • $D = 0.125 \text{ m}$ • $F_n = 0.2$ • $\beta_{w0} = 0^\circ$ • $\beta_{wc} = 180^\circ$
CASE 2	Blunt Wigley		<ul style="list-style-type: none"> • $L = 2.5 \text{ m}$ • $B = 0.5 \text{ m}$ • $D = 0.175 \text{ m}$ • $F_n = 0.2$ • $\beta_{w0} = 0^\circ$ • $\beta_{wc} = 180^\circ$
CASE 3	Cylinder		<ul style="list-style-type: none"> • $D = 27.4 \text{ m}$ • $R = 10.8 \text{ m}$ • $F_n = 0.137$ • $\beta_{w0} = 0^\circ$ • $\beta_{wc} = 180^\circ$

2.3.2. Results and Discussions

2.3.2.1. CASE 1 Results and Discussion

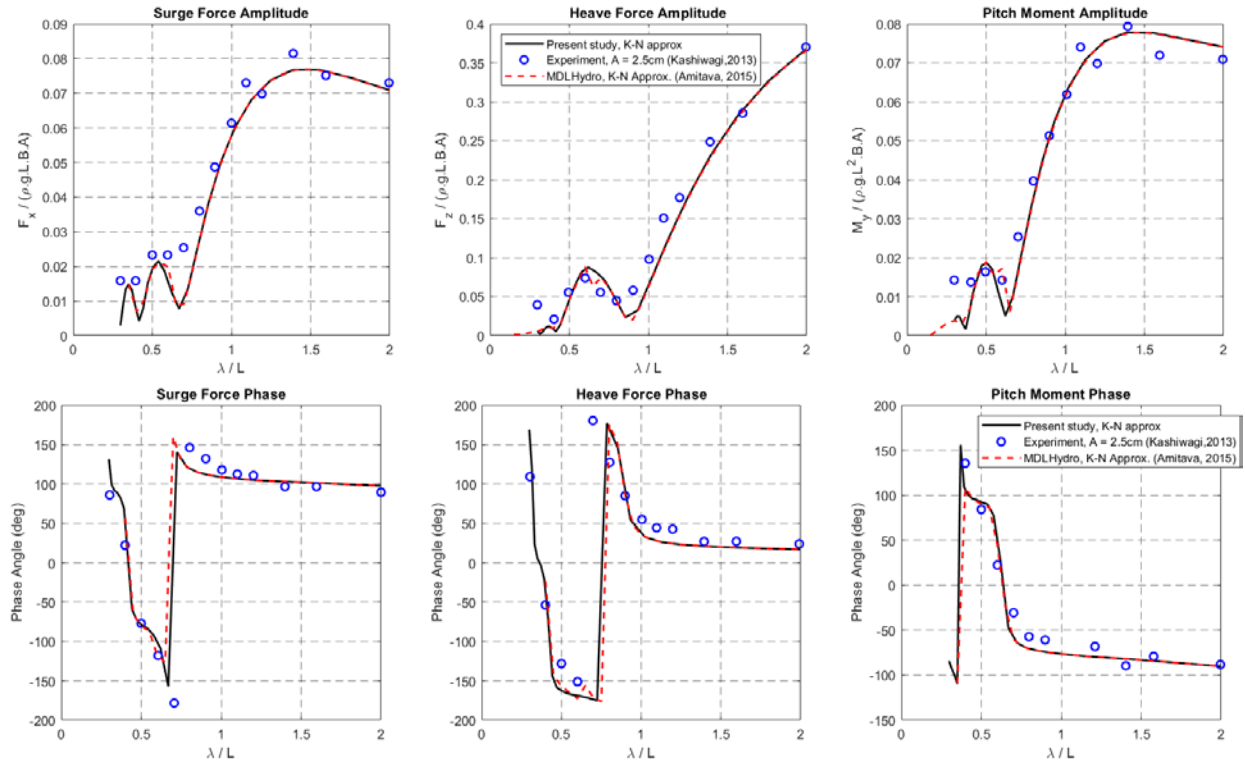


Fig. 2.1. Force amplitude (top) and phase (bottom) validation of the present study against similar approach from ref.[23,25] and experiment data from ref.[31] for slender Wigley hull with $F_n = 0.2$

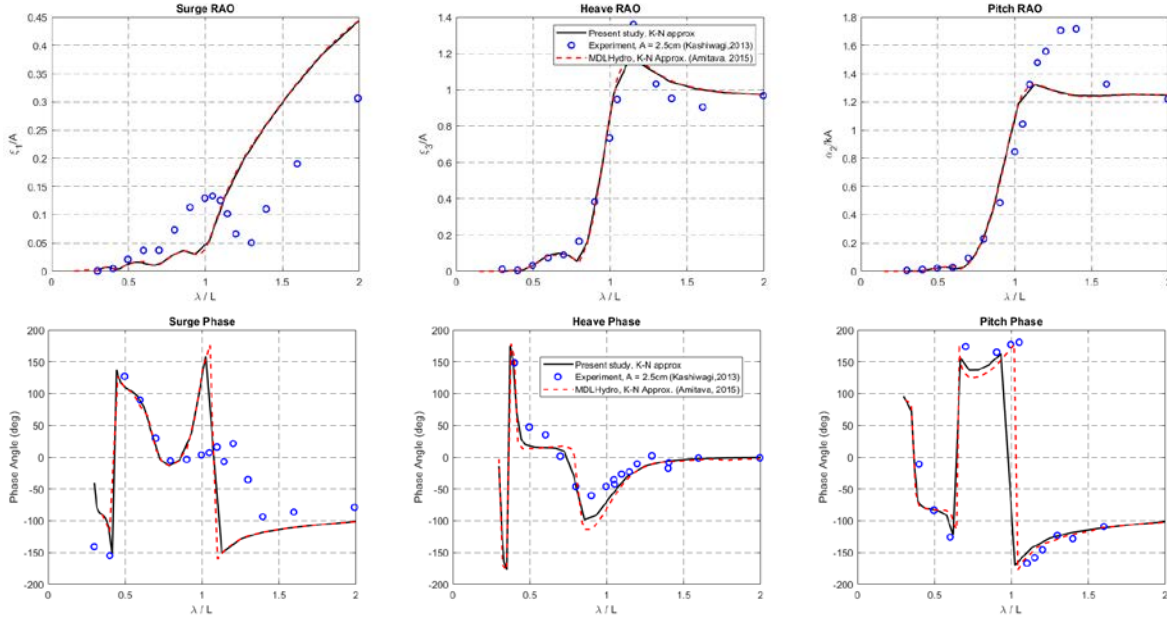


Fig. 2.2. RAO amplitude (top) and phase (bottom) validation of the present study against similar approach from ref.[23,25] and experiment data from ref.[31] for slender Wigley hull with $F_n = 0.2$

For the slender Wigley Hull with $F_n = 0.2$ case(Fig. 2.1-Fig. 2.2), good agreements for both forces and RAOs with another UF approximation study (ref. [23, 25]) were achieved. The UF approximation method also agrees well with the experiment results, especially the exciting forces, and heave RAO. Exception can be found on the heave and pitch resonance RAO and the overall surge RAO. It is well known that for slender body, the linear potential theory typically under predict the surge damping. Furthermore, as mentioned in [31], the motion is highly non-linear and that the viscous effect is more pronounce at the heave and pitch resonance frequency.

2.3.2.2. CASE 2 Results and Discussion

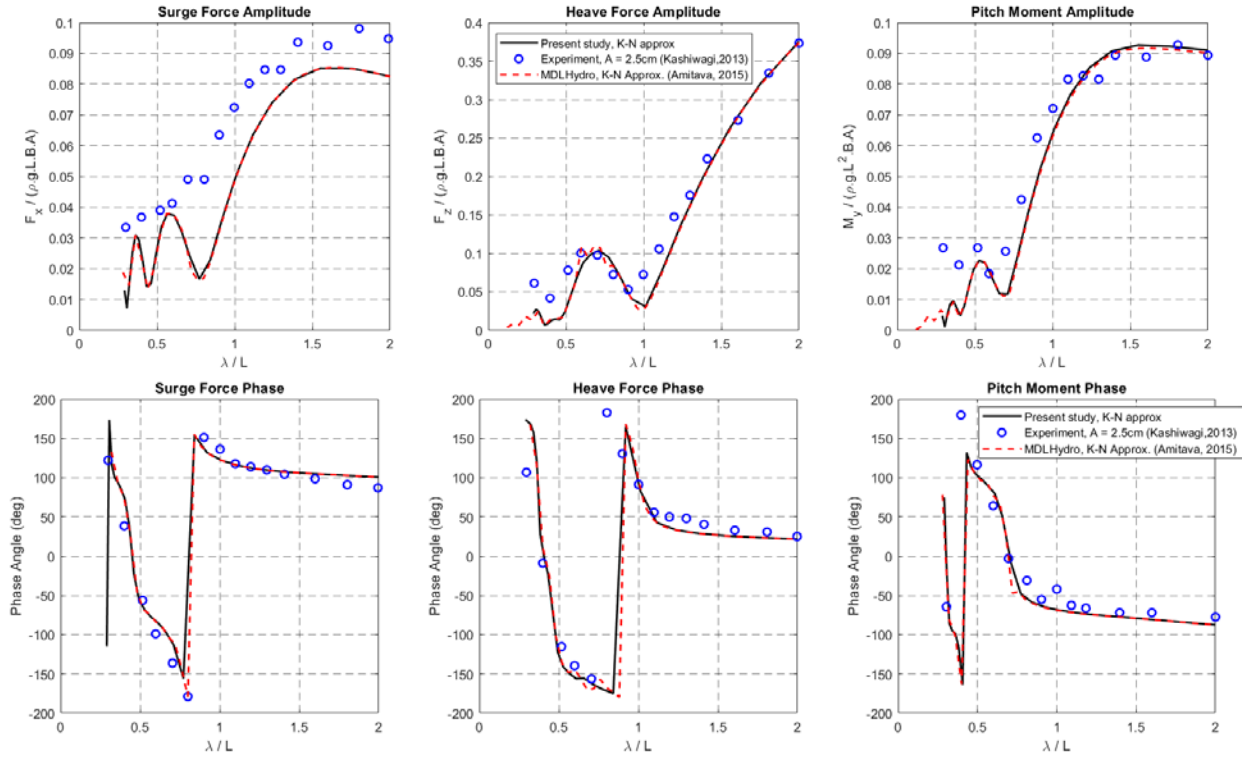


Fig. 2.3. Force amplitude (top) and phase (bottom) validation of the present study against similar approach from ref.[23,25] and experiment data from ref.[31] for blunt Wigley hull with $F_n =$

0.2

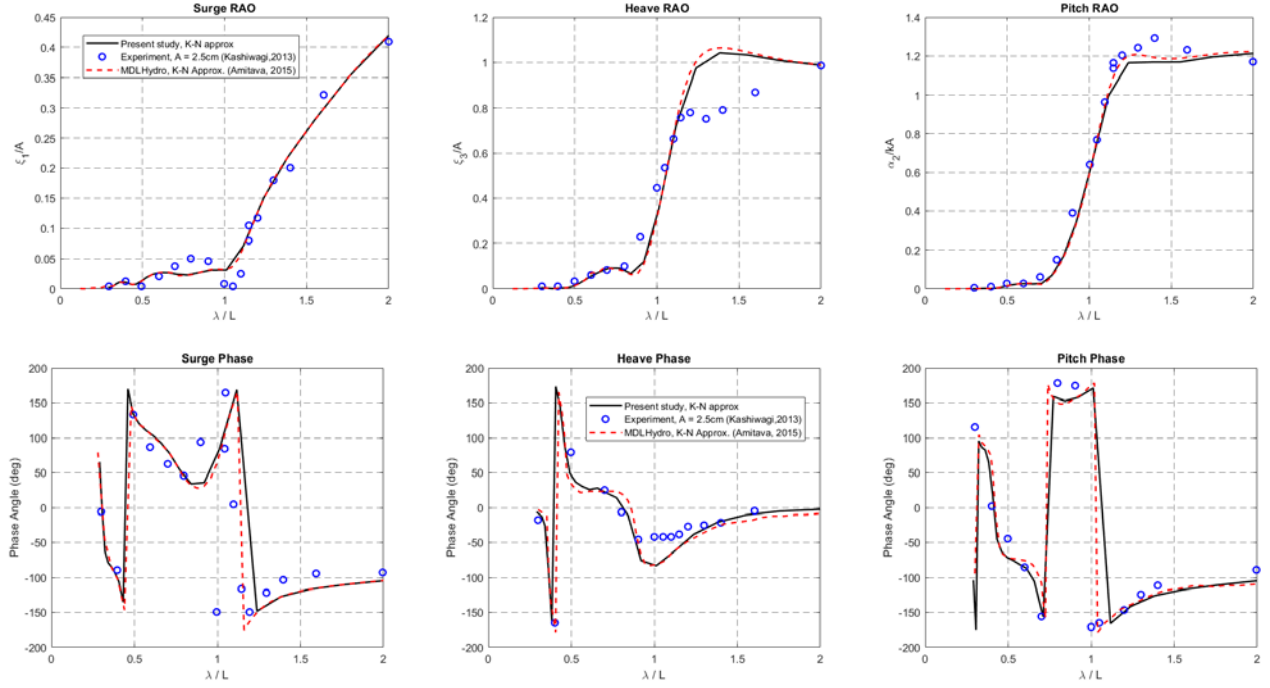


Fig. 2.4. RAO amplitude (top) and phase (bottom) validation of the present study against similar approach from ref.[23,25] and experiment data from ref.[31] for slender Wigley hull with $F_n = 0.2$

For the blunt wigley Hull with $F_n = 0.2$ (Fig. 2.3-Fig. 2.4), we also obtained a good agreement with another UF approximation study (ref. [23, 25]), for both forces and RAOs. The UF approximation method also agrees well with the experiment results for both exciting forces and RAOs. Exception can be found on the heave motion which are overpredicted, which might caused by viscous or non linear effect that are present on the experiment.

2.3.2.3. CASE 3 Results and Discussion

From Fig. 2.5, we can see that the UF approximation agrees well with body nonlinear – free surface nonlinear time domain rankine panel BEM on ref. [14] for the cylinder case. The same reversal for surge and pitch where on lower period the forces becomes larger than the $U = 0$ in contrast with the peak amplitude are observed on both method.

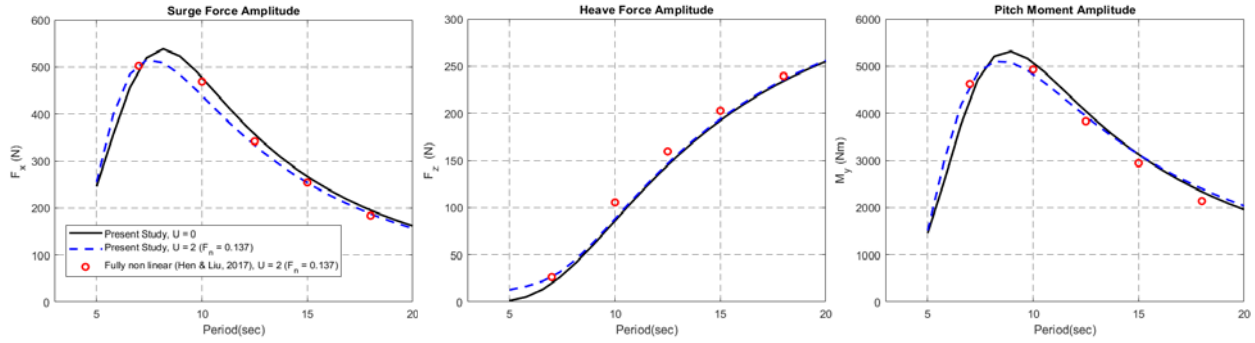


Fig. 2.5. Comparison between the UF approximations with weakly nonlinear time domain rankine panel UF BEM from ref.[14]

2.4. Summary

An in-house linear wave-current interaction simulation tool is developed by considering UF approximation in the frequency domain - 3D BEM framework. An in-house program that was originally developed for linear zero speed wave diffraction-radiation problem was used as a base. The program is then extended to include the source formulation to calculate velocity more accurately and also extended to include the linear wave-current interaction effect.

In overall, the UF wave-uniform flow interaction model are proven to be robust enough to solve typical fluid structure interaction problem, especially when the structure is considered to be slender. More comparative studies and validations can be found in ref. [9, 20, 22, 23, 25]. The UF approximation also proven to be straightly applicable to any BEM simulation tools, since all interaction terms reduced to correction terms that can be obtained from zero uniform speed simulation. Due to the ease of implementation in the linear problem, there are still rooms for this method to be applied to other linear theory such as linear hydro elasticity problems. For non-linear problem however, the UF approximation needed additional efforts to be implemented since all the non-linear hydrodynamic coefficients will not solely comprise of the output from $U = 0$

simulation results. Due to these reasons, we aim to present the extension to the UF approximation method so that its applicability is extended to cover wider range of problems in the following sections.

2.5. References

- [1] S. E. Hirdaris *et al.*, "Loads for use in the design of ships and offshore structures," *Ocean Engineering*, vol. 78, pp. 131-174, 2014.
- [2] H. Liang, Z. Ren-chuan, M. Guo-ping, and F. Ju, "Study on Havelock form translating-pulsating source Green's function distributing on horizontal line segments and its applications," *Ocean Engineering*, vol. 124, pp. 306-323, 2016.
- [3] I. Ten, H. Liang, and X. Chen, "New formulations of the ship-motion Green function," *Journal of Engineering Mathematics*, vol. 110, no. 1, pp. 39-61, 2018.
- [4] C. Xie, X. Chen, A. H. Clément, and A. Babarit, "A new ordinary differential equation for the evaluation of the frequency-domain Green function," *Applied Ocean Research*, vol. 86, no. February, pp. 239-245, 2019.
- [5] C. Yang, F. Noblesse, and R. Löhner, "Comparison of classical and simple free-surface green functions," *Proceedings of the International Offshore and Polar Engineering Conference*, vol. 14, no. 4, pp. 439-446, 2004.
- [6] G. F. Clauss and K. Stutz, "Time-domain analysis of floating bodies with forward speed," *Journal of Offshore Mechanics and Arctic Engineering*, vol. 124, no. 2, pp. 66-73, 2002.
- [7] F. T. Korsmeyer and H. B. Bingham, "The Forward Speed Diffraction Problem," *Journal of Ship Research*, vol. 42, no. 2, pp. 99-112, 1998.
- [8] X. Chen, R. c. Zhu, J. Zhao, W. j. Zhou, and J. Fan, "Study on weakly nonlinear motions of ship advancing in waves and influences of steady ship wave," *Ocean Engineering*, vol. 150, no. February, pp. 243-257, 2018.
- [9] G. J. Grigoropoulos, C. Katsikis, and D. S. Chalkias, "Experimental verification of the linear and non-linear versions of a panel code," *International Journal of Naval Architecture and Ocean Engineering*, vol. 3, no. 1, pp. 27-36, 2011.
- [10] X. Zhang, P. Bandyk, and R. F. Beck, "Seakeeping computations using double-body basis flows," *Applied Ocean Research*, vol. 32, no. 4, pp. 471-482, 2010.
- [11] S. M. Scorpio and R. F. Beck, "A Multipole Accelerated Desingularized Method for Computing Nonlinear Wave Forces on Bodies," *Journal of Offshore Mechanics and Arctic Engineering*, vol. 120, no. 2, pp. 71-76, 1998.

- [12] A. Subramani, R. F. Beck, and S. M. Scorpio, "Fully nonlinear free-surface computations for arbitrary and complex hull forms," *Twenty-Second Symposium on Naval Hydrodynamics*, vol. 2, pp. 390-402, 1999.
- [13] Z. Ran, "Coupled Dynamic Analysis of Floating Structures in Waves and Currents," 2000.
- [14] M. Shen and Y. Liu, "Current effects on global motions of a floating platform in waves," *Ocean Systems Engineering*, vol. 7, no. 2, pp. 121-141, 2017.
- [15] R. A. Watai, F. Ruggeri, and A. N. Simos, "A new time domain Rankine panel method for simulations involving multiple bodies with large relative displacements," *Applied Ocean Research*, vol. 59, pp. 93-114, 2016.
- [16] R. Timman and J. Newman, "The Coupled Damping Coefficients of a Symmetric Ship," *Journal of Ship Research*, 1963.
- [17] T. Ogilvie and E. Tuck, "A rational strip theory of ship motions: part I," ed, 1969, pp. 107-107.
- [18] R. Brard, "Representation of a given ship form by singularity distributions when the boundary condition on the free surface is linearized," *Journal of Ship Research*, vol. 16, no. 1, pp. 79-92, 1972.
- [19] N. Salvesen, E. Tuck, and O. Faltinsen, "Ship motions and sea loads," vol. 78, ed, 1970, pp. 250-287.
- [20] A. Papanikolaou and T. Schellin, "A three-dimensional panel method for motions and loads of ships with forward speed," *Ship Technology Research (Schiffstechnik)*, vol. 39, no. 4, pp. 145-155, 1992.
- [21] R. F. Beck and A. E. Loken, "Three-dimensional effects in ship relative-motion problems," *Journal of Ship Research*, vol. 33, no. 4, pp. 261-268, 1989.
- [22] K. H. Kim and Y. Kim, "Comparative study on ship hydrodynamics based on Neumann-Kelvin and double-body linearizations in time-domain analysis," *International Journal of Offshore and Polar Engineering*, vol. 20, no. 4, pp. 265-274, 2010.
- [23] A. Guha and J. Falzarano, "Estimation of hydrodynamic forces and motion of ships with steady forward speed," *International Shipbuilding Progress*, vol. 62, no. 3-4, pp. 113-138, 2016.
- [24] M. Kashiwagi, "Prediction of Surge and its Effect on Added Resistance by Means of the Enhanced Unified Theory," *Trans West-Japan Society of Naval Architects*, no. 89, pp. 77-89, 1995.
- [25] A. Guha and J. Falzarano, "The effect of hull emergence angle on the near field formulation of added resistance," *Ocean Engineering*, vol. 105, pp. 10-24, 2015.

- [26] J. N. Newman and C. H. Lee, "Boundary-element methods in offshore structure analysis," *Journal of Offshore Mechanics and Arctic Engineering*, vol. 124, no. 2, pp. 81-89, 2002.
- [27] D. Bruzzone, C. Gironi, and A. Grasso, "Nonlinear effects on motions and loads using an iterative time-frequency solver," *International Journal of Naval Architecture and Ocean Engineering*, vol. 3, no. 1, pp. 20-26, 2011.
- [28] A. Grasso, D. Villa, S. Brizzolara, and D. Bruzzone, "Nonlinear motions in head waves with a RANS and a potential code," *Journal of Hydrodynamics*, vol. 22, no. 5 SUPPL. 1, pp. 172-177, 2010.
- [29] J. V. Wehausen and E. V. Laitone, "Surface Waves," vol. 9: Springer-Verlag, Berlin, 1960, pp. 446-778.
- [30] F. R. S. Sir Thomas Havelock, "Waves due to a floating sphere making periodic heaving oscillations," *Proceedings of the Royal Society of London. Series A. Mathematical and Physical Sciences*, vol. 231, no. 1184, pp. 1-7, 1955.
- [31] M. Kashiwagi, "Hydrodynamic study on added resistance using unsteady wave analysis," *Journal of Ship Research*, vol. 57, no. 4, pp. 220-240, 2013.

3. PRACTICAL APPROACH OF LINEAR HYDRO-ELASTICITY

EFFECT ON VESSEL WITH FORWARD SPEED IN THE

FREQUENCY DOMAIN

3.1. Background and Literature Review

Different from classical fluid-structure interaction where the structure is considered as one rigid body, hydroelasticity treats the structure as a deformable solid continuum with its own governing equation that is different from the surrounding fluid continuum. The elastic deformation of the body will change the body's total local displacement which in turn will displace the surrounding fluid differently compared to if we treated the structure as a non-deformable rigid body. Consequently, the resulting reaction force and the fluid's exciting force acting on the body will be effectively changed due to the deformation of the body as well. This coupling effect between the fluid and deformable body's interaction is the main focus of many hydroelasticity studies.

Unlike the traditional fluid-structure interaction that treats structures as a single rigid body, hydro-elasticity studies consider the structure as a deformable solid continuum that interacts with fluid motions. The elastic deformation of the structure can cause an appreciable change in local displacements, which in turn results in different behavior of surrounding fluid and the corresponding forces compared to the case of rigid body. Based on this theoretical background, many hydro-elasticity studies have been performed in the past several decades to explain the coupling effect between fluid motion and structural deformation [1].

The hydro-elasticity effect is largely dependent on structural deformability [2, 3]. In general, the larger the structure, the more difficult to be rigid. In recent years, Very Large Floating Structures (VLFSs) have attracted great attention due to increased interest in ocean-space utilization. Such structures include not only ship-shaped structures (e.g., Ultra Large Crude Carrier (ULCC) supertankers) but also other types of floating structures (e.g., floating bridges, floating airports, islands, storages, and floating solar power plants) [4]. These structures can be up to several kilometers in length and relatively low in stiffness compared to traditional offshore structures. Consequently, VLFSs require more elaborate hydro-elastic analysis to estimate their local displacements and structural behaviors during the design process. In addition, hydro-elasticity was also considered in several Wave Energy Converters (WECs) to accurately estimate their local load distribution and energy extraction [5, 6].

There are two popular numerical methods for hydro-elastic analysis: the modal superposition and direct methods. First, the modal superposition method calculates the generalized body coordinates and local normal directions of the structures by using rigid and elastic modes, and then the fluid dynamics solver utilizes these parameters to calculate wave and other fluid loads in each mode. Hydro-elastic deformation is then obtained by superposing the elastic responses obtained in each mode [2]. This method can further be categorized into dry and wet mode methods, depending on the method to acquire the elastic modes. For example, Newman [2], Senjanović et al. [7], and Fu et al. [8] selected the dry mode method in frequency-domain hydro-elastic analysis while the wet mode method [9-11], which additionally considers added mass and hydrostatic stiffness in modal analysis, was also incorporated in the frequency-domain hydro-elastic analysis. In some cases, the Finite Element Method (FEM) is required to obtain the structural mode shapes and natural frequencies of a complex structure with non-typical boundary conditions [8, 11, 12]. In

addition, the modal superposition method can be combined with the 3-dimensional (3D) hydrodynamic simulation program to estimate the interacting fluid loads in both frequency [2, 3, 13, 14] and time domains [13, 15-17]. In the time domain, this method was also utilized for load mapping of a deformable structure in random waves [18]. Second, the direct method couples the 3D FEM method with the 3D hydrodynamic simulation at each time step, which is numerically expensive but can be more robust [19-21]. This method has several advantages: no structural mode shape is required, non-linearity can be taken into consideration in the time domain, complex structural geometry can straightforwardly be incorporated, and local stresses can directly be estimated. In some cases, Computational Fluid Dynamics (CFD) and FEM are coupled for the hydro-elastic simulation, which is numerically very intensive [22]. A hybrid method, which combines these two methods, was also investigated by Jagite et al. [23]. Various hydro-elastic methods were reviewed in more detail in ref. [24-27].

Recently, a discrete-module-beam (DMB) method has been proposed for hydro-elastic analysis [1, 4, 28], which is different from the conventional modal-superposition and direct methods. In this approach, a deformable structure is discretized into multiple floating rigid modules while a stiffness matrix based on beam theory, such as the Euler-Bernoulli beam, equivalently representing the structure's stiffness, is employed to connect neighboring modules. No structure's modal characteristics are required with enough number of rigid modules, which can also save computational time and effort compared with the modal superposition method where iteration is needed to get wet modes. Hydro-elastic problems can then be solved in both frequency [1] and time [4, 28, 29] domains. In addition, Zhang and Lu [30] extended its application to a complex structural shape with the rigorous FEM simulation, in which the complex structural

stiffness is converted into equivalent beam stiffness. In the present hydro-elastic analysis, the DMB approach with multi-floater-module hydrodynamics is used.

The presence of uniform flow or forward speed of vessels poses additional difficulties. Ref. [19, 21, 31, 32] shows that the presence of uniform flow changes both the direction and magnitude of local loads on structures, which means that structural design and fatigue analysis need to take it into consideration. Numerical studies such as ref. [19, 21] took account of the uniform flow by means of full FEM-BEM coupling in the time domain, or time-domain BEM coupled with modal superposition method. Those methods are highly time-consuming and computationally very extensive. In order to make a more practical approach to consider the uniform flow effect on the linear hydro-elasticity problems, the present uniform-flow approximation [33-35] along with the DMB method is therefore proposed. Both uniform-flow approximation and DMB method can be applied as a post-processing after the multi-body diffraction/radiation problem in the frequency domain. Therefore, any multi-body wave diffraction/radiation simulation tools, such as the commercially available like WAMIT [36], can straightforwardly be used to solve the forward-speed hydro-elastic problem as presented in this paper despite that WAMIT was developed as zero-forward-speed code. Although multi-body wave-structure interaction is used both in the industry and academia, the same case with forward speed (or uniform current) is hard to find in the open literature. Using the developed computer program, the effects of forward speed or partial structural damage on the modal characteristic of elastic structures are also investigated. This might also be useful for future researches if the wave-current interaction model is to be paired with the modal superposition method. To summarize, the principal differences between the proposed method with the more rigorous FEM-BEM direct coupling methods as in ref. [19, 21, 31, 32] can

be found in Table 3.1. Various hydro-elastic analyses in the presence of forward speed using various different approaches can also be found in more detail in ref. [33, 37, 38].

Table 3.1. Summary of differences between the reference [19] and present methods

Physics	Das & Cheung [19]	Present Study
Structural Dynamics	3D shell finite element	Discrete 3D multi rigid bodies connected by equivalent beam elements
Wave Diffraction-Radiation	Boundary element method: <ul style="list-style-type: none"> • Rankine green function • Free surface and far-field discretization in box spatial domain 	Boundary element method: <ul style="list-style-type: none"> • Free surface Green Function • Body discretization only
Hydro-elastic Coupling	Direct FEM-BEM coupling in the frequency domain	External stiffness matrix on multi-body diffraction-radiation dynamics in the frequency domain
Wave-Current Interaction	<ul style="list-style-type: none"> • Steady double-body flow is considered in the boundary conditions and forces • Modification of free-surface waves by current is considered 	<ul style="list-style-type: none"> • Only the uniform-flow coupling effect is considered in the boundary conditions and forces • 0-speed free surface boundary condition approximation

3.2. Structural Dynamics and Hydro-elastic Coupling

3.2.1. Discrete Body Hydroelasticity Method (DBM)

The structural analysis part of the hydroelasticity problem is done using the equivalent beam theory based element. Just like on typical experimental set up (Fig.3.2), the VLFS is modeled as

interconnected M rigid body that are connected by beam elements that act as the “spine” of the whole structures. As its numerical representation, the stiffness of the whole structure will be represented as equivalent Euler-Bernoulli beam and Saint Venant’s torsional end node stiffness. A total of $M-1$ beam elements are needed to connect all the rigid bodies together, and individual beam is considered to be connected by a fixed end connection to a lumped mass that represents each rigid body. The end node stiffness obtained from the beam theory is then applied as external stiffness in our hydrodynamic model, thus completing the hydrodynamic and structural elasticity coupling.

The DMB method was first developed by Lu et al. [39] to simulate the linear hydro-elasticity problem by adopting a multi-rigid body approach. The concept of this approach is similar to the standard hydro-elasticity experiment’s set-up, where the floating body is partitioned into M number of sections that are connected to one another by beam elements to simulate its elastic behaviors as can be seen in Fig. 3.1. The blue lines illustrate the beam elements that are connected to two adjacent module’s center of gravities. A total of $M-1$ beam elements are needed to connect all the modules.

As can be seen in Fig. 3.1 Each module is treated as an independent rigid body with six degrees of freedom, expressed in their local coordinate system (x_n, y_n, z_n) . The interaction between one body and the others comes through the hydrodynamics interactions and the end node’s stiffness loading from the beam elements.

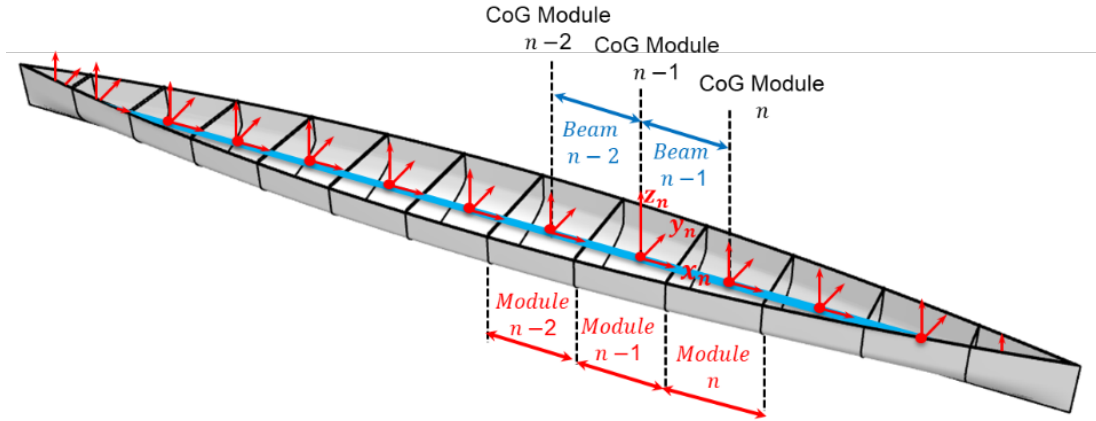


Fig. 3.1. Illustration of Discrete Module Beam (DMB) method

As its numerical representation, each module's distributed mass is modeled as a lumped mass located at its center of gravity, and the beam is modeled as the Euler-Bernoulli beam theory and Saint-Venant torsion model. This beam model is valid when the structure's plane sections remain plane (no shear deformation), and that deformed beam angles are small (linear). These assumptions are typically valid for slender structures with $EI/\kappa L_e^2 AG \ll 1$ that undergoes small deformations. Where E , I , κ , L_e , A and G are elastic modulus, second moment of area, shear coefficient, length of the beam, cross-section area of the beam, and the shear modulus respectively. The 12×12 equivalent end node axial, bending, and torsional stiffness of two interconnected structures in the local coordinate system can be formulated as follow [15]:

simplified approach to calculate the equivalent beam stiffness for ship-shaped structures based on the matching of fundamental modes is adopted in the present study.

3.2.2. Equation of Motions

The multi-body equation of motion in the frequency domain is used in this study and is formulated as follows:

$$[M + A(\omega_e)]\ddot{\eta} + [B(\omega_e)]\dot{\eta} + [K_h + K_E]\eta = F_d \quad (3.3)$$

$$(-\omega_e^2[M + A(\omega_e)] + i\omega_e[B(\omega_e)] + [K_h + K_E])\eta = F_d \quad (3.4)$$

where ω_e is the wave's encounter frequency, M , $A(\omega_e)$, $B(\omega_e)$, K_h , and K_E are the $6M \times 6M$ sectional mass, added mass, hydrodynamic damping, hydrostatic stiffness, and external stiffness matrices (with the number of modules, M), while η and F_d are the $6M \times 1$ motion and diffraction-force vectors, respectively. The total external stiffness matrix in global coordinate system K_E can be derived from the element's external stiffness matrix as follow:

$$K_E = \begin{bmatrix} K_1^{(11)} & K_1^{(12)} & 0 & \cdots & 0 \\ K_1^{(21)} & K_1^{(22)} + K_2^{(22)} & K_2^{(23)} & \cdots & 0 \\ 0 & K_2^{(32)} & K_2^{(33)} + K_3^{(33)} & \cdots & 0 \\ \vdots & \vdots & \vdots & \ddots & \vdots \\ 0 & 0 & 0 & \cdots & K_{M-1}^{(MM)} \end{bmatrix} \quad (3.5)$$

Note that all the local element stiffness matrices are converted into the global coordinate by utilizing directional cosine transformation matrices, i.e. $K_e^{(ii)} = T_e^T K_e'^{(ii)} T_e$ (with transformation matrix, T_e), as can be found in Wei et al. [1].

After solving the equation of motion, the vertical bending moment can be subsequently calculated by considering the internal force balance as follow:

$$F_{int} = K_E \eta = F_d - (-\omega_e^2 [M + A(\omega_e)] + i\omega_e B(\omega_e) + K_h) \eta \quad (3.6)$$

$$M_y(x) = \sum_{k=1}^K (x_g^{(k)} \leq x) \left(F_{int5}^{(k)} + F_{int3}^{(k)} \cdot (x - x_g^{(k)}) \right) \quad (3.7)$$

where F_{int} is the $6M \times 1$ structural loading vector, $F_{int5}^{(k)}$ is the internal y-moment of the kth body, $F_{int3}^{(k)}$ is the internal z-force of the kth body, x is the collocation point of the vertical bending moment, and $x_g^{(k)}$ is the location of the kth body's center of gravity. All of which are illustrated in Fig. 3.2. Illustration of bending moment on DMB method. Since the diffraction force, motion, added mass, radiation damping, and encounter frequency are affected by the uniform flow; the bending moment is expected to be changed as well.

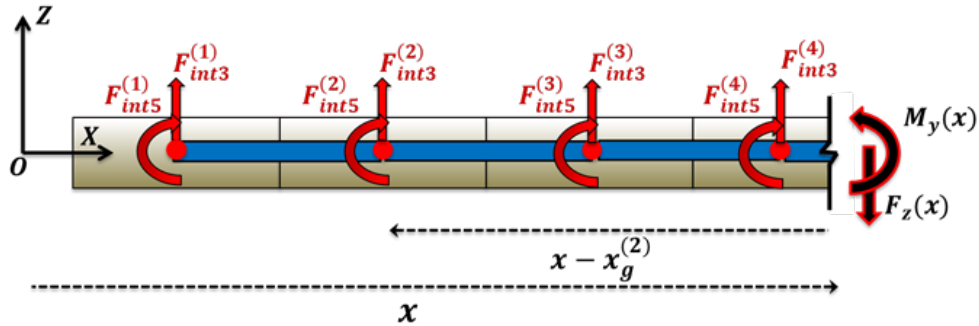


Fig. 3.2. Illustration of bending moment on DMB method

3.2.3. Modal Analysis

Modal analysis is done to see the effect of the uniform flow to the mode shape and natural frequency. Because DBM does not require the solving of modal analysis before any calculation can be done, the modal analysis can be done separately from the rest of calculation. The writer is

interested in investigating the change of modal characteristics due to uniform flow, because for the more popular modal superposition method, the mode shape is one of the determining factor. In addition, the modal characteristics can gives an overview on which part of the structure is expected to change the most due to the presence of the uniform flow.

DMB does not require solving mode shapes before hydro-elastic computation. The elastic behavior is considered by the multi-body dynamics that are coupled through the equivalent beam stiffness (see sub-section 2.1). The modal analysis, however, can be done separately for heuristic comparison. We primarily investigate the change of modal characteristics due to uniform flow (or forward speed) so that the users of the modal superposition method can have the relevant insight. In addition, the modal characteristics can give an idea on which part of the structure is changed the most due to the presence of the uniform flow. The natural frequencies are calculated as follows:

$$\det|-\omega_n^2[M + A(\omega_n)] + [K_h + K_E]| = 0 \quad (3.8)$$

Mode shapes are calculated as follows:

$$\{-\omega_{n_i}^2[M + A(\omega_{n_i})] + [K_h + K_E]\} \psi_i = 0 \quad (3.9)$$

where ω_{n_i} is the natural frequency of i^{th} mode and ψ_i is the mode-shape vectors of the i^{th} mode. Since the added mass $A(\omega_e)$ is affected by the uniform flow, the mode shapes and natural frequencies are expected to be changed as well. This kind of modal analysis, which considers the water-contact effect $[A(\omega_n)]$ and $[K_h]$, is called the wet-mode method. From eq.(3.9) above, we can see that in order to solve for ω_n , we need to know the added mass at ω_n , which is not known a priori. Thus to solve this problem, automated iteration method as can be seen on Fig.3.3. is employed.

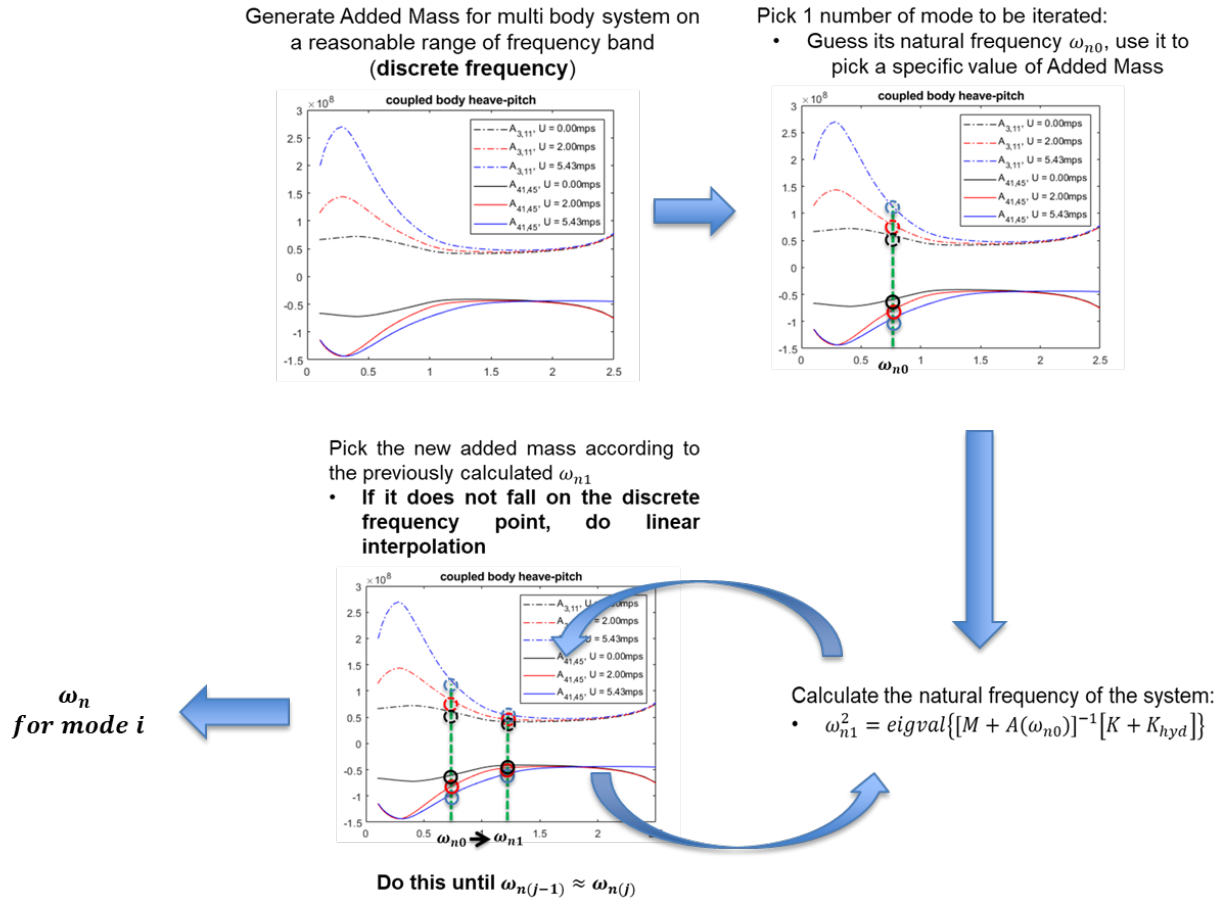


Fig. 3.3. Automated iteration method to solve the “wet” modal characteristics

3.3. Wave and Uniform Current Hydrodynamics

3.3.1. Boundary Value Problem for Multi Body Wave Interaction with Uniform Flow

In the DMB method, the structural elastic behavior is treated as relative motions among multiple floating sub-bodies; thus, the multi-body hydrodynamic model needs to be employed. Although multi-body wave-structure interaction is used both in the industry and academia, the same case with forward speed (or uniform current) like the present case is hard to find in the open literature. To shorten the notation, all first order wave potentials $\phi_w^{(1)}$ will be written only as ϕ_w , and the superscript will be used for the indexing of the discrete body instead. By separating the

problem into scattering and radiation problems, also by considering the uniform flow approximation, the 1st-order multi-body boundary conditions can be written as follows:

- Free surface boundary condition:

$$\left[g \frac{\partial}{\partial z} + \left(\frac{\partial}{\partial t} - U \frac{\partial}{\partial x} \right)^2 \right] \phi_w = 0 \quad \text{on } S_F(z = 0) \quad (3.10)$$

- Bottom boundary condition:

$$\frac{\partial \phi_w}{\partial z} = 0 \quad \text{on } S_h(z = -h) \quad (3.11)$$

- Body boundary condition of the scattering potential:

$$\frac{\partial \phi_s}{\partial n} = - \frac{\partial \phi_I}{\partial n} \quad \text{on } S_B^{(l)} \quad (3.12)$$

- Body boundary condition of the radiation potential:

$$\frac{\partial \phi_{rj}^{(k)}}{\partial n^{(l)}} = \begin{cases} n_j^{(k)} + \frac{U}{i\omega_e} m_j^{(k)} & \text{for } k = l \\ 0 & \text{for } k \neq l \end{cases} \quad \text{on } S_B^{(l)} \quad (3.13)$$

where,

$$(m_1^{(k)}, m_2^{(k)}, m_3^{(k)}) = (n^{(k)} \cdot \nabla) \nabla \phi_{st} \quad (3.14)$$

$$(m_4^{(k)}, m_5^{(k)}, m_6^{(k)}) = (n^{(k)} \cdot \nabla) \times (x \times \nabla \phi_{st})$$

For wave-uniform-flow interaction model, the m terms are reduced to:

$$m_j^{(k)} = (0, 0, 0, 0, n_3^{(k)}, -n_2^{(k)}) \quad (3.15)$$

For vessels without forward speed, the body boundary condition of the radiation potential

is reduced to:

$$\frac{\partial \phi_{rj}^{0(k)}}{\partial n^{(l)}} = \begin{cases} n_j^{(k)} & \text{for } k = l \\ 0 & \text{for } k \neq l \end{cases} \quad \text{on } S_B^{(l)} \quad (3.16)$$

- Far field boundary condition:

$$\lim_{|x| \rightarrow \infty} \sqrt{|x|} \left(\frac{\partial}{\partial t} - ik \right) \phi_w \quad \text{on } S_{|x| \rightarrow \infty} \quad (3.17)$$

All superscripts indicate the sub-body or module indices. By using eq.(3.16) (definition of $\phi_{rj}^{0(k)}$) and by substituting the m terms definition (eq.(3.15)) to the radiation body boundary conditions in eq.(3.13), the relation between the radiation potential with forward speed $\phi_{rj}^{(k)}$ and the radiation potential with zero forward speed $\phi_{rj}^{0(k)}$ can be written as follows:

$$\phi_{rj}^{(k)} = \begin{cases} \phi_{rj}^{0(k)} & \text{for } j < 5 \\ \phi_{rj}^{0(k)} + \frac{U}{i\omega_e} \phi_{r3}^{0(k)} & \text{for } j = 5 \\ \phi_{rj}^{0(k)} - \frac{U}{i\omega_e} \phi_{r2}^{0(k)} & \text{for } j = 6 \end{cases} \quad (3.18)$$

In the single-hull configuration, it is known that there is a coupling effect between the damping and the added mass term in the presence of forward speed [35]. The proposed multi-body formulation above ensures that this coupling effect is still considered when we treat the single-hull as a multi-body hull connected with the beam elements.

Just like on the previous section, the linear free surface boundary condition (eq.(3.10)) can be reduced back to the same form as the case without uniform flow, if $\omega_e \gg U(\partial/\partial x)$. This condition can be fulfilled if one or the combination of the following conditions is fulfilled: (1) high encounter frequency ω_e , (2) low uniform flow magnitude U, (3) slender body (or in other words $(\partial/\partial x)$ is small compared to the transversal derivatives). Considering all linearization and approximations above, notable advantages of using the Uniform Flow approximation are:

1. Zero-speed free surface green function can be used.

2. Only body boundary conditions need to be fulfilled by the radiation and scattering potentials. Therefore no free surface discretization is needed.
3. No additional steps compared to the 0-speed case are needed to solve the steady wave potentials.
4. The change in wave's diffraction forces, added mass, and hydrodynamic damping due to the wave-current interactions can be treated as correction terms to the 0-speed values.

The detailed derivation of the boundary conditions and m terms for a single rigid body can be found in [34, 35]. Therefore, ϕ_s can be obtained by solving the same body boundary condition as the one for the 0-speed case but evaluated at ω_e , and ϕ_I can be obtained as below:

$$2\pi\phi_s(x_i) + \sum_{j=1}^{Np} \phi_s(x_j) \frac{\partial G^0(k_e, x_j, x_i)}{\partial n_j} A_j = - \sum_{j=1}^{Np} \frac{\partial \phi_I}{\partial n} G^0(k_e, x_j, x_i) A_j \quad (3.19)$$

$$\phi_I = \frac{igA \cosh(k(z+h))}{\omega_0 \cosh(kh)} e^{-ik(x \cos \beta + y \sin \beta)} \quad (3.20)$$

where G^0 denotes the 0-speed free-surface green function, subscript i and j denotes the panel number, k_e denotes the wave number that corresponds to encounter frequency ω_e , Np denotes the total number of panels over the whole un-partitioned structures, A denotes the incident wave's amplitude, h denotes the water depth, k denotes the wave number that corresponds to the incident wave's frequency ω_0 , and β denotes the wave heading angle of incidence to the positive x -axis. The radiation wave potentials can be solved using eq.(3.19), but changing the right-hand side to the radiated wave's body boundary condition as in eq.(3.13).

All of the above means that any multi-body wave's diffraction-radiation simulation tools developed for rigid body and zero forward speed can be extended to the forward-speed case after

reasonably minor modifications. Then, it can be combined with the DMB method to solve the hydro-elasticity problem with forward speed.

3.3.2. Hydrodynamic Forces and Coefficients

Consider the 1st order hydrodynamic forces in eq.(2.13), and then decompose it into several components in the generalized multi-body degree of freedoms as follow:

$$F^{(k)} = F_I^{(k)} + F_S^{(k)} + F_h^{(k)} + \left[A^{(k,l)} - \frac{i}{\omega_e} B^{(k,l)} \right] \dot{\eta}^{(l)} \quad (3.21)$$

$$F_d^{(k)} = F_I^{(k)} + F_S^{(k)} \quad (3.22)$$

where F_I is the Froude-Krylov force (contribution from ϕ_I), F_S is the scattering force from ϕ_S terms, $(A^{(k,l)} - iB^{(k,l)}/\omega_e)$ are the added mass and hydrodynamic damping related to ϕ_r terms and F_h is the hydrostatic forces that consist of steady / lower-order terms. The mathematical definition of each of these terms can be found as follows:

- Incident wave exciting force:

$$\begin{aligned} F_I^{(k)} &= \rho \iint_{S_B^{(k)}} \left(\frac{\partial \phi_I}{\partial t} - U \frac{\partial \phi_I}{\partial x} \right) n^{(k)} dS \\ &= \rho \iint_{S_B^{(k)}} (i\omega_e - iUk \cos \beta) \phi_I n^{(k)} dS \\ &= i\omega_0 \rho \iint_{S_B^{(k)}} \phi_{w1} n^{(k)} dS \end{aligned} \quad (3.23)$$

- Scattered wave exciting force, with uniform flow correction:

$$F_S^{(k)} = \rho \iint_{S_B^{(k)}} \left(\frac{\partial \phi_S}{\partial t} - U \frac{\partial \phi_S}{\partial x} \right) n^{(k)} dS \quad (3.24)$$

The spatial derivative in the convective term can be avoided by utilizing Stoke's theorem, as shown in ref.[35, 40]

$$F_S^{(k)} = \rho \iint_{S_B^{(k)}} (i\omega_e n^{(k)} - Um^{(k)}) \phi_S dS \quad (3.25)$$

Or using the Haskind's relation, it can also be written as,

$$\begin{aligned} F_{Sj}^{(k)} &= -\rho \sum_{l=1}^M \iint_{S_B^{(l)}} \frac{\partial \phi_l}{\partial n^{(l)}} \phi_{r_j}^{0(k)} dS && \text{for } j = 1, 2, 3, 4 \\ &= -\rho \sum_{l=1}^M \left\{ \iint_{S_B^{(l)}} \frac{\partial \phi_l}{\partial n^{(l)}} \phi_{r_j}^{0(k)} dS + \frac{\rho U}{i\omega_e} \iint_{S_B^{(l)}} \frac{\partial \phi_l}{\partial n^{(l)}} \phi_{r_3}^{0(k)} dS \right\} && \text{for } j = 5 \\ &= -\rho \sum_{l=1}^M \left\{ \iint_{S_B^{(l)}} \frac{\partial \phi_l}{\partial n^{(l)}} \phi_{r_j}^{0(k)} dS - \frac{\rho U}{i\omega_e} \iint_{S_B^{(l)}} \frac{\partial \phi_l}{\partial n^{(l)}} \phi_{r_2}^{0(k)} dS \right\} && \text{for } j = 6 \end{aligned} \quad (3.26)$$

- Added mass and hydrodynamic damping with uniform flow correction:

$$F_R^{(k)} = F_{Rj}^{(k)} = \sum_{j=1}^6 \left(A_{ij}^{(k,l)} - \frac{i}{\omega_e} B_{ij}^{(k,l)} \right) \ddot{\xi}_j^{(l)} \quad (3.27)$$

By rewriting the force definition in eq.(2.13) into the generalized multi-body degree of freedoms, and then utilizing Stoke's theorem as shown in ref.[35, 40]

$$\left(A_{ij}^{(k,l)} - \frac{i}{\omega_e} B_{ij}^{(k,l)} \right) = \rho \iint_{S_B^{(k)}} (i\omega_e n_i^{(k)} - Um_i^{(k)}) \phi_{r_j}^{(l)} dS \quad (3.28)$$

The equation above can be written in terms of its relationship with the added mass and hydrodynamic damping without uniform flow as below:

$$\left(A_{ij}^{0(k,l)} - \frac{i}{\omega_e} B_{ij}^{0(k,l)} \right) = \rho \iint_{S_B^{(k)}} (i\omega_e n_i^{(k)}) \phi_{wrj}^{0(l)} dS \quad (3.29)$$

- For $i \leq 4$ and $j = 5$

$$A_{i5}^{(k,l)} = A_{i5}^{0(k,l)} - \frac{U}{\omega_e^2} B_{i3}^{0(k,l)} \quad (3.30)$$

- For $i = 5$ and $j \leq 4$

$$A_{5j}^{(k,l)} = A_{5j}^{0(k,l)} + \frac{U}{\omega_e^2} B_{3j}^{0(k,l)} \quad (3.31)$$

$$B_{i5}^{(k,l)} = B_{i5}^{0(k,l)} + UA_{i3}^{0(k,l)}$$

$$B_{5j}^{(k,l)} = B_{5j}^{0(k,l)} - UA_{3j}^{0(k,l)}$$

○ For $i \leq 4$ and $j = 6$

○ For $i = 6$ and $j \leq 4$

$$A_{i6}^{(k,l)} = A_{i6}^{0(k,l)} + \frac{U}{\omega_e^2} B_{i2}^{0(k,l)} \quad (3.32)$$

$$A_{6j}^{(k,l)} = A_{6j}^{0(k,l)} - \frac{U}{\omega_e^2} B_{2j}^{0(k,l)} \quad (3.33)$$

$$B_{i6}^{(k,l)} = B_{i6}^{0(k,l)} - UA_{i2}^{0(k,l)}$$

$$B_{6j}^{(k,l)} = B_{6j}^{0(k,l)} + UA_{2j}^{0(k,l)}$$

○ For $i = 5$ and $j = 5$

$$A_{55}^{(k,l)} = A_{55}^{0(k,l)} - \frac{U}{\omega_e^2} B_{53}^{0(k,l)} + \frac{U}{\omega_e^2} B_{35}^{0(k,l)} + \frac{U^2}{\omega_e^2} A_{33}^{0(k,l)} \quad (3.34)$$

$$B_{55}^{(k,l)} = B_{55}^{0(k,l)} + UA_{53}^{0(k,l)} - UA_{35}^{0(k,l)} + \frac{U^2}{\omega_e^2} B_{33}^{0(k,l)}$$

○ $i = 6$ and $j = 6$

$$A_{66}^{(k,l)} = A_{66}^{0(k,l)} + \frac{U}{\omega_e^2} B_{62}^{0(k,l)} - \frac{U}{\omega_e^2} B_{26}^{0(k,l)} + \frac{U^2}{\omega_e^2} A_{22}^{0(k,l)} \quad (3.35)$$

$$B_{66}^{(k,l)} = B_{66}^{0(k,l)} - UA_{62}^{0(k,l)} + UA_{26}^{0(k,l)} + \frac{U^2}{\omega_e^2} B_{22}^{0(k,l)}$$

On the single-body model, $B_{ij}^0 - B_{ji}^0$ and $A_{ij}^0 - A_{ji}^0$ typically cancel each other. However, since $B_{ij}^{0(k,l)} - B_{ji}^{0(k,l)}$ and $A_{ij}^{0(k,l)} - A_{ji}^{0(k,l)}$ consist of 2 different body's interaction, it will give non-zero results and need to be taken into consideration.

3.4. Validations

3.4.1. Case Definition

Shallow draft elastic barge, as defined in Yago & Endo [41], is used to validate the DMB method against their experiment data in the case of zero forward speed. The hull shape and particulars can be seen in Table 3.2 and Fig. 3.4 below. This particular case is used due to the availability of the experiment data.

Table 3.2. Main particulars of the shallow-draft barge case

Item	Notation	Value	Unit
Length	L	300.0	m
Breadth	B	60.0	m
Depth	h_{bm}	2.0	m
Draft	D	0.5	m
Water depth	h	58.5	m
Mass	M_{tot}	9.225×10^6	kg
Vertical bending stiffness	EI_y	4.77×10^{11}	N·m ²
Poisson Ratio	ν	0.3	-
NBODY	M	8	-
Minimum wave length	λ_{min}	120	m
Wave Heading	β	0	deg

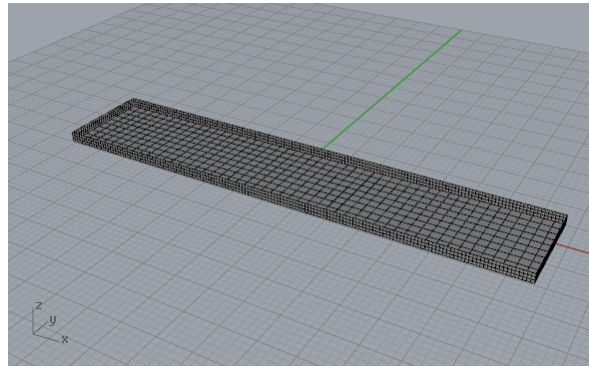


Fig. 3.4. Shallow-draft barge shape as defined in Yago & Endo [41]

Analytical Wigley Hull, as defined in Riggs et al. [42] and Das & Cheung [19], is also used as another comparative study against their linear hydro-elasticity models. This case study is chosen because of several reasons, such as:

1. Both references used different approaches compared to the present study; Riggs et al. [42] used modal superposition and generalized coordinate body boundary conditions, while Das & Cheung [19] used shell element FEM and Rankine panel BEM directly coupled, which is computationally very intensive.

2. Das & Cheung's [19] method is to be more accurate than the present method, thus can serve as a good benchmark. However, the present methodology is way more practical than their method to be incorporated into early design processes.
3. The hull is designed specifically to accentuate the effect of linear hydro-elasticity so that the hydro-elastic behavior can clearly be seen in the global analysis.

As an illustration for points 1 and 2, the free-surface and far-field panels used in Das & Cheung [18] significantly increase the size of linear equations compared to the present method. Also, their FEM computations with shell elements take much more time than the present DMB method.

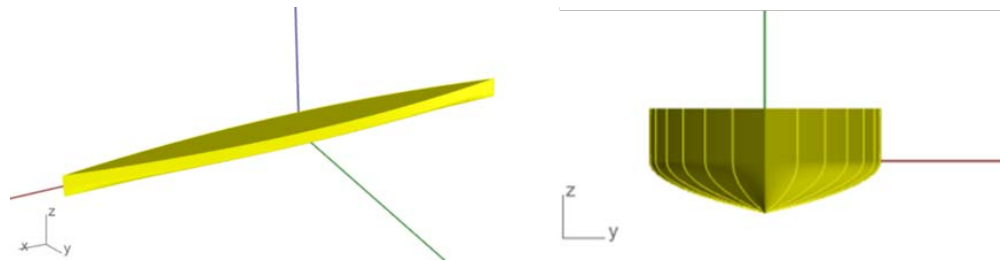


Fig. 3.5. Wigley hull shape as defined in Riggs et. al. [42]

Table 3.3. Main particulars of Wigley hull case

Item	Notation	Value	Unit
Length	L	100	m
Breadth	B	10	m
Total Depth	h_{bm}	4.5	m
Draft	d	2.25	m
Water depth	h	Inf	m
Displaced Volume	∇	1000	m^3
Deck's mass density	ρ_s	76,857	kg/m^3
Deck's thickness – mass	t_m	0.02	m
Deck's thickness – stiffness	t_{k-deck}	0.25	m
Hull's thickness – stiffness	t_{k-hull}	0.15	m
Elastic Modulus	E	7.5	GPa
Poisson Ratio	ν	0.3	--
NBODY	M	21	-
Minimum wave length	λ_{min}	6.5	m
Wave Heading	β	180	deg

The Wigley-hull shape can be seen in Fig. 3.5, the main particulars of its FEM models Das & Cheung [19] can be seen in Table 3.3, and the wetted area of the hull is described in eq.(3.36). The hull is extended vertically above the water plane to reach the total height.

$$y = \frac{1}{2}B \left(1 - \left(\frac{2x}{L}\right)^2\right) \left(1 - \left(\frac{z}{d}\right)^2\right) \quad (3.36)$$

For the shallow draft barge case, the structure is considered to have a uniform beam stiffness and mass distribution, as defined in Table 3.2. Because of these considerations, the geometric properties I_y, I_z, I_p of the barge can be simply calculated, i.e. $I_y = Bh_{bm}^3 / 12$ and so forth.

For Wigley Hull case in both Riggs [42] and Das & Cheung [19], the hull's stiffness is modeled as equivalent hull and deck stiffness so that internal stiffeners and bulkheads are still taken into account, even without modeling them directly with FEM. For the DMB method, however, we only need to calculate equivalent beam geometric properties I_y^*, I_z^*, I_p^* so that they can best represent the FEM structure as close as possible. The most robust approach to find these equivalent properties for complex structures can be found in Zhang & Lu [30], where they modeled the structures using FEM and then used the end-node forces to back-calculate the end node stiffness, which has the same form as eq.(3.5).

To simplify the approach, we consider the equivalent beam geometric properties as the geometric properties of the cross-section of the hull on each section multiplied by a factor α , such that $I_y^* = \alpha \cdot I_y$ (see Fig. 3.6). To find α , we match the first two natural periods of the vertical bending modes of the beam with the values calculated using FEM, and keep the error below 10%. To reduce the complexity of the problem in determining equivalent stiffness of DMB, the first two

modes are matched. However, as can be seen from the results, this consideration already gave good agreement with the more rigorous FEM results.

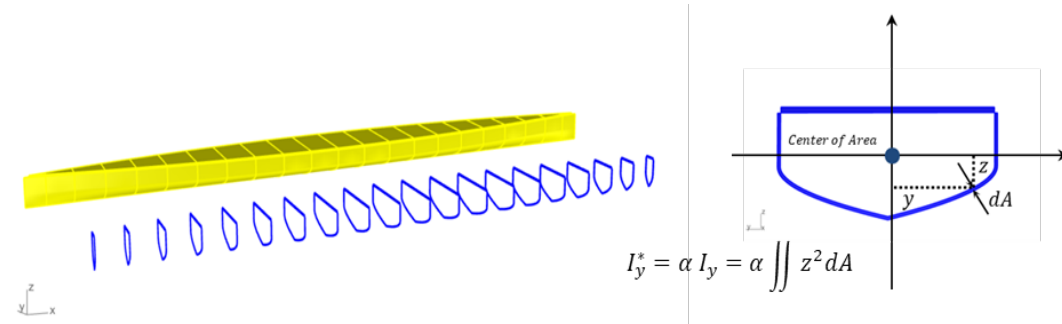


Fig. 3.6. Cross sections of the structures, and geometric properties definitions

From the matching of the first two vertical bending modes, $\alpha = 12.3$ is used, and the resulting I_y^*, I_z^*, I_p^* and the dry natural periods of the vertical bending modes for NBODY = 21 case can be seen in Table 3.4 and Table 3.5. The convergence with increasing NBODY was tested with 7, 14, and 21 sub-bodies, and satisfactory convergence was achieved beyond 14 sub-bodies. Thus 21 sub-bodies were used.

Table 3.4. Equivalent geometry for equivalent beam model

Beam #	I_y^*	I_z^*	I_p^*	L_{beam}
1	0.3881	0.08408	297.4125	4.2262
2	0.5925	0.3095	308.9748	4.6545
3	0.7875	0.6947	293.4534	4.7152
4	0.9622	1.2110	256.4946	4.7353
5	1.1135	1.8118	206.2381	4.7443
6	1.2404	2.4399	150.8212	4.7490
7	1.3423	3.0345	97.4637	4.7517
8	1.4190	3.5386	52.1230	4.7533
9	1.4702	3.9045	19.3430	4.7542
10	1.4961	4.0979	2.1816	4.7547

Table 3.5. Dry natural period comparisons between FEM model and equivalent beam model

Vertical Bending Mode #	T_n FEM (sec) Riggs et. al. [42]	T_n DBM (sec) Present Study	Err (%)
1	2.15	2.17	0.93%
2	1.00	0.91	-9.00%

Only the first 10 equivalent beam geometric properties are shown in Table 3.4 because of the symmetry of the ship with respect to the y-axis.

3.4.2. Validation of DMB Hydro-elasticity Model for Zero Forward Speed Case

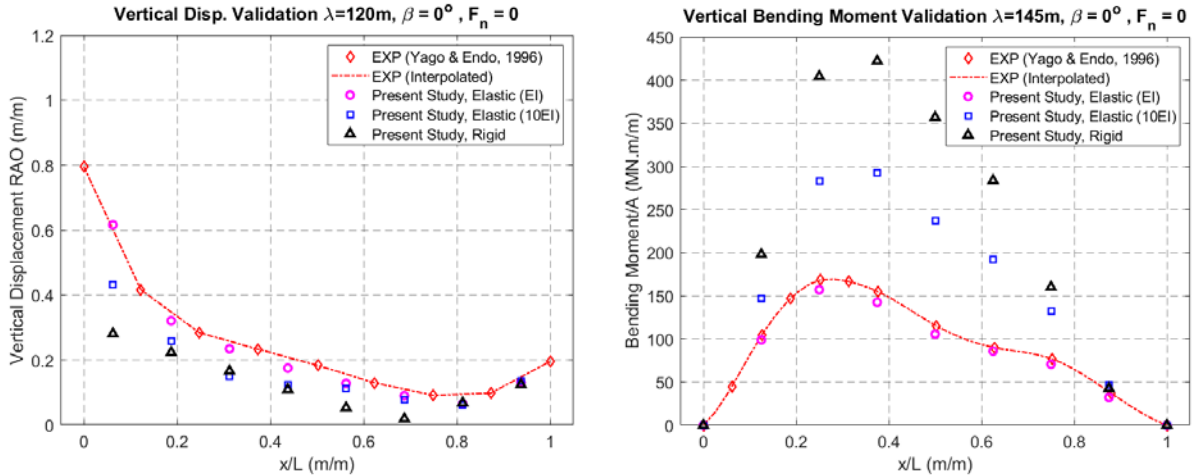


Fig. 3.7. Vertical displacement and bending moment validation for shallow barge case

From Fig. 3.7, we can see that the DMB method matches very well with the experimental data of Yago & Endo [41] for the barge case. It is clear from the figure that hydro-elasticity changes the vertical displacements non-uniformly from bow to stern compared to those of rigid body. The elasticity also causes the bending moment to be smaller than that of rigid body. Higher structural stiffness increases the bending moments and decreases the vertical displacements. Sensitivity

analysis on the number of modules can be found in Jin et al. [29], in which to catch all essential dynamics, each module length needs to be at least $L_m < \lambda_{min}$.

For the Wigley hull case, the present DMB model is compared with the modal-superposition method and direct FEM-BEM coupling method. Using the present DMB model, the first two wet natural periods without forward speed are found to be 7.13 sec (i.e., coupling between roll and horizontal bending mode) and 3.85 sec (i.e., coupling between heave and vertical bending mode) respectively, which is a good match with the FEM results from Riggs et al. [42].

The rigid body case is simulated by the same hydro-elasticity model, with a very high elastic modulus $E_{rigid} = 100$ GPa. For the DMB, the vertical stern and bow displacements are obtained by combining the pitch and heave modes as follows:

$$Z^{Stern} = \xi_3^1 + \sin(\alpha_2^1) \frac{L_1}{2} \quad (3.37)$$

$$Z^{Bow} = \xi_3^{NBODY} - \sin(\alpha_2^{NBODY}) \frac{L_{NBODY}}{2} \quad (3.38)$$

where ξ_3^k , α_2^k , and L_i are the heave RAO, pitch RAO, and length of body section of the k^{th} body. Fig. 3.8 shows the comparisons of vertical displacements at three locations between the present hydro-elastic method with other hydro-elastic approaches when forward speed is zero. We first see that the present rigid case agrees well with the rigid FEM case of [19, 42]. The present elastic case also agrees very well with the more rigorous approach of direct FEM-BEM coupling in Das & Cheung [19].

At the bow and stern locations, when compared with more rigorous FEM-BEM direct coupling [19], the present DMB hydro-elastic method (black) provides better results than the conventional hydro-elastic analysis based on the modal-superposition method (yellow) [42]. Das & Cheung [19]

stated that these discrepancies might be caused by the fact that the modal superposition method has to use discrete elastic modes (21 in total for this reference). However, the present DMB hydro-elasticity method with the same 21 units produced as good results as Das & Cheung [19], which implies that the difference was not caused by discrete elastic modes. We suggest that the use of less accurate wet modes in [42] may be the reason for the discrepancy. The hydro-elasticity effect generally decreases the vertical displacements on the bow and stern locations and increases the vertical displacement at the midship location.

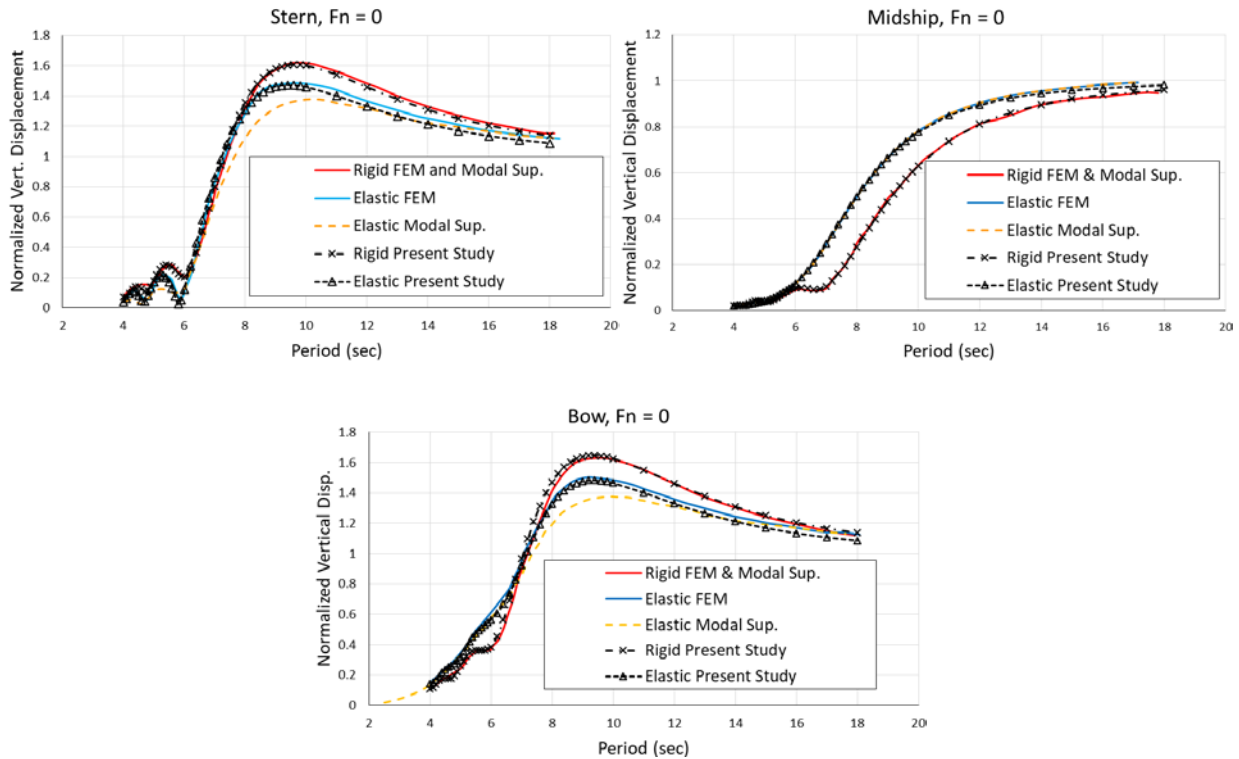


Fig. 3.8. Wigley hull hydro-elastic model comparisons for zero forward speed case. The FEM results are from ref. [19], while the modal superposition results are from ref. [42]

3.4.3. Validation of DMB Hydro-Elasticity Model with Forward Speed Case

For the same reason as explained in section 4.2, the Wigley hull case from Riggs et al. [48] and Das & Cheung [19] is used as the test case of the present linear hydro-elasticity with forward

speed. The slender ship shape is also well suited for the present uniform-flow approximation model. The present hydro-elastic results are compared against more rigorous FEM-BEM direct-coupling method of Das & Cheung [19]. To highlight the differences of hydro-elastic effects between the two methods, the hydro-elastic effects are plotted with respect to the same base case of rigid body [19].

Fig. 3.9 shows the comparison for head wave with the forward speed of $F_n = 0.3$ ($U = 9.4 \text{ m/s}$) and Wigley hull shape is considered. The differences in methodology between the reference method (blue line) and the present method (red line) are highlighted in Table 3.1.

From Fig. 3.9, it can be seen that both present and reference results show very similar elastic effects even when forward speed is considered, except near the bow. The discrepancies near the bow can be attributed to the stronger influence of steady flow and the resulting difference in relative wave elevation there, which is originated from the approximations in the free surface boundary condition in the present study. However, the overall marginal differences between the reference and the present study suggest that we achieved the intended result with considerably less effort and computational burden.

In general, both methods show that the hydro-elasticity effect causes larger vertical displacement compared to the rigid body case except $\lambda/L > 0.7$ at bow. The encounter frequency, convective pressure, and m-terms contribute to their changes. Interestingly, there is a distinct high peak on $\lambda/L \approx 0.35 - 0.4$ region due to structural elasticity. These peaks do not occur in the case of rigid body with forward speed or elastic body without forward speed (Fig. 3.8). The peak at $\lambda/L \approx 0.35 - 0.4$ represents resonance i.e. the wave encounter frequency coincides with the natural frequency of first pure bending mode. Therefore, we can conclude that for elastic

structures, it is important to consider both forward speed and hydro-elasticity effects to be able to capture all important structural dynamics correctly.

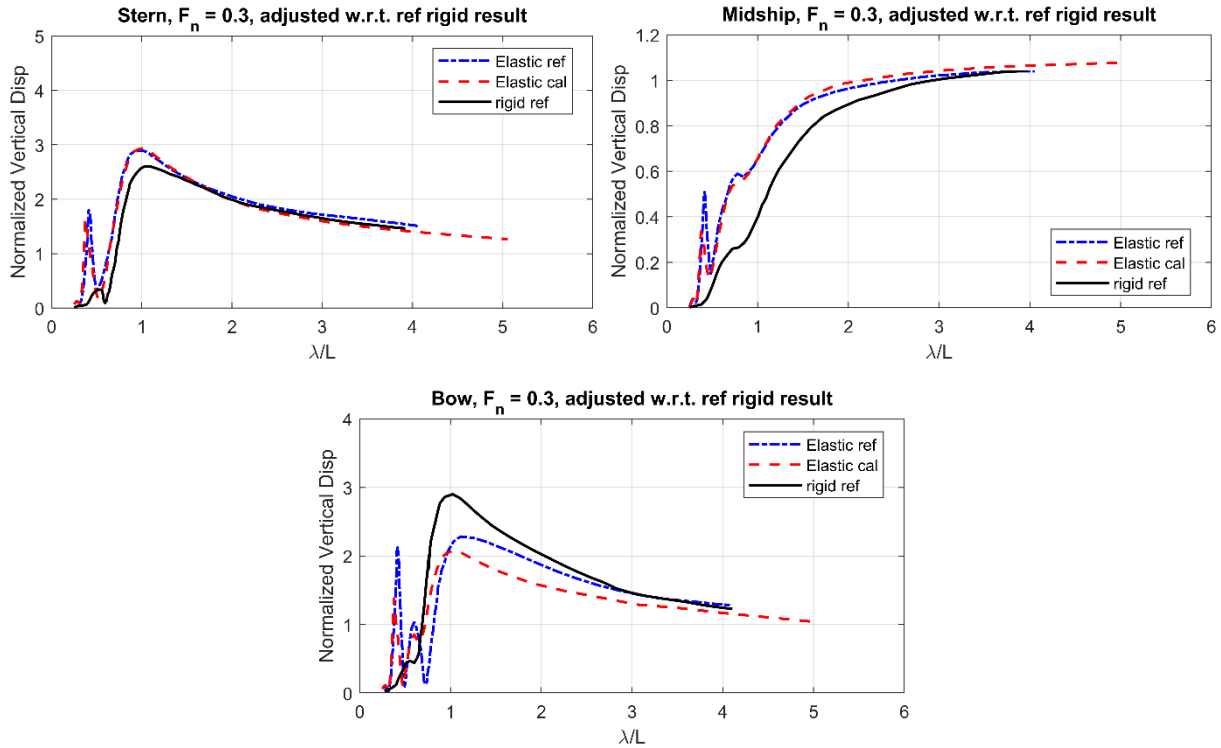


Fig. 3.9. Elasticity effect with forward speed with respect to the rigid-body base of [19]

3.5. Parametric Study on the Forward Speed Effect on the Ship Hydro-elastic Behavior

3.5.1. Forward Speed Effect on the Modal Characteristics

From Table 3.6, we can see the effects of forward speed and water contact on the natural frequencies of elastic modes. The hydrostatic stiffness and added mass cause the natural periods of the 2nd and 3rd elastic modes to be slightly higher when compared to the dry modes. On the other hand, the forward-speed effect only causes a very small change to the natural period of the 1st bending mode, while its effects on the higher bending modes are negligible. This is because the

added-mass correction with forward speed diminishes as the period becomes smaller, i.e., added mass at very high-frequency region is almost constant (high-frequency limit).

From Fig. 3.10, we can see how all the mode shapes (1st, 2nd, 3rd bending) are affected by the water-contact effect, marking the importance of the inclusion of hydrostatic force and added mass when the modal superposition method is used. On the other hand, the change by forward speed is negligible except for the 1st bending mode. The 1st vertical bending mode is warped towards downstream direction when forward speed effect is considered. The modal-superposition method has to figure out this kind of modal change in a priori, which is not necessary for the present DMB-based hydro-elasticity analysis. That can be considered as an advantage compared to the traditional modal-superposition-based hydro-elastic analysis.

Table 3.6. The forward-speed and water-contact effects on the natural periods of Wigley hull

Mode #	Dry Mode	Wet Mode $F_n = 0.0$	Wet Mode $F_n = 0.3$
1 st Vertical Bending	2.17 sec	2.19 sec	2.27 sec
2 nd Vertical Bending	0.90 sec	1.21 sec	1.22 sec
3 rd Vertical Bending	0.51 sec	0.70 sec	0.71 sec

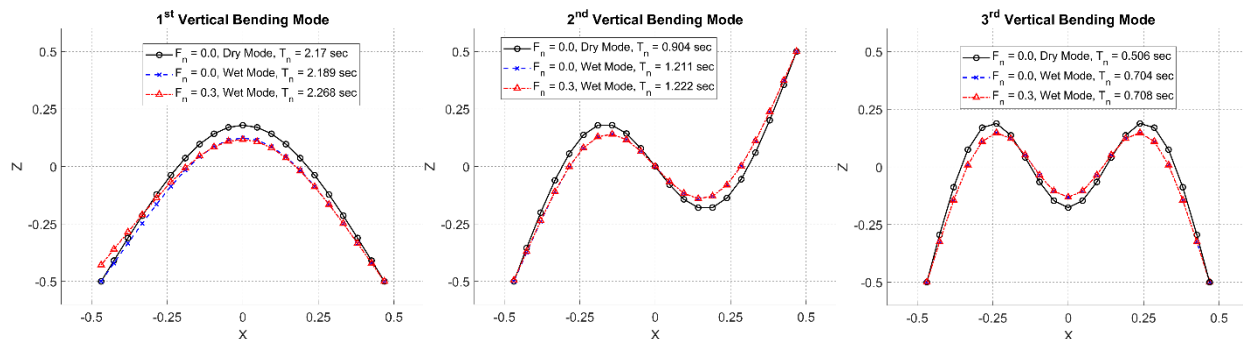


Fig. 3.10. The forward-speed and water-contact effects on the mode shapes of Wigley hull

The warping of the first bending mode shape with forward speed occurs because of the change of the added mass by the forward speed, as can be seen in Fig. 3.11. From eq.(3.28)-(3.35), it is clear that the forward speed affected the added mass through the encounter frequency, the body boundary condition (e.g., the m terms), and the convective term in the Bernoulli's pressure.

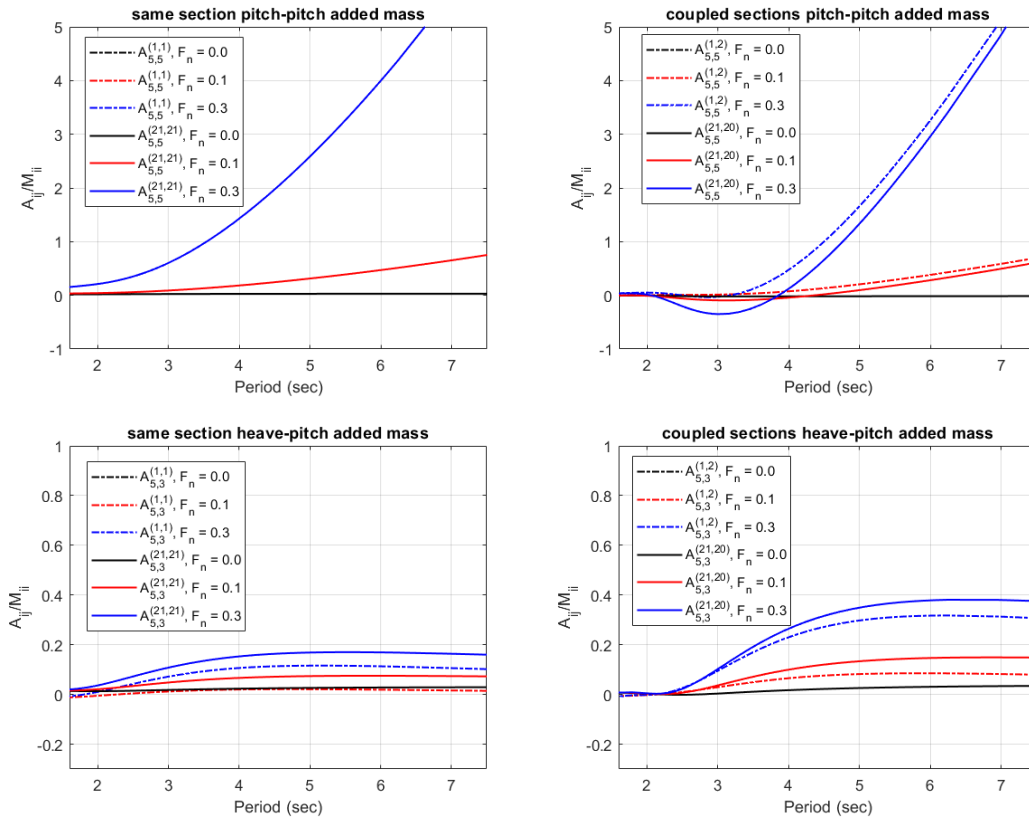


Fig. 3.11. The forward speed effect on the Wigley hull added mass (subscript index=mode, superscript index=section; superscript 1,2 means hydrodynamic interaction between section 1 and 2; subscript 5,3 means pitch-heave mode coupling)

From Fig. 3.11, we can see how the pitch or pitch-heave added mass is affected by the forward speed for sub-body 1 and 21 or by hydrodynamic multi-body coupling between sub-body 1-2 and 20-21. Their differences are large at larger wave periods with increasing forward speed but become small at small wave periods less than 2s regardless of forward speed. This explains why there are no mode shape warps on the higher bending modes.

From the modal analysis, we conclude that the changes of the lowest elastic natural frequencies and natural modes are mainly due to the change of added-mass coefficients depending on forward speed if $T_n > 2s$. This conclusion is especially important when one is trying to solve the hydro-elastic problem with forward speed by the modal superposition method. Note that in the DMB method, no prior knowledge of natural modes is necessary when directly solving for the elastic dynamic responses and stresses.

3.5.2. Forward Speed Effect on the Vertical Bending Moment

The results for vertical bending moments of the Wigley hull can be seen in Fig. 3.12 and Fig. 3.13. For $F_n = 0.0 - 0.2$, the maximum vertical bending over the whole ship's length can be found when $\lambda \cong 0.72L$ while for $F_n = 0.3$, the maximum vertical bending occurs when $\lambda \cong 0.36L$ because the bending moment by the higher-frequency elastic mode (i.e. first vertical bending mode) takes over that by the pitch-resonance motion (see rigid vs. elastic mode in Fig. 3.9). All the vertical bending moment peaks are located at the mid-ship section. However, there are possibilities of the emergence of primary and secondary peaks not located at the mid ship section (e.g. , $\lambda \cong 0.47L$; $\lambda \cong 0.36L$ & $U < 6.3\text{m/s}$ etc.), as shown in Fig. 3.13. For $\lambda \cong 0.36L$ and $\lambda \cong 0.72L$, the bending moments monotonically increase with increasing forward speed but in other λ s, it is not necessarily so.

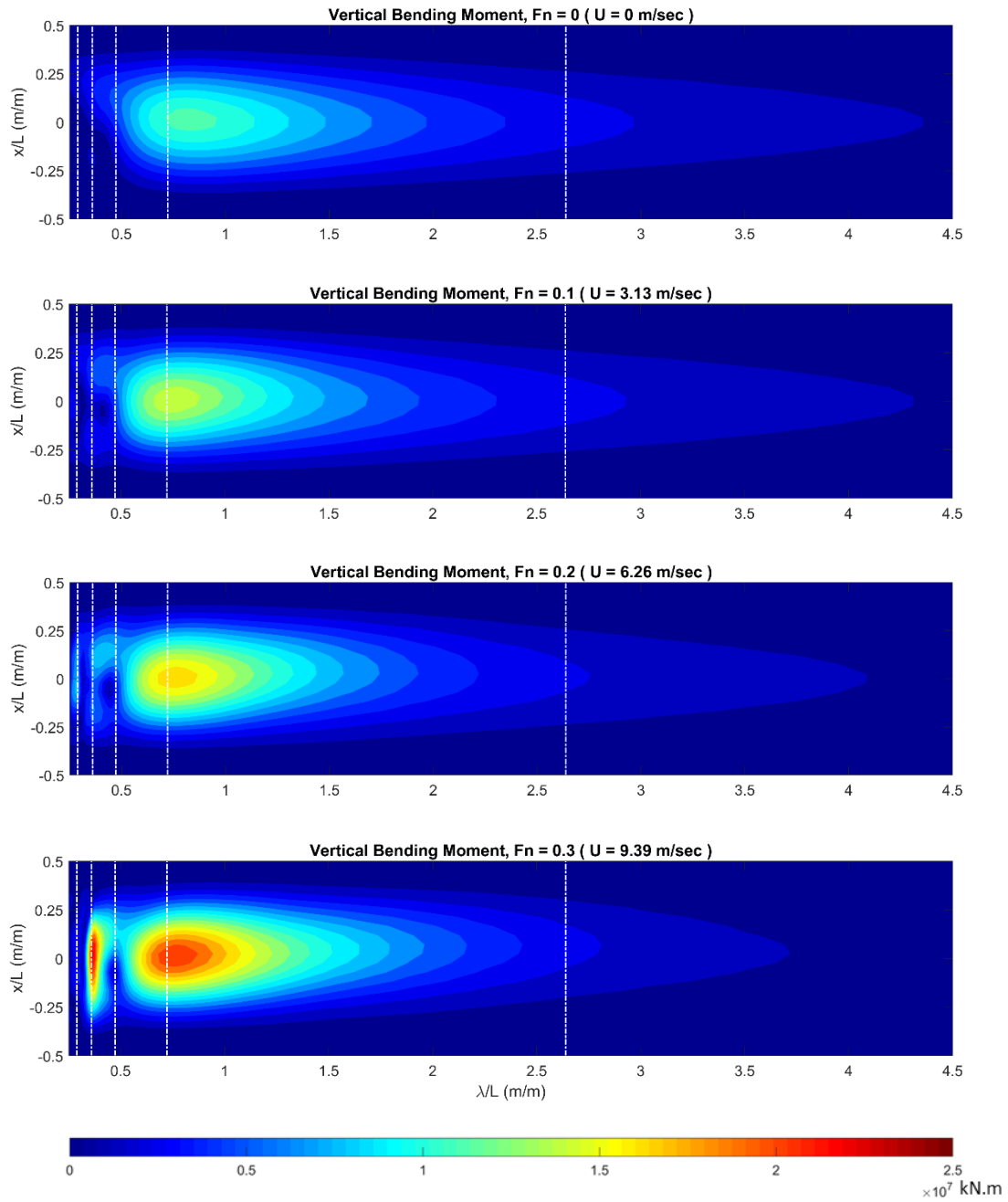


Fig. 3.12. Vertical bending moments of Wigley hull depending on the wave length, location of the ship's section, and forward speed

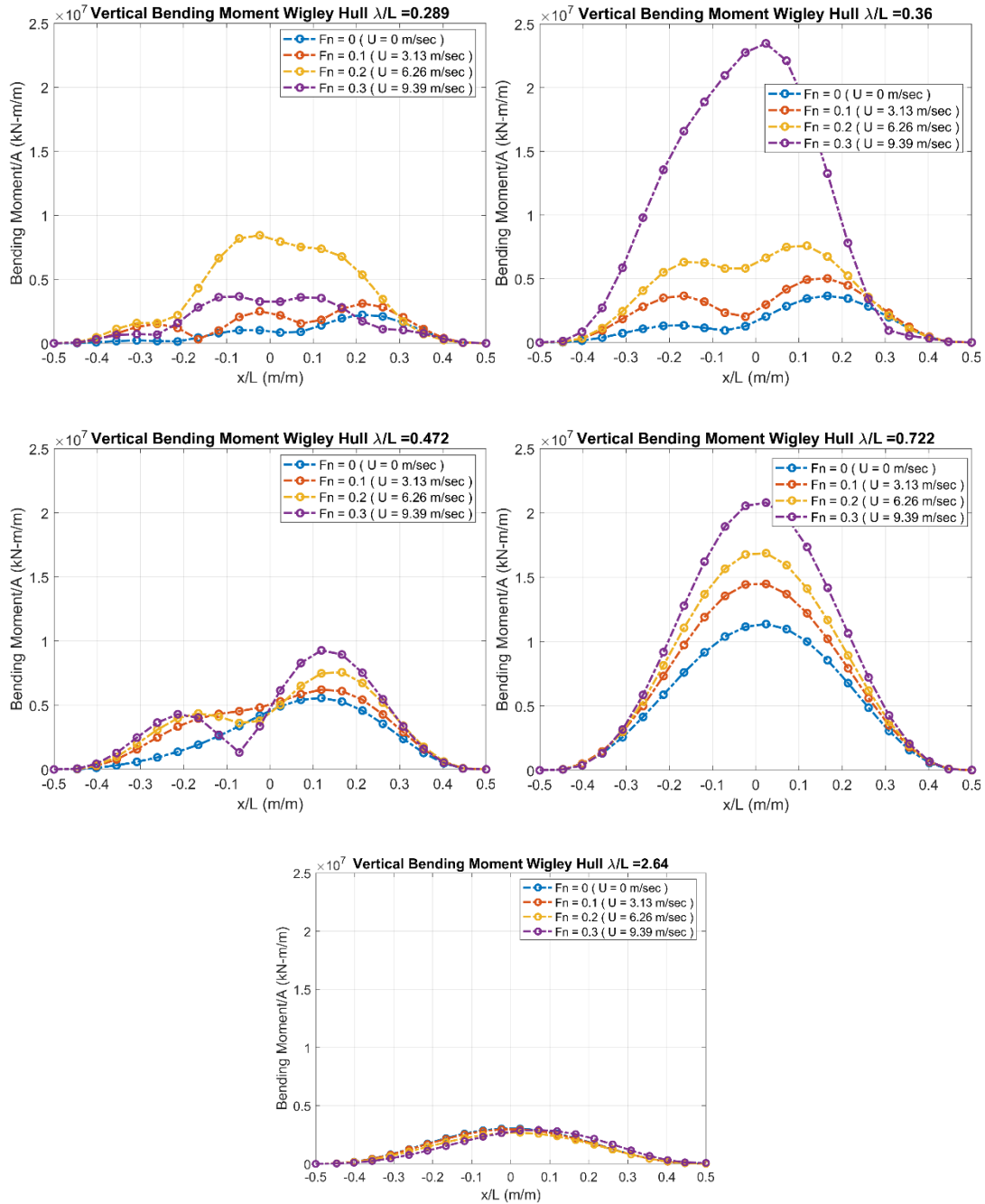


Fig. 3.13. Vertical bending moments along the length of Wigley hull for various wave lengths and forward speeds

The encounter wave period plays an important role, especially for short waves of $\lambda < 0.5L$. For example, the maximum bending moment for $F_n = 0.3$ occurred when $\lambda = 0.36L$ or $T_e = 2.2 \text{ sec}$, which coincides with the 1st bending mode. Another example is when $\lambda = 0.29L$, for which the bending moment for $F_n = 0.2$ was found to be larger than that for $F_n = 0.3$. The reason is that $\lambda = 0.29L$ corresponds to the encounter period of $T_e = 2.2 \text{ sec}$ for $F_n = 0.2$, thus causing resonant responses of 1st bending mode. With $F_n = 0.3$, $T_e = 1.8 \text{ sec}$, which is away from any elastic natural periods. When $\lambda \gg 2L$ the body can be considered as a heaving-only rigid body, thus the elastic effects and bending moments will be small and the effect of forward speed can no longer be seen, as can be observed in the last figure.

3.5.3. Forward Speed Effect on Hydro-elastic Response in Random Waves

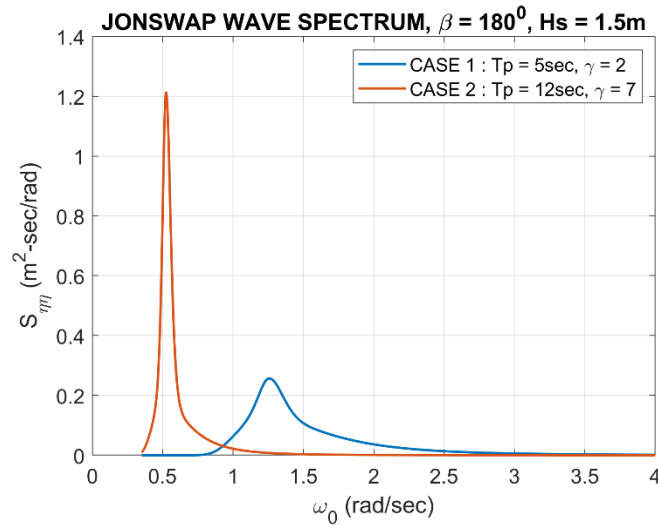


Fig. 3.14. Two wave spectra used in random wave simulation

Two different JONSWAP random-wave spectra as defined in Fig. 3.14 are used. The case of $T_p = 12 \text{ sec}$, $H_s = 1.5\text{m}$, and $\gamma = 7$ represents swell condition, while that of $T_p = 5 \text{ sec}$, $H_s = 1.5\text{m}$, and $\gamma = 2$ represents an ordinary operational condition (Sea State 3). Both cases are for head-sea condition. The resulting statistical values of Wigley-hull case can be seen in Table 3.7.

Table 3.7. Statistical values from the random wave simulation results

F_n	CASE	T_{pe} (sec)	M_y - max (kN-m)	σM_y (kN-m)	Max heave ξ_3 (m)	$\sigma \xi_3$ (m)
0.0	$T_p = 5$ sec $\gamma = 2$	5.00	0.57×10^7	0.95×10^6	0.076	0.019
0.1		3.57	0.74×10^7	1.18×10^6	0.075	0.023
0.2		2.77	1.10×10^7	1.60×10^6	0.113	0.030
0.3		2.27	1.61×10^7	2.67×10^6	0.159	0.052
0.0	$T_p = 12$ sec $\gamma = 7$	12.00	0.75×10^7	1.39×10^6	0.785	0.271
0.1		10.28	0.80×10^7	1.49×10^6	0.798	0.277
0.2		8.99	0.89×10^7	1.62×10^6	0.808	0.287
0.3		7.99	1.03×10^7	1.93×10^6	0.855	0.300

From the table, we can see that both the maximum and standard deviation (σ in Table 8) of the bending moment M_y always increase with forward speed. The bending moment becomes the largest in short waves at the highest speed (see Fig. 3.15 and Fig. 3.18) i.e. this is the most serious case for mid-ship fatigue damage in view of larger stresses at higher frequencies (see Fig. 3.16). The heave motion changes very little with forward speed when the encounter period (T_{pe}) is larger than 3.5s but changes considerably when the encounter period is small and the forward speed is high. The heave motion does not necessarily translate into elastic motion, and vice versa. The maximum bending moments and vertical displacements, as can be seen in three consecutive time series snapshots, are given along the length of the hull in Fig. 3.15 for various forward speeds and two wave spectra.

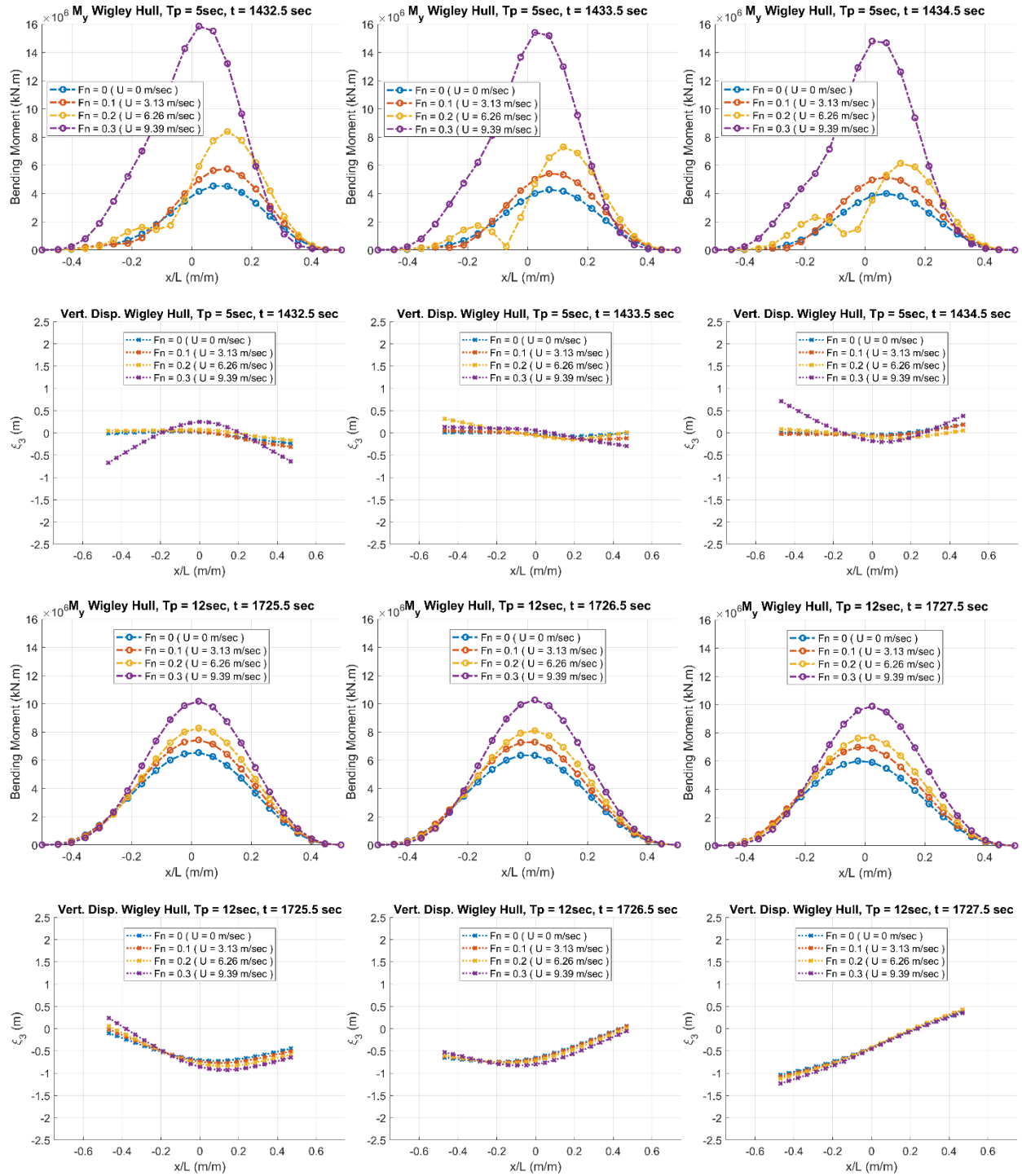


Fig. 3.15. Three consecutive time series snapshots of the Wigley hull's maximum M_y and vertical displacements for various forward speeds and two different wave spectra

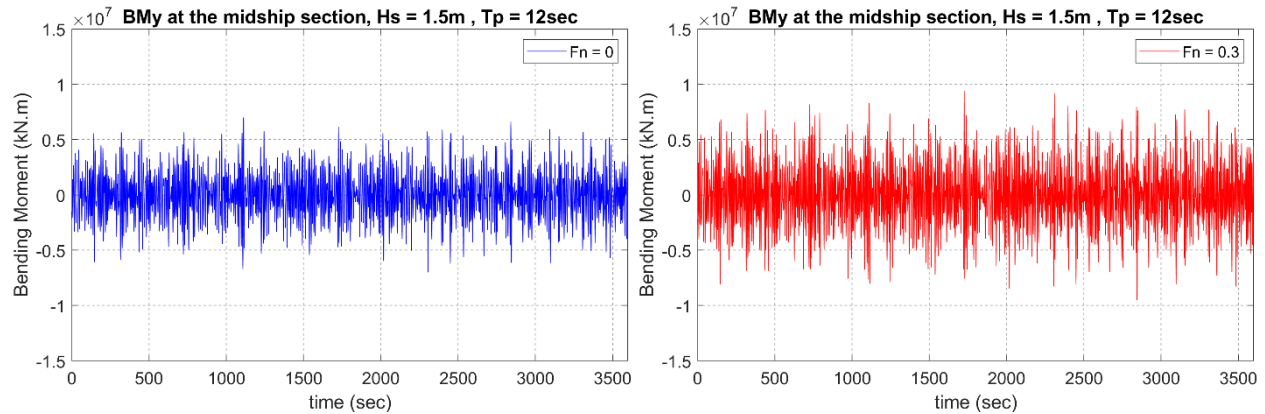


Fig. 3.16. Time series of bending moments at mid-ship with (right) and without (left) forward speed in swell sea

Looking at the results for the two different wave spectra, we can see that for low forward speed, the swell case causes the ship to have larger M_y , while for high forward speed the operational-sea case causes the ship to have larger M_y . This occurs because on the operational sea with high forward speed, the corresponding encounter period becomes closer to the resonance period of the lowest elastic mode. This enlarged elastic responses (see also Fig. 3.18) can directly be seen in the corresponding snapshots (second row of Fig. 3.15; purple color) of vertical displacements. The increase of bending moments with forward speed can be seen more directly in Fig. 3.16 (swell sea) and Fig. 3.18 (operational sea). Again, the significant increase with forward speed in the operational sea is noticeable. The time series were generated with random phases from the response and bending-moment spectra by using the respective RAOs (response amplitude operators) calculated from the present DMB method.

3.5.4. Additional Demonstration of the Present Method's Practicality: Damaged Hull Simulation

As can be found in ref. [1, 29], the DMB method provides a simple way to change the local structure characteristics (e.g., stiffness) to simulate various types of conditions or damages on the hull. Therefore, to further demonstrate the practicality of the present DMB method, a damaged hull case is simulated for the Wigley hull (Fig. 3.5 and Table 3.3) i.e. the mid-ship section of the hull is considered to be partially damaged. The damaged hull is modeled by lowering the beam stiffness connected to body no.11 by 30% (0.7EI). The resulting modal characteristic of the damaged hull case with and without forward speed can be seen in Fig. 3.17 and Table 3.8.

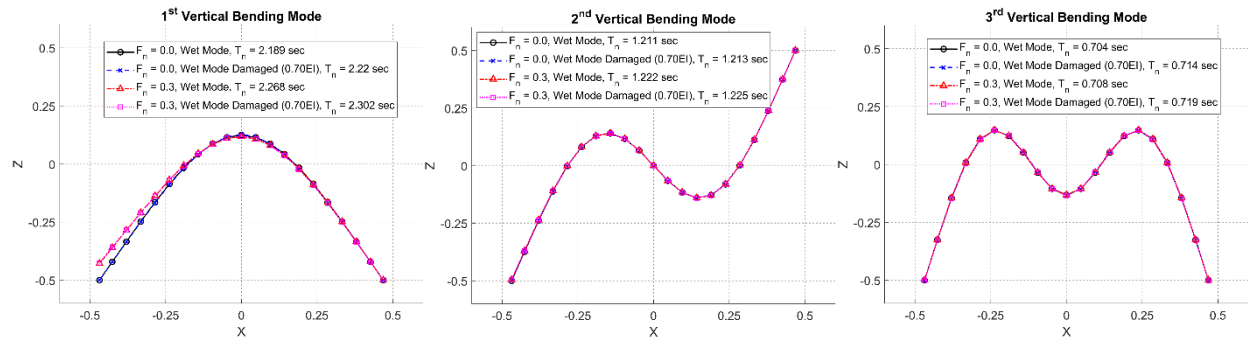


Fig. 3.17. The damaged hull effect on the wet modes of Wigley hull

Table 3.8. The damaged hull effect on the wet natural periods of Wigley hull

Mode #	$F_n = 0.0$		$F_n = 0.3$	
	No Damage	Damaged (0.7E)	No Damage	Damaged (0.7E)
1 st Vertical Bending	2.1893 sec	2.2202 sec	2.2683 sec	2.3015 sec
2 nd Vertical Bending	1.2106 sec	1.213 sec	1.2224 sec	1.2248 sec
3 rd Vertical Bending	0.7036 sec	0.714 sec	0.7076 sec	0.7189 sec

From Fig. 3.17 and Table 3.8, the local damage does not appear to affect the mode shapes regardless of forward speed. The forward speed only alters the lowest wet bending mode through the change of added mass, as was observed in the previous section. Since the global mode shapes are not affected by the local damage, the case is hard to be detected/analyzed by the conventional modal-superposition approach in solving hydro-elasticity. The natural periods are slightly shifted to higher values when the damage is imposed due to the loss of local stiffness. The anti-symmetric mode is more affected by the damage since there is no curvature on the damaged location for the symmetric mode. The largest change to the natural period occurred on the 3rd bending mode with forward speed, where the natural period is shifted by 1.6%. The forward-speed effect shifted the natural period up to 3.6% when compared to the stationary case. It means that the shift in natural frequency on seafaring vessel, does not necessarily translate into damage occurrence.

Note that the damaged hull implementation on the DMB method is straight-forward since it only needs to convert the corresponding local stiffness. Fig. 3.18 and Fig. 3.19 shows the comparisons of bending moments (or bending stresses) near the damage location between the intact and locally-damaged hull. Appreciable differences can be observed for the high-frequency oscillation in the forward speed case. This kind of change in stress-sensor signals may be used for the structural health monitoring [43].

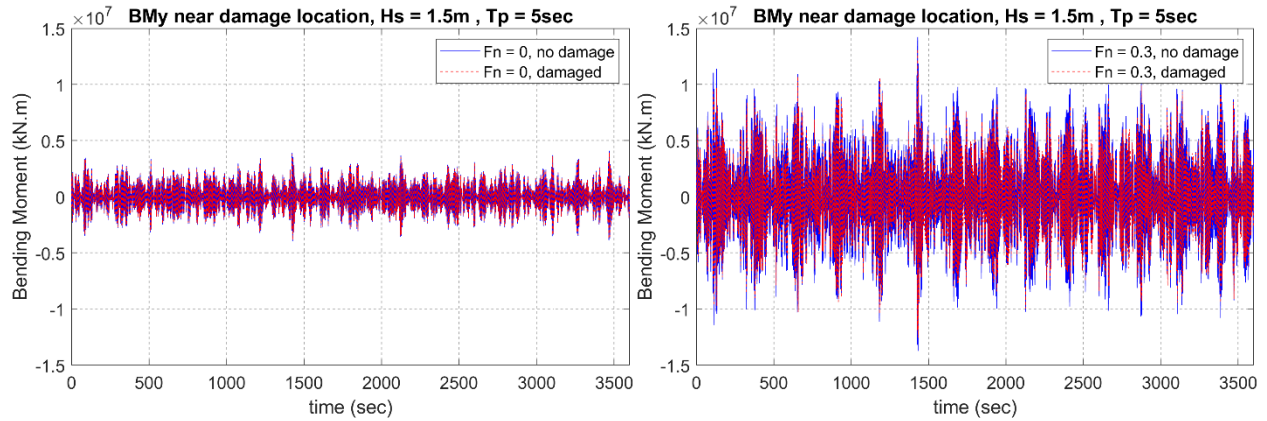


Fig. 3.18. Time series of bending moments at mid-ship with (right) and without (left) forward speed and with (red) and without (blue) damage in operational sea

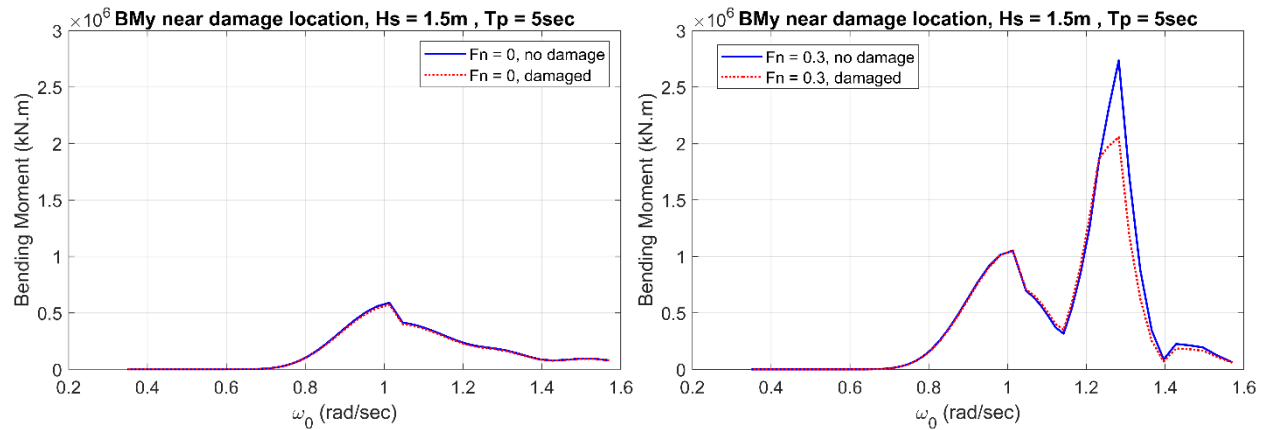


Fig. 3.19. Frequency domain analysis of bending moments at mid-ship with (right) and without (left) forward speed and with (red) and without (blue) damage in operational sea

3.6. Conclusions

A multi-body uniform-flow-based wave-current interaction hydrodynamic model was developed. Coupled with the DMB (Discrete-Module-Beam)-based hydro-elasticity method, the aforementioned model can be used as a practical and efficient numerical tool for the hydro-elastic analyses with forward-speed effect. The present hydro-elasticity model produced very accurate results when compared with the direct but much more time-consuming BEM-FEM coupling

method in the case of $F_n = 0$. Also, the present uniform-flow-based wave-current interaction model compared well with published experimental and computational results in the case of rigid Wigley hull with and without forward speed. The developed model successfully captured the increase of elastic responses and bending moments by forward speed especially due to the resonance at the first bending mode. Also, with forward speed $F_n = 0.3$, the dynamic vertical displacements at mid-ship and stern increased for the whole wave frequency range but those at bow decreased when $\lambda > 0.7L$ as a result of hull elasticity when compared with the rigid-hull case.

From the modal characteristic analysis of the Wigley hull, there exist appreciable differences between the dry and wet natural modes and the corresponding natural frequencies up to high bending modes. The same conclusion was also presented by various studies that used different approaches, namely in [44, 45]. The forward speed effect (up to $F_n = 0.3$) on the natural period and the mode shape was nontrivial at the first bending mode but negligible at higher bending modes. Due to forward speed, the lowest mode shape is warped towards the downstream direction, making the application of the conventional modal superposition method not straightforward. When the hydro-elasticity is solved by the modal superposition method, all the modal shapes should be obtained a priori. On the other hand, the present DMB method solves the hydro-elastic problem more directly without that kind of pre-process.

The maximum dynamic bending moment occurred at the mid-ship section when $\lambda \gg 0.5L$. However, when $\lambda < 0.5L$, higher elastic modes can be excited to change the location of the maximum bending moment. The bending moment (or stress) magnitudes tended to increase with forward speed although exceptions existed. The same tendencies were also observed in the case of two random waves considered. The increase of bending moments with forward speed in the

operational sea was more pronounced than the swell sea because of the encounter frequencies getting close to the first bending resonance. This kind of phenomenon is important in view of fatigue damage since both stress level and number of cycles are increased.

The 30% local damage at the mid-ship did not change the mode shapes while a bit altering the elastic-mode natural frequencies. The damaged hull implementation on the DMB method is straightforward since it only needs to convert the corresponding local stiffness. More noticeable differences in bending stresses near the damage location can be observed especially with forward speed. This kind of change in stress signals may be used for the structural health monitoring with the help of the big data produced by the present hydro-elastic simulation program.

In conclusion, the presently developed multi-body uniform-flow-based hydrodynamic model coupled with the DMB method showed promise to be a highly efficient, practical tool to solve rather complicated hydro-elasticity problem with forward speed. Nonetheless, due to several pragmatic approximations, care should be exercised when applying the proposed method especially when the steady free surface effect is large (e.g., close to the bow), hull shape is not slender, and uniform flow speed is large. More studies and comparisons are needed to investigate the validity of the proposed method, especially in the random sea case and the structural damage assessment case.

3.7. References

- [1] W. Wei, S. Fu, T. Moan, Z. Lu, and S. Deng, "A discrete-modules-based frequency domain hydroelasticity method for floating structures in inhomogeneous sea conditions," *Journal of Fluids and Structures*, vol. 74, pp. 321-339, 2017.
- [2] J. N. Newman, "Wave effects on deformable bodies," *Applied Ocean Research*, vol. 16, no. 1, pp. 47-59, 1994.

- [3] H. Y. Kang and M. H. Kim, "Hydroelastic analysis and statistical assessment of flexible offshore platforms," *International Journal of Offshore and Polar Engineering*, vol. 24, no. 1, pp. 35-44, 2014.
- [4] X. Zhang, D. Lu, Y. Gao, and L. Chen, "A time domain discrete-module-beam-bending-based hydroelasticity method for the transient response of very large floating structures under unsteady external loads," *Ocean Engineering*, vol. 164, no. May, pp. 332-349, 2018.
- [5] H. Zhang, D. Xu, R. Ding, H. Zhao, Y. Lu, and Y. Wu, "Embedded Power Take-Off in hinged modularized floating platform for wave energy harvesting and pitch motion suppression," *Renewable Energy*, vol. 138, pp. 1176-1188, 2019.
- [6] X. Zhang, S. Zheng, D. Lu, and X. Tian, "Numerical investigation of the dynamic response and power capture performance of a VLFS with a wave energy conversion unit," *Engineering Structures*, vol. 195, no. February, pp. 62-83, 2019.
- [7] I. Senjanović, Š. Malenica, and S. Tomašević, "Investigation of ship hydroelasticity," *Ocean Engineering*, vol. 35, no. 5-6, pp. 523-535, 2008.
- [8] S. Fu, T. Moan, X. Chen, and W. Cui, "Hydroelastic analysis of flexible floating interconnected structures," *Ocean Engineering*, vol. 34, no. 11-12, pp. 1516-1531, 2007.
- [9] E. Loukogeorgaki, C. Michailides, and D. C. Angelides, "Hydroelastic analysis of a flexible mat-shaped floating breakwater under oblique wave action," *Journal of Fluids and Structures*, vol. 31, pp. 103-124, 2012.
- [10] C. Michailides, E. Loukogeorgaki, and D. C. Angelides, "Response analysis and optimum configuration of a modular floating structure with flexible connectors," *Applied Ocean Research*, vol. 43, pp. 112-130, 2013.
- [11] T. Hamamoto and K. Fujita, "Wet-Mode Superposition for Evaluating the Hydroelastic Response of Floating Structures with Arbitrary Shape," *Proceedings of the International Offshore and Polar Engineering Conference*, vol. 12, pp. 290-297, 2002.
- [12] I. Senjanović, M. Tomić, and S. Tomašević, "An explicit formulation for restoring stiffness and its performance in ship hydroelasticity," *Ocean Engineering*, vol. 35, no. 13, pp. 1322-1338, 2008.
- [13] S. Malenica, B. Molin, F. Remy, and I. Senjanović, "Hydroelastic response of a barge to impulsive and non-impulsive wave loads," The Oxford University, Oxford, UK, pp. 107-116.
- [14] H. I. Wu, X. j. Chen, H. p. Shen, and Y. s. Wu, "Experimental and numerical investigation of the hydroelasticity of a floating structure with legs," *Marine Structures*, vol. 61, no. May, pp. 100-118, 2018.
- [15] F. Kara, "Time domain prediction of hydroelasticity of floating bodies," *Applied Ocean Research*, vol. 51, pp. 1-13, 2015.

- [16] S. Rajendran and C. Guedes Soares, "Numerical investigation of the vertical response of a containership in large amplitude waves," *Ocean Engineering*, vol. 123, pp. 440-451, 2016.
- [17] S. Seng, J. J. Jensen, and Š. Malenica, "Global hydroelastic model for springing and whipping based on a free-surface CFD code (OpenFOAM)," *International Journal of Naval Architecture and Ocean Engineering*, vol. 6, no. 4, pp. 1024-1040, 2014.
- [18] H. Y. Kang and M. H. Kim, "Time-domain hydroelastic analysis with efficient load estimation for random waves," *International Journal of Naval Architecture and Ocean Engineering*, vol. 9, no. 3, pp. 266-281, 2017.
- [19] S. Das and K. F. Cheung, "Hydroelasticity of marine vessels advancing in a seaway," *Journal of Fluids and Structures*, vol. 34, no. June, pp. 271-290, 2012.
- [20] I. Jae, E. Soo, and S. Hong, "A 3D direct coupling method for steady ship hydroelastic analysis," *Journal of Fluids and Structures*, vol. 94, pp. 102891-102891, 2020.
- [21] K. H. Kim, J. S. Bang, J. H. Kim, Y. Kim, S. J. Kim, and Y. Kim, "Fully coupled BEM-FEM analysis for ship hydroelasticity in waves," *Marine Structures*, vol. 33, pp. 71-99, 2013.
- [22] P. Lakshminarayanan, P. Temarel, and Z.-M. Chen, "Coupled fluid structure interaction to model three-dimensional dynamic behaviour of ship in waves," *7th International Conference on Hydroelasticity in Marine Technology*, pp. 623-636, 2015.
- [23] G. Jagite, X. D. Xu, X. B. Chen, and Š. Malenica, "Hydroelastic analysis of global and local ship response using 1D-3D hybrid structural model," *Ships and Offshore Structures*, vol. 13, pp. 37-46, 2018.
- [24] W. G. Price, M. A. Salas, and P. Tamarel, "The dynamic behaviour of a mono-hull in oblique waves using two- and three-dimensional fluid structure interaction models," *Transactions of the Royal Institution of Naval Architects*, vol. 144, pp. 1-26, 2002.
- [25] S. E. Hirdaris and P. Temarel, "Hydroelasticity of ships: Recent advances and future trends," *Proceedings of the Institution of Mechanical Engineers Part M: Journal of Engineering for the Maritime Environment*, vol. 223, no. 3, pp. 305-330, 2009.
- [26] X. J. Chen, Y. S. Wu, W. C. Cui, and J. J. Jensen, "Review of hydroelasticity theories for global response of marine structures," *Ocean Engineering*, vol. 33, no. 3-4, pp. 439-457, 2006.
- [27] S. E. Hirdaris *et al.*, "Loads for use in the design of ships and offshore structures," *Ocean Engineering*, vol. 78, pp. 131-174, 2014.
- [28] W. Wei, S. Fu, T. Moan, C. Song, and T. Ren, "A time-domain method for hydroelasticity of very large floating structures in inhomogeneous sea conditions," *Marine Structures*, vol. 57, no. October 2017, pp. 180-192, 2018.

- [29] C. Jin, F. P. Bakti, and M. H. Kim, "Multi-floater-mooring coupled time-domain hydroelastic analysis in regular and irregular waves," *Applied Ocean Research*, vol. 101, no. May, pp. 102276-102276, 2020.
- [30] X. Zhang and D. Lu, "An extension of a discrete-module-beam-bending-based hydroelasticity method for a flexible structure with complex geometric features," *Ocean Engineering*, vol. 163, no. May, pp. 22-28, 2018.
- [31] Y. Lee, N. White, Z. Wang, S. Zhang, and S. E. Hirdaris, "Comparison of springing and whipping responses of model tests with predicted nonlinear hydroelastic analyses," *International Journal of Offshore and Polar Engineering*, vol. 22, no. 3, pp. 209-216, 2012.
- [32] Y. L. Shao and O. M. Faltinsen, "A numerical study of the second-order wave excitation of ship springing in infinite water depth," *Proceedings of the Institution of Mechanical Engineers Part M: Journal of Engineering for the Maritime Environment*, vol. 226, no. 2, pp. 103-119, 2012.
- [33] R. E. D. Bishop, W. G. Price, and Y. Wu, "A General Linear Hydroelasticity Theory of Floating Structures Moving in a Seaway," *Philosophical Transactions of the Royal Society of London*, vol. 316, pp. 375-426, 1986.
- [34] R. Timman and J. Newman, "The Coupled Damping Coefficients of a Symmetric Ship," *Journal of Ship Research*, 1963.
- [35] N. Salvesen, E. Tuck, and O. Faltinsen, "Ship motions and sea loads," vol. 78, ed, 1970, pp. 250-287.
- [36] W. Inc, "WAMIT 6.2 User Manual."
- [37] K. H. Shin *et al.*, "Two- and three-dimensional springing analysis of a 16,000 TEU container ship in regular waves," *Ships and Offshore Structures*, vol. 10, no. 5, pp. 498-509, 2015.
- [38] J. H. Kim and Y. Kim, "Prediction of extreme loads on ultra-large containerships with structural hydroelasticity," *Journal of Marine Science and Technology (Japan)*, vol. 23, no. 2, pp. 253-266, 2018.
- [39] D. Lu, S. Fu, X. Zhang, F. Guo, and Y. Gao, "A method to estimate the hydroelastic behaviour of VLFS based on multi-rigid-body dynamics and beam bending," *Ships and Offshore Structures*, vol. 14, no. 4, pp. 354-362, 2016.
- [40] T. Ogilvie and E. Tuck, "A rational strip theory of ship motions: part I," ed, 1969, pp. 107-107.
- [41] K. Yago and H. Endo, "On the Hydroelastic Response of Box-Shaped Floating Structure with Shallow Draft," *Journal of the Society of Naval Architects of Japan*, vol. 1996, no. 180, pp. 341-352, 1996.

- [42] H. R. Riggs, K. M. Niimi, and L. L. Huang, "Two benchmark problems for three-dimensional, linear hydroelasticity," *Journal of Offshore Mechanics and Arctic Engineering*, vol. 129, no. 3, pp. 149-157, 2007.
- [43] H. C. Kim, M. H. Kim, and D. E. Choe, "Structural health monitoring of towers and blades for floating offshore wind turbines using operational modal analysis and modal properties with numerical-sensor signals," *Ocean Engineering*, vol. 188, no. July, pp. 106226-106226, 2019.
- [44] E. Loukogeorgaki, C. Michailides, and D. C. Angelides, "'Dry" and "wet" mode superposition approaches for the hydroelastic analysis of floating structures," *Proceedings of the International Conference on Structural Dynamic , EURODYN*, vol. 2014-Janua, no. July, pp. 3089-3096, 2014.
- [45] J. Tilander, M. Patey, and S. Hirdaris, "Springing Analysis of a Passenger Ship in Waves," *Journal of Marine Science and Engineering*, vol. 8, no. 7, pp. 492-492, 2020.

4. SECOND-ORDER DIFFERENCE-FREQUENCY WAVE LOADS ON A FLOATING BODY IN UNIFORM CURRENT

4.1. Background and Literature Review

The effect of steady flow (e.g., current or forward speed) on the wave's diffraction-radiation problem has been widely studied [1-3]. One of the earliest studies to account for the wave-current interaction can be found in [2], where the body was divided into 2D strip sections, and the uniform flow approximation was applied to each section. The advances in computational power in the last two decades have made the boundary element method (BEM) more attractive in solving the wave diffraction-radiation problem. Among many publications, [4], for example, presented a numerical method to solve the boundary integral equations using the Rankine source. To satisfy the free-surface boundary condition automatically, several studies, including [5-8], proposed an oscillating Green function. By utilizing the oscillating (also called free-surface) Green function, the numerical evaluation on the free surface can be avoided, thus reducing the computational burden.

The inclusion of the wave-current interaction effect into the 2D and 3D BEM framework was investigated in [9-13]. In those studies, the wave diffraction-radiation problem was solved up to the first-order in wave slope and first-order in forward speed. There are two popular linear wave-steady flow linearization schemes: the Neumann-Kelvin linearization [14, 15] and the double-body linearization. In the Neumann-Kelvin linearization scheme, the free surface was linearized with respect to the steady flow by considering low forward speed and slender body. Since the body disturbance in the steady potential was omitted, the Neumann-Kelvin linearization method only

used the results from the waves to solve the wave-current interaction problems [2, 10, 13]. Recent developments have been made to account for the higher-current and non-linear free-surface effects. For example, [16, 17] utilized the ship wave Green's function to solve the steady free surface disturbance, and [12, 18-20] solved the weakly non-linear problem, including the exact Froude-Krylov force or the exact free surface evaluation. However, most of the non-linear schemes with instantaneous free-surface and body-surface conditions significantly increased the computational cost (e.g. [21]).

In the case without steady flow, [22-24] obtained the second-order wave force without solving for the second-order wave potential. However, those schemes were not able to calculate local quantities such as hydrodynamic pressures and wave elevations at any point. A more direct method to calculate the second-order force in the frequency domain by direct pressure integration over the body surface was shown in [25-29]. These studies were carried out without considering the steady-uniform flow, which considerably increases the theoretical complexity. As shown by [30] [12], the second-order wave drift load is highly affected by the currents. In this regard, [31] and [32] solved the wave-current interaction problem that is accurate up to the second-order in wave slope and first-order in current speed, including the second-order unsteady velocity potential. Both methods adopted a time-domain simulation and required free-surface discretization. However, to the authors' knowledge, no study has tried to solve the same problem for a floating body in the frequency domain using the direct pressure integration method.

Slowly varying force components of the second-order wave loading can be of high importance in most station keeping problems especially when the natural frequencies of the platform are considerably lower compared to the dominant wave frequencies. This happens in the horizontal motion of slack moored floaters and heave-pitch motions of large-volume deep-draft platforms. In

this paper, we focus on the second-order difference-frequency wave exciting forces including the second-order-potential force. The present study also solves the second-order velocity potential in the presence of small uniform flow. By adopting frequency-domain formulation, we reduce the computational burden when solving the complete quadratic transfer function (QTF). Furthermore, [26] showed that the free-surface-integral effect on the difference frequency wave loading is negligible. Therefore, when combined with the uniform-flow approximation, we can further reduce the computational cost by omitting the free-surface effect, which is to be useful in many practical applications.

4.2. The Second Order Problem

The 2nd order variables include the multiplication between two 1st order oscillating variables. Consider two oscillating 1st order variables of $F_i e^{i\omega_{e_i} t}$ and $G_j e^{i\omega_{e_j} t}$, with the oscillation frequency of ω_{e_i} and ω_{e_j} , the multiplication between the two can be written as:

$$q_{ij} = Re(F_i e^{i\omega_{e_i} t}) \cdot Re(G_j e^{i\omega_{e_j} t}) = \frac{1}{2} Re \left[(F_i e^{i\omega_{e_i} t}) (G_j e^{i\omega_{e_j} t} + G_j^* e^{-i\omega_{e_j} t}) \right] \quad (4.1)$$

where F_i and G_j are time-invariant complex variables, and the (*) superscript indicates its complex conjugates. Note that in the above equation, only the real values are considered to have any physical relevance. We can further decompose eq.(4.1) into:

$$q_{ij}^+ = q_{ji}^+ = \frac{1}{2} Re \left[F_i G_j e^{i(\omega_{e_i} + \omega_{e_j}) t} \right] \quad (4.2)$$

$$q_{ij}^- = q_{ji}^{-*} = \frac{1}{2} Re \left[F_i G_j^* e^{i(\omega_{e_i} - \omega_{e_j}) t} \right]$$

Considering eq.(4.2) above, and considering multiple frequency combinations, the multiplication between two first-order solutions can be written in the symmetric form as follow:

$$Q(\hat{\mathbf{x}}, t) = \frac{1}{2} \text{Re} \sum_{i=1}^N \sum_{j=1}^N \left\{ Q_{ij}^-(\hat{\mathbf{x}}) e^{i(\omega_{ei} - \omega_{ej})t} + Q_{ij}^+(\hat{\mathbf{x}}) e^{i(\omega_{ei} + \omega_{ej})t} \right\} \quad (4.3)$$

$$Q_{ij}^-(\hat{\mathbf{x}}) = \frac{q_{ij}^-(\hat{\mathbf{x}}) + q_{ji}^{-*}(\hat{\mathbf{x}})}{2}$$

$$Q_{ij}^+(\hat{\mathbf{x}}) = \frac{q_{ij}^+(\hat{\mathbf{x}}) + q_{ji}^+(\hat{\mathbf{x}})}{2}$$

Note that the $Q(\hat{\mathbf{x}}, t)$ has the same form as the second-order potential $\Phi^{(2)}(\hat{\mathbf{x}}, t)$ in eq.(1.13). By considering eq.(1.3) – eq.(1.10) and considering the Taylor expansion in eq.(1.19) – eq.(1.21), the 2nd order variables can be found in Table 4.1 below.

Table 4.1. The 2nd order variables

Variables	$O(\epsilon^2)$
$\bar{\mathbf{n}}$	$\bar{\mathbf{n}}^{(2)} = [\mathbf{H}]\mathbf{n} + \boldsymbol{\alpha}^{(2)} \times \mathbf{n}$
$\bar{\mathbf{x}}$	$\bar{\mathbf{x}}^{(2)} = [\mathbf{H}]\mathbf{x} + \boldsymbol{\xi}^{(2)} + \boldsymbol{\alpha}^{(2)} \times \mathbf{x}$
$\bar{\mathbf{x}} \times \bar{\mathbf{n}}$	$(\bar{\mathbf{x}} \times \bar{\mathbf{n}})^{(2)} = [\mathbf{H}](\mathbf{x} \times \mathbf{n}) + \boldsymbol{\xi}^{(2)} \times \mathbf{n} + \boldsymbol{\alpha}^{(2)} \times (\mathbf{x} \times \mathbf{n})$
$P(\bar{\mathbf{x}})_{S_B}$	$P(\bar{\mathbf{x}})_{S_B}^{(2)} = -\rho \left(\frac{\partial \phi_w^{(2)}}{\partial t} - U \frac{\partial \phi_w^{(2)}}{\partial x} + \frac{1}{2} \left \phi_w^{(1)} \right ^2 + g \bar{\mathbf{x}}^{(2)} \cdot \hat{\mathbf{k}} \right)_{S_{B0}}$ $-\rho (\boldsymbol{\xi}^{(1)} + \boldsymbol{\alpha}^{(1)} \times \mathbf{x}) \cdot \nabla \left(\frac{\partial \phi_w^{(1)}}{\partial t} - U \frac{\partial \phi_w^{(1)}}{\partial x} + g \bar{\mathbf{x}}^{(1)} \cdot \hat{\mathbf{k}} \right)_{S_{B0}}$
$\zeta(\bar{\mathbf{x}}, \bar{\mathbf{y}})$	$\zeta(\bar{\mathbf{x}}, \bar{\mathbf{y}})^{(2)} = -\frac{1}{g} \left(\frac{\partial \phi_w^{(2)}}{\partial t} - U \frac{\partial \phi_w^{(2)}}{\partial x} + \frac{1}{2} \left \phi_w^{(1)} \right ^2 \right)_{z=0} + \frac{1}{g^2} \left(\frac{\partial \phi_w^{(1)}}{\partial t} - \right.$ $\left. U \frac{\partial \phi_w^{(1)}}{\partial x} \right) \frac{\partial}{\partial z} \left(\frac{\partial \phi_w^{(1)}}{\partial t} - U \frac{\partial \phi_w^{(1)}}{\partial x} \right)_{z=0}$

where the second term in the $P(\bar{\mathbf{x}})_{S_B}$ and $\zeta(\bar{\mathbf{x}}, \bar{\mathbf{y}})$ come from the Taylor expansion as defined in eq.(1. 21). $[\mathbf{H}]$ is a roll-pitch-yaw second order coordinate transformation matrix which elements are the multiplication between the first order rotational motions as explained in [3] as follow:

$$[\mathbf{H}] = \quad (4.4)$$

$$\begin{bmatrix} -\frac{1}{2}\left(\left(\alpha_y^{(1)}\right)^2 + \left(\alpha_z^{(1)}\right)^2\right) & 0 & 0 \\ \alpha_x^{(1)}\alpha_y^{(1)} & -\frac{1}{2}\left(\left(\alpha_x^{(1)}\right)^2 + \left(\alpha_z^{(1)}\right)^2\right) & 0 \\ \alpha_x^{(1)}\alpha_z^{(1)} & \alpha_y^{(1)}\alpha_z^{(1)} & -\frac{1}{2}\left(\left(\alpha_x^{(1)}\right)^2 + \left(\alpha_y^{(1)}\right)^2\right) \end{bmatrix}$$

Different from the 1st order boundary value problem, the boundary conditions in the 2nd order problem are inhomogeneous, with the right-hand side consisting of multiplication between two known first-order solutions. The second-order boundary value problem is subjected to the following 2nd order boundary conditions as follow:

- Free surface boundary condition:

$$\left[g \frac{\partial}{\partial z} + \left(\frac{\partial}{\partial t} - U \frac{\partial}{\partial x} \right)^2 \right] \phi_w^{(2)} = \text{QF} \quad \text{on } S_F(z = 0) \quad (4.5)$$

where QF is the free surface quadratic forcing function, defined as follow:

$$\text{QF} = \frac{1}{g} \left(\frac{\partial}{\partial t} - U \frac{\partial}{\partial x} \right) \phi_w^{(1)} \frac{\partial}{\partial z} (\text{LF}) - \left(\frac{\partial}{\partial t} - U \frac{\partial}{\partial x} \right) \left| \phi_w^{(1)} \right|^2 \quad (4.6)$$

The first term containing $\frac{\partial}{\partial z} (\text{LF})$ comes from the Taylor expansion of the free surface evaluated at $z = 0$, with LF defined in eq.(2.1). Recalling that the first-order potential $\phi_w^{(1)}$ consist of incident wave potential $\phi_I^{(1)}$, and wave potential due to the presence of the body $\phi_B^{(1)} = \phi_S^{(1)} + \phi_R^{(1)}$, QF can be decomposed into the following components:

$$\text{QF} = \text{QF}_{\text{II}} + \text{QF}_{\text{IB}} + \text{QF}_{\text{BB}} \quad (4.7)$$

where, QF_{II} consist of multiplication between two 1st order incident wave potentials (i.e., $f(\phi_I^{(1)}, \phi_I^{(1)})$), QF_{IB} consist of multiplication between 1st order incident wave potentials and body disturbance potentials (i.e., $f(\phi_I^{(1)}, \phi_B^{(1)})$), and QF_{BB} consist of multiplication between two 1st order body disturbance potentials (i.e., $f(\phi_B^{(1)}, \phi_B^{(1)})$). From these definitions, we decompose the 2nd order free surface boundary condition in eq.(4.5) into the following formulation:

$$\left[g \frac{\partial}{\partial z} + \left(\frac{\partial}{\partial t} - U \frac{\partial}{\partial x} \right)^2 \right] \phi_I^{(2)} = QF_{II} \quad (4.8)$$

$$\left[g \frac{\partial}{\partial z} + \left(\frac{\partial}{\partial t} - U \frac{\partial}{\partial x} \right)^2 \right] \phi_S^{(2)} = QF_{IB} + QF_{BB} \quad (4.9)$$

$$\left[g \frac{\partial}{\partial z} + \left(\frac{\partial}{\partial t} - U \frac{\partial}{\partial x} \right)^2 \right] \phi_{rk}^{(2)} = 0 \quad (4.10)$$

- Bottom boundary condition:

$$\frac{\partial \phi_w^{(2)}}{\partial z} = 0 \quad \text{on } S_h(z = -h) \quad (4.11)$$

- Body boundary condition of the scattering potential:

$$\frac{\partial \phi_S^{(2)}}{\partial \mathbf{n}} = -\frac{\partial \phi_I^{(2)}}{\partial \mathbf{n}} + QB \quad \text{on } S_B = S_{B0} \quad (4.12)$$

where QB is the body boundary quadratic forcing function, defined as follow:

$$QB = \mathbf{n} \cdot \frac{\partial [H]}{\partial t} \mathbf{x} - [H] \mathbf{n} \cdot U \hat{\mathbf{i}} + (\boldsymbol{\alpha}^{(1)} \times \mathbf{n}) \cdot \left(\frac{\partial (\boldsymbol{\xi}^{(1)} + \boldsymbol{\alpha}^{(1)} \times \mathbf{x})}{\partial t} - \nabla \phi_w^{(1)} \right) - \mathbf{n} \cdot \left((\boldsymbol{\xi}^{(1)} + \boldsymbol{\alpha}^{(1)} \times \mathbf{x}) \cdot \nabla \right) \nabla \phi_w^{(1)} \quad (4.13)$$

The last term containing second-order spatial derivative comes from the Taylor expansion of the fluid velocity evaluated at the body at rest, i.e., $\nabla\Phi|_{S_B} \cong \nabla\Phi|_{S_B^0} + \mathbf{x}|_{S_B} \cdot \nabla(\nabla\Phi)|_{S_B^0} + \dots$. The effect of the second term $[\mathbf{H}]\mathbf{n} \cdot \mathbf{U} \hat{\mathbf{i}}$ are particularly interesting since it comes from the steady flow $\mathbf{U} \hat{\mathbf{i}}$, which is not included in the typical 2nd order wave diffraction-radiation boundary value problem.

- Body boundary condition of the radiation potential:

$$\eta_k^{(2)} \frac{\partial \phi_{rk}^{(2)}}{\partial \mathbf{n}} = \frac{\partial \eta_k^{(2)}}{\partial t} n'_k + \mathbf{U} \eta_k^{(2)} m_k, \quad k=1,2,\dots,6 \quad \text{on } S_B = S_{B0} \quad (4.14)$$

Just like on the 1st order boundary condition, the m terms come from the interaction between the zeroth-order potential with 2nd order normal direction (see Table 4.1). For wave-uniform-flow interaction model, the m terms are reduced to:

$$m_j = (0, 0, 0, 0, n_3, -n_2) \quad (4.15)$$

For the case without uniform flow, the body boundary condition of the radiation potential is reduced to:

$$\eta_k^{(2)} \frac{\partial \phi_{rk}^{(2)}}{\partial \mathbf{n}} = \frac{\partial \eta_k^{(2)}}{\partial t} n'_k, \quad k=1,2,\dots,6 \quad \text{on } S_B = S_{B0} \quad (4.16)$$

- Far-field boundary condition:

$$\lim_{|\mathbf{x}| \rightarrow \infty} \sqrt{|\mathbf{x}|} \left(\frac{\partial}{\partial t} - ik_e \right) \phi_w^{(2)} \quad \text{on } S_{|\mathbf{x}| \rightarrow \infty} \quad (4.17)$$

The uniform flow affect the 2nd order boundary problem through all the terms containing the uniform flow speed \mathbf{U} , and through the 1st order motions $\xi^{(1)}$ and $\alpha^{(1)}$. Just like on the first order

free surface condition, we consider $\omega_e \gg U(\partial/\partial x)$ to be valid throughout this study. Due to this consideration, the second-order free surface boundary condition is reduced back to the same form as the case without uniform flow such as below:

$$\left[g \frac{\partial}{\partial z} + \left(\frac{\partial}{\partial t} - U \frac{\partial}{\partial x} \right)^2 \right] \phi_w^{(2)} \cong \left[g \frac{\partial}{\partial z} + \frac{\partial^2}{\partial t^2} \right] \phi_w^{(2)} = QF^0 \quad (4.18)$$

$$QF^0 = \frac{1}{g} \frac{\partial \phi_w^{(1)}}{\partial t} \frac{\partial}{\partial z} (LF^0) - \frac{\partial}{\partial t} \left| \phi_w^{(1)} \right|^2 \quad (4.19)$$

All of the above 2nd order boundary conditions can be used to solve both the sum frequency potentials $\phi_{ij}^+(\hat{\mathbf{x}})$, and the difference frequency potentials $\phi_{ij}^-(\hat{\mathbf{x}})$ without losing any generality. However, in this study, we only consider the difference frequency potentials and the associated loading due to the reasons stated in the Introduction section.

Considering the symmetric form in eq.(4.4), the difference frequency component of the quadratic forcing functions and other relevant quadratic variables can be written as follow:

$$[\mathbf{H}]^- \quad (4.20)$$

$$= \frac{1}{2} \begin{bmatrix} - \left(\alpha_{y_i}^{(1)} \alpha_{y_j}^{*(1)} + \alpha_{z_i}^{(1)} \alpha_{z_j}^{*(1)} \right) & 0 & 0 \\ \alpha_{x_i}^{(1)} \alpha_{y_j}^{*(1)} + \alpha_{x_j}^{*(1)} \alpha_{y_i}^{(1)} & - \left(\alpha_{x_i}^{(1)} \alpha_{x_j}^{*(1)} + \alpha_{z_i}^{(1)} \alpha_{z_j}^{*(1)} \right) & 0 \\ \alpha_{x_i}^{(1)} \alpha_{z_j}^{*(1)} + \alpha_{x_j}^{*(1)} \alpha_{z_i}^{(1)} & \alpha_{y_i}^{(1)} \alpha_{z_j}^{*(1)} + \alpha_{y_j}^{*(1)} \alpha_{z_i}^{(1)} & - \left(\alpha_{x_i}^{(1)} \alpha_{x_j}^{*(1)} + \alpha_{y_i}^{(1)} \alpha_{y_j}^{*(1)} \right) \end{bmatrix}$$

$$QF_{ij}^- = \frac{1}{4g} \left(i\omega_{e_i} - U \frac{\partial}{\partial x} \right) \phi_{w_i}^{(1)} \frac{\partial}{\partial z} \left(g \frac{\partial}{\partial z} + \left\{ -i\omega_{e_j} - U \frac{\partial}{\partial x} \right\}^2 \right) \phi_{w_j}^{*(1)} \quad (4.21)$$

$$+ \frac{1}{4g} \left(-i\omega_{e_j} - U \frac{\partial}{\partial x} \right) \phi_{w_j}^{*(1)} \frac{\partial}{\partial z} \left(g \frac{\partial}{\partial z} + \left\{ i\omega_{e_i} - U \frac{\partial}{\partial x} \right\}^2 \right) \phi_{w_i}^{(1)}$$

$$- \frac{1}{2} \left(i \left(\omega_{e_i} - \omega_{e_j} \right) - U \frac{\partial}{\partial x} \right) \nabla \phi_{w_i}^{(1)} \cdot \nabla \phi_{w_j}^{*(1)}$$

$$QF_{ij}^{0-} = \frac{1}{4g} i\omega_{e_i} \phi_{w_i}^{(1)} \frac{\partial}{\partial z} \left(g \frac{\partial}{\partial z} - i\omega_{e_j}^2 \right) \phi_{w_j}^{*(1)} \quad (4.22)$$

$$\begin{aligned}
& -\frac{1}{4g} i\omega_{e_j} \Phi_{w_j}^{*(1)} \frac{\partial}{\partial z} \left(g \frac{\partial}{\partial z} - i\omega_{e_i}^2 \right) \Phi_{w_i}^{(1)} \\
& -\frac{i(\omega_{e_i} - \omega_{e_j})}{2} \nabla \Phi_{w_i}^{(1)} \cdot \nabla \Phi_{w_j}^{*(1)} \\
QB_{ij}^- = & \frac{i(\omega_{e_i} - \omega_{e_j})}{2} [\mathbf{H}]^- \mathbf{x} \cdot \mathbf{n} - \frac{1}{2} [\mathbf{H}]^- \mathbf{n} \cdot \mathbf{U} \hat{\mathbf{i}} \\
& + \frac{1}{4} (\boldsymbol{\alpha}_i^{(1)} \times \mathbf{n}) \cdot \left(-i\omega_{e_j} (\boldsymbol{\xi}_j^{*(1)} + \boldsymbol{\alpha}_j^{*(1)} \times \mathbf{x}) - \nabla \Phi_{w_j}^{*(1)} \right) \\
& + \frac{1}{4} (\boldsymbol{\alpha}_j^{*(1)} \times \mathbf{n}) \cdot \left(i\omega_{e_i} (\boldsymbol{\xi}_i^{(1)} + \boldsymbol{\alpha}_i^{(1)} \times \mathbf{x}) - \nabla \Phi_{w_i}^{(1)} \right) \\
& - \frac{1}{4} \mathbf{n} \cdot \left((\boldsymbol{\xi}_i^{(1)} + \boldsymbol{\alpha}_i^{(1)} \times \mathbf{x}) \cdot \nabla \right) \nabla \Phi_{w_j}^{*(1)} - \frac{1}{4} \mathbf{n} \cdot \left((\boldsymbol{\xi}_j^{*(1)} + \boldsymbol{\alpha}_j^{*(1)} \times \mathbf{x}) \cdot \nabla \right) \nabla \Phi_{w_i}^{(1)}
\end{aligned} \tag{4.23}$$

By substituting the eq.(2.12) into eq.(4.18)-(4.19) the 2nd order difference-frequency incident potential $\Phi_{I_{ij}}^-$ for uni-directional seas can be written as follow [26]:

$$\Phi_{I_{ij}}^- = QF_{II}^- \frac{\cosh\{\kappa_{e_{ij}}^-(z+h)\}}{[-\nu_{e_{ij}}^- + \kappa_{e_{ij}}^- \tanh(\kappa_{e_{ij}}^- h)] \cosh\{\kappa_{e_{ij}}^- h\}} \tag{4.24}$$

where,

$$QF_{II}^- = \left\{ \frac{igA_i A_j^*}{2} \right\} \left\{ \frac{(k_{e_j}^2 - \nu_{e_j}^2)}{2\omega_{e_j}} - \frac{(k_{e_i}^2 - \nu_{e_i}^2)}{2\omega_{e_i}} - \frac{(\omega_{e_i} - \omega_{e_j})}{\omega_{e_i} \omega_{e_j}} (\mathbf{k}_i \cdot \mathbf{k}_j + \nu_{e_i} \nu_{e_j}) \right\} e^{-i(\mathbf{k}_i - \mathbf{k}_j) \cdot \mathbf{x}} \tag{4.25}$$

$$\nu_{e_i} = \omega_{e_i}^2 / g$$

$$\nu_{e_{ij}}^- = (\omega_{e_i} - \omega_{e_j})^2 / g$$

$$\kappa_{e_{ij}}^- = |\mathbf{k}_i - \mathbf{k}_j| = \sqrt{k_i^2 + k_j^2}$$

4.3. The Second-order Wave Loading

After solving the 1st order potentials, forces, and motions, the 2nd order forces are obtained by collecting the $O(\epsilon^2)$ terms in eq.(1.22)-(1.23) as follow:

$$\mathbf{F}^{(2)} = \mathbf{F}'_{1-3}{}^{(2)} \quad (4.26)$$

$$\begin{aligned} &= - \iint_{S_{B0}} P^{(0)}[\mathbf{H}]\mathbf{n} \, dS \\ &\quad - \iint_{S_{B0}} P^{(0)}(\boldsymbol{\alpha}^{(2)} \times \mathbf{n}) \, dS - \iint_{S_B} P^{(1)}(\boldsymbol{\alpha}^{(1)} \times \mathbf{n}) \, dS \\ &\quad - \iint_{S_B} P^{(2)}\mathbf{n} \, dS \end{aligned}$$

$$\mathbf{M}^{(2)} = \mathbf{F}'_{4-6}{}^{(2)} \quad (4.27)$$

$$\begin{aligned} &= - \iint_{S_B} P^{(0)}(\boldsymbol{\xi}^{(2)} \times \mathbf{n}) \, dS - \iint_{S_B} P^{(0)}(\boldsymbol{\alpha}^{(2)} \times (\mathbf{x} \times \mathbf{n})) \, dS \\ &\quad - \iint_{S_B} P^{(0)}[\mathbf{H}](\mathbf{x} \times \mathbf{n}) \, dS \\ &\quad - \iint_{S_B} P^{(1)}(\boldsymbol{\xi}^{(1)} \times \mathbf{n}) \, dS - \iint_{S_B} P^{(1)}(\boldsymbol{\alpha}^{(1)} \times (\mathbf{x} \times \mathbf{n})) \, dS \\ &\quad - \iint_{S_B} P^{(2)}(\mathbf{x} \times \mathbf{n}) \, dS \\ &\quad - \int_{wl} \int_0^{z_r^{(1)}} \rho g z (\mathbf{x} \times \mathbf{n}) \, dz \, dl \end{aligned}$$

Similar to the eq.(1.13) the total time-varying forces and moments are defined as $\mathbf{F}'_T{}^{(2)}(t) = \text{Re} \sum_{i=1}^N \sum_{j=1}^N \{ \mathbf{F}'_{ij}{}^- e^{i(\omega_{ei} - \omega_{ej})t} + \mathbf{F}'_{ij}{}^+ e^{i(\omega_{ei} + \omega_{ej})t} \}$, with \mathbf{F}' defined in eq.(1.24) and $\mathbf{F}'_{ij}{}^\pm$ referred to as the force quadratic transfer function (QTF). Collecting the forcing terms with similar characteristics, the second-order forces can be written in the following form:

$$\mathbf{F}'^{(2)} = \mathbf{F}'_q{}^{(2)} + \mathbf{F}'_p{}^{(2)} + \mathbf{F}'_h{}^{(2)} + \left[\mathbf{A}^{(2)} - \frac{i}{\omega_e} \mathbf{B}^{(2)} \right] \ddot{\boldsymbol{\eta}}^{(2)} \quad (4.28)$$

where $\mathbf{F}'_q^{(2)}$ is the quadratic wave force and moment from multiplication between two first-order terms, $\mathbf{F}'_p^{(2)}$ is the second-order diffraction force from $\phi_1^{(2)} + \phi_s^{(2)}$ terms, $([\mathbf{A}^{(2)}] - i[\mathbf{B}^{(2)}]/\omega_e)$ are the added mass and hydrodynamic damping from $\phi_r^{(2)}$ terms, $\ddot{\boldsymbol{\eta}}^{(2)}$ is the second-order body's acceleration, and $\mathbf{F}'_h^{(2)}$ is the hydrostatic forces that only depends on second-order motions $\boldsymbol{\eta}^{(2)}$ and independent from the wave potentials. $\mathbf{F}'_q^{(2)}$ and $\mathbf{F}'_p^{(2)}$ is of particular interest, since it acts as the second-order wave exciting force $\mathbf{F}'_{ext}^{(2)}$ on the right-hand side of the equation of motion. With only considering the difference frequency force, the quadratic force and second-order diffraction force are defined as follow:

$$\begin{aligned}
\mathbf{F}'_{qij} = & \frac{1}{4} \rho g \int_{wl} \left[\zeta_i^{(1)} - \left(\xi_{z_i}^{(1)} + \alpha_{x_i}^{(1)} y - \alpha_{y_i}^{(1)} x \right) \right] \left[\zeta_j^{*(1)} - \left(\xi_{z_j}^{*(1)} + \alpha_{x_j}^{*(1)} y - \right. \right. \\
& \left. \left. \alpha_{y_j}^{*(1)} x \right) \right] \frac{\mathbf{n}}{\sqrt{1-n_z}} dl \\
& - \frac{1}{4} \rho \iint_{S_B} \nabla \phi_{w_i}^{(1)} \cdot \nabla \phi_{w_j}^{*(1)} \mathbf{n} dS \\
& - \frac{1}{4} \rho \iint_{S_B} \left(\xi_i^{(1)} + \boldsymbol{\alpha}_i^{(1)} \times \mathbf{x} \right) \cdot \nabla \left(\frac{\partial \phi_{w_j}^{*(1)}}{\partial t} - U \frac{\partial \phi_{w_j}^{*(1)}}{\partial x} \right) \mathbf{n} dS \\
& - \frac{1}{4} \rho \iint_{S_B} \left(\xi_j^{*(1)} + \boldsymbol{\alpha}_j^{*(1)} \times \mathbf{x} \right) \cdot \nabla \left(\frac{\partial \phi_{w_i}^{(1)}}{\partial t} - U \frac{\partial \phi_{w_i}^{(1)}}{\partial x} \right) \mathbf{n} dS \\
& + \frac{1}{4} \rho \boldsymbol{\alpha}_i^{(1)} \times \iint_{S_B} \left(\frac{\partial \phi_{w_j}^{*(1)}}{\partial t} - U \frac{\partial \phi_{w_j}^{*(1)}}{\partial x} \right) \mathbf{n} dS \\
& + \frac{1}{4} \rho \boldsymbol{\alpha}_j^{*(1)} \times \iint_{S_B} \left(\frac{\partial \phi_{w_i}^{(1)}}{\partial t} - U \frac{\partial \phi_{w_i}^{(1)}}{\partial x} \right) \mathbf{n} dS \\
& - \frac{1}{4} \rho g A_{wp} \left(\alpha_{x_i}^{(1)} \alpha_{z_j}^{*(1)} x_f + \alpha_{y_i}^{(1)} \alpha_{z_j}^{*(1)} y_f + \frac{1}{2} \left(\alpha_{x_i}^{(1)} \alpha_{x_j}^{*(1)} + \alpha_{y_i}^{(1)} \alpha_{y_j}^{*(1)} \right) Z_0 \right) \hat{\mathbf{k}} \\
& - \frac{1}{4} \rho g A_{wp} \left(\alpha_{z_i}^{(1)} \alpha_{x_j}^{*(1)} x_f + \alpha_{z_i}^{(1)} \alpha_{y_j}^{*(1)} y_f + \frac{1}{2} \left(\alpha_{x_i}^{(1)} \alpha_{x_j}^{*(1)} + \alpha_{y_i}^{(1)} \alpha_{y_j}^{*(1)} \right) Z_0 \right) \hat{\mathbf{k}}
\end{aligned} \tag{4.29}$$

$$\begin{aligned}
\mathbf{M}_{qij}^- &= \frac{1}{4} \rho g \int_{wl} \left[\zeta_i^{(1)} - \left(\xi_{z_i}^{(1)} + \alpha_{x_i}^{(1)} y - \alpha_{y_i}^{(1)} x \right) \right] \left[\zeta_j^{*(1)} - \left(\xi_{z_j}^{*(1)} + \alpha_{x_j}^{*(1)} y - \right. \right. \\
&\quad \left. \left. \alpha_{y_j}^{*(1)} x \right) \right] \frac{(\mathbf{x} \times \mathbf{n})}{\sqrt{1-n_z}} dl \\
&\quad - \frac{1}{4} \rho \iint_{S_B} \nabla \phi_{w_i}^{(1)} \cdot \nabla \phi_{w_j}^{*(1)} (\mathbf{x} \times \mathbf{n}) dS \\
&\quad - \frac{1}{4} \rho \iint_{S_B} \left(\xi_i^{(1)} + \alpha_i^{(1)} \times \mathbf{x} \right) \cdot \nabla \left(\frac{\partial \phi_{w_j}^{*(1)}}{\partial t} - U \frac{\partial \phi_{w_j}^{*(1)}}{\partial x} \right) (\mathbf{x} \times \mathbf{n}) dS \\
&\quad - \frac{1}{4} \rho \iint_{S_B} \left(\xi_j^{*(1)} + \alpha_j^{*(1)} \times \mathbf{x} \right) \cdot \nabla \left(\frac{\partial \phi_{w_i}^{(1)}}{\partial t} - U \frac{\partial \phi_{w_i}^{(1)}}{\partial x} \right) (\mathbf{x} \times \mathbf{n}) dS \\
&\quad + \frac{1}{4} \rho \xi_i^{(1)} \times \iint_{S_B} \left(\frac{\partial \phi_{w_j}^{*(1)}}{\partial t} - U \frac{\partial \phi_{w_j}^{*(1)}}{\partial x} \right) \mathbf{n} dS + \frac{1}{4} \rho \xi_j^{*(1)} \times \iint_{S_B} \left(\frac{\partial \phi_{w_i}^{(1)}}{\partial t} - \right. \\
&\quad \left. U \frac{\partial \phi_{w_i}^{(1)}}{\partial x} \right) \mathbf{n} dS \\
&\quad + \frac{1}{4} \rho \alpha_i^{(1)} \times \iint_{S_B} \left(\frac{\partial \phi_{w_j}^{*(1)}}{\partial t} - U \frac{\partial \phi_{w_j}^{*(1)}}{\partial x} \right) (\mathbf{x} \times \mathbf{n}) dS \\
&\quad + \frac{1}{4} \rho \alpha_j^{*(1)} \times \iint_{S_B} \left(\frac{\partial \phi_{w_i}^{(1)}}{\partial t} - U \frac{\partial \phi_{w_i}^{(1)}}{\partial x} \right) (\mathbf{x} \times \mathbf{n}) dS \\
&\quad + \frac{1}{4} \rho g V \left[-\xi_{x_i}^{(1)} \alpha_{z_j}^{*(1)} - \xi_{x_j}^{*(1)} \alpha_{z_i}^{(1)} + \left(\alpha_{x_i}^{(1)} \alpha_{y_j}^{*(1)} + \alpha_{x_j}^{*(1)} \alpha_{y_i}^{(1)} \right) x_b - \left(\alpha_{y_i}^{(1)} \alpha_{z_j}^{*(1)} + \right. \right. \\
&\quad \left. \left. \alpha_{y_j}^{*(1)} \alpha_{z_i}^{(1)} \right) z_b - \left(\alpha_{x_i}^{(1)} \alpha_{x_j}^{*(1)} + \alpha_{z_i}^{(1)} \alpha_{z_j}^{*(1)} \right) y_b \right] \hat{\mathbf{i}} \\
&\quad + \frac{1}{4} \rho g V \left[-\xi_{y_i}^{(1)} \alpha_{z_j}^{*(1)} - \xi_{y_j}^{*(1)} \alpha_{z_i}^{(1)} + \left(\alpha_{x_i}^{(1)} \alpha_{z_j}^{*(1)} + \alpha_{x_j}^{*(1)} \alpha_{z_i}^{(1)} \right) z_b + \left(\alpha_{y_i}^{(1)} \alpha_{y_j}^{*(1)} + \right. \right. \\
&\quad \left. \left. \alpha_{z_i}^{(1)} \alpha_{z_j}^{*(1)} \right) x_b \right] \hat{\mathbf{j}} \\
&\quad + \frac{1}{4} \rho g V \left[\xi_{x_i}^{(1)} \alpha_{x_j}^{*(1)} + \xi_{x_j}^{*(1)} \alpha_{x_i}^{(1)} + \xi_{y_i}^{(1)} \alpha_{y_j}^{*(1)} + \xi_{y_j}^{*(1)} \alpha_{y_i}^{(1)} + \left(\alpha_{y_i}^{(1)} \alpha_{z_j}^{*(1)} + \right. \right. \\
&\quad \left. \left. \alpha_{y_j}^{*(1)} \alpha_{z_i}^{(1)} \right) x_b - \left(\alpha_{x_i}^{(1)} \alpha_{z_j}^{*(1)} + \alpha_{x_j}^{*(1)} \alpha_{z_i}^{(1)} \right) y_b \right] \hat{\mathbf{k}}
\end{aligned} \tag{4.30}$$

$$\begin{aligned}
& + \frac{1}{4} \rho g \left[- \left(\alpha_{x_i}^{(1)} \alpha_{z_j}^{*(1)} + \alpha_{x_j}^{*(1)} \alpha_{z_i}^{(1)} \right) L_{12} - \left(\alpha_{y_i}^{(1)} \alpha_{z_j}^{*(1)} + \alpha_{y_j}^{*(1)} \alpha_{z_i}^{(1)} \right) L_{22} - \right. \\
& \quad \left. \left(\alpha_{x_i}^{(1)} \alpha_{x_j}^{*(1)} + \alpha_{y_i}^{(1)} \alpha_{y_j}^{*(1)} \right) Z_0 A_{wp} y_f \right] \hat{\mathbf{i}} \\
& + \frac{1}{4} \rho g \left[\left(\alpha_{x_i}^{(1)} \alpha_{z_j}^{*(1)} + \alpha_{x_j}^{*(1)} \alpha_{z_i}^{(1)} \right) L_{11} + \left(\alpha_{y_i}^{(1)} \alpha_{z_j}^{*(1)} + \alpha_{y_j}^{*(1)} \alpha_{z_i}^{(1)} \right) L_{12} + \right. \\
& \quad \left. \left(\alpha_{x_i}^{(1)} \alpha_{x_j}^{*(1)} + \alpha_{y_i}^{(1)} \alpha_{y_j}^{*(1)} \right) Z_0 A_{wp} x_f \right] \hat{\mathbf{j}}
\end{aligned}$$

$$\mathbf{F}_{pI_{ij}}^- = -\rho \iint_{S_{B0}} \left(\frac{\partial \phi_{I_{ij}}^-}{\partial t} - U \frac{\partial \phi_{I_{ij}}^-}{\partial x} \right) \mathbf{n} \, dS \quad (4.31)$$

$$\mathbf{M}_{pI_{ij}}^- = -\rho \iint_{S_{B0}} \left(\frac{\partial \phi_{I_{ij}}^-}{\partial t} - U \frac{\partial \phi_{I_{ij}}^-}{\partial x} \right) (\mathbf{x} \times \mathbf{n}) \, dS \quad (4.32)$$

$$\mathbf{F}_{pS_{ij}}^- = -\rho \iint_{S_{B0}} \left(\frac{\partial \phi_{S_{ij}}^-}{\partial t} - U \frac{\partial \phi_{S_{ij}}^-}{\partial x} \right) \mathbf{n} \, dS \quad (4.33)$$

$$\mathbf{M}_{pS_{ij}}^- = -\rho \iint_{S_{B0}} \left(\frac{\partial \phi_{S_{ij}}^-}{\partial t} - U \frac{\partial \phi_{S_{ij}}^-}{\partial x} \right) (\mathbf{x} \times \mathbf{n}) \, dS \quad (4.34)$$

where $A_{wp} = \iint_{S_{B0}} n_z \, dS$ is the waterplane area, x_f and y_f are the coordinate center of floatation, L_{mn} is the second moment over the waterplane area (e.g., $L_{12} = \iint_{S_{B0}} x y n_z \, dS$). When $\omega_{0_i} = \omega_{0_j}$ (i.e., the main diagonal of the QTF), the total 2nd order wave exciting force only depends on the quadratic force, since the 2nd order diffraction force is zero-valued. It is clear that the quadratic force only depends on the 1st order variable and doesn't require the solving of the rather complicated 2nd order boundary value problem (eq.(4.5)-(4.19)).

4.4. Implementation

Similar to the 1st order problem, the difference frequency scattering potentials $\phi_{S_{ij}}^-$ or each encounter frequency combinations ω_{e_i} and ω_{e_j} , can be obtained by solving the following boundary integral equations:

$$\begin{aligned}
2\pi\phi_{S_{ij}}^-(\mathbf{x}) + \iint_{S_B} \phi_{S_{ij}}^-(\mathbf{x}') \frac{\partial G^0(\kappa_{eij}^-, \mathbf{x}, \mathbf{x}')}{\partial \mathbf{n}} dS = & \quad (4.35) \\
& \iint_{S_B} \left(-\frac{\partial \phi_{I_{ij}}^-(\mathbf{x}')}{\partial \mathbf{n}} + QB_{ij}^-(\mathbf{x}') \right) G^0(\kappa_{eij}^-, \mathbf{x}, \mathbf{x}') dS \\
& + \frac{1}{g} \iint_{S_F} \left(QF_{IB_{ij}}^{0-}(\mathbf{x}') + QF_{BB_{ij}}^{0-}(\mathbf{x}') \right) G^0(\kappa_{eij}^-, \mathbf{x}, \mathbf{x}') dS
\end{aligned}$$

The right-hand side of the boundary integral equation contains an infinite-domain free-surface integral part that does not exist on the 1st order problem. This additional integral significantly increases the numerical complexity since it needs to satisfy the infinite domain boundary condition and require free surface discretization. Kim [26] and Ma et.al., [33] show that for uni-directional seas, the free surface contribution to the total difference frequency forces is negligible for most engineering cases. We also validate this claim by comparing the present model (without free surface contribution) with the industry-standard software WAMIT (with free surface contribution) [34] in the Validation section. Therefore, to maintain the advantages of the uniform flow approximation model, i.e., the use of zero speed free surface green function without free surface discretization, we neglect the free surface contribution in this study. We call this approach the weak second-order potential, which obtained the difference frequency scattering potentials by solving the following boundary integral equation:

$$\begin{aligned}
2\pi\phi_{S_{ij}}^-(\mathbf{x}) + \iint_{S_B} \phi_{S_{ij}}^-(\mathbf{x}') \frac{\partial G^0(\kappa_{eij}^-, \mathbf{x}, \mathbf{x}')}{\partial \mathbf{n}} dS \cong & \quad (4.36) \\
& \iint_{S_B} \left(-\frac{\partial \phi_{I_{ij}}^-(\mathbf{x}')}{\partial \mathbf{n}} + QB_{ij}^-(\mathbf{x}') \right) G^0(\kappa_{eij}^-, \mathbf{x}, \mathbf{x}') dS
\end{aligned}$$

Considering that the right-hand side of eq.(4. 36) above is given by the body boundary condition in (4.23)-(4.24), $\phi_{S_{ij}}^-$ can be solved by solving the discretized form of the second-kind Fredholm integral equation.

In the irregular wave's analysis, the structure is subjected to JONSWAP wave's spectra defined as follow [35]:

$$S_{\eta\eta}(\omega_i) = \alpha\beta H_s^2 \omega_p^4 \omega_i^{-5} \exp\left(-1.25 \frac{\omega_i^4}{\omega_p^4}\right) \quad (4.37)$$

where,

$$a = \gamma \exp\left(-\left(\frac{\omega_i}{\omega_p} - 1\right)^2 / 2\sigma^2\right)$$

$$\beta = \frac{0.597+0.3125\gamma}{1.27+1.47\gamma+0.168\gamma^2} \quad (4.38)$$

$$\sigma = \begin{cases} 0.07, & \omega_i < \omega_p \\ 0.09, & \omega_i \geq \omega_p \end{cases}$$

where H_s , ω_p , and γ is the significant wave's height, peak frequency, and wave's enhancement factor, respectively. Given the irregular wave's energy spectral density $S_{\eta\eta}(\omega_i)$ and the complex quadratic transfer function of the difference frequency force $\mathbf{QTF}_F^-(\omega_i, \omega_j)$, the energy spectral density of the slowly varying force \mathbf{F}_{ij}^- can be readily calculated by using the following equation:

$$\mathbf{S}_{FF}^{(2)-}(\delta\omega) = 8 \int_0^\infty S_{\eta\eta}(\omega + \delta\omega) S_{\eta\eta}(\omega) |\mathbf{QTF}_F^-(\omega + \delta\omega, \omega)|^2 d\omega \quad (4.39)$$

In the discrete form with fixed $\Delta\omega$ the eq.(4. 39) can be rewritten into eq.(4.40), while its corresponding time series can be found in eq.(4.41)-(4.42).

$$\mathbf{S}_{FF}^{(2)-}(\delta\omega_i) = 8 \sum_{j=1}^{N_w} \{S_{\eta\eta}(\omega_j + (i-1)\Delta\omega) S_{\eta\eta}(\omega_j) |\mathbf{QTF}_F^-(\omega_j + (i-1)\Delta\omega, \omega_j)|^2 \Delta\omega\} \quad (4.40)$$

$$|A_i| = \sqrt{2S_{AA}(\delta\omega_i)\Delta\omega} \quad (4.41)$$

$$A(t) = \sum_{i=1}^{N_w} |A_i| \cos(\delta\omega_i t + \theta_i) \quad (4.42)$$

where $|A_i|$ is the frequency dependent real valued amplitude, N_w is the total number of simulated frequency, $\delta\omega_i$ is the frequency difference, and θ_i is the random phase angle between 0 and 2π . The slowly varying force time series can also be directly calculated from the wave's amplitude time series and the force's QTFs, by employing a double inverse Fourier transform as follow:

$$\begin{aligned} \mathbf{F}'_{ext}(2)^-(t) = \sum_{j=1}^{N_w} \sum_{k=1}^{N_w} A_j A_k [& Re\{\mathbf{QTF}_F^-(\omega_j, \omega_k)\} \cos\{(\omega_k - \omega_j) + (\theta_k - \theta_j)\} + \\ & Im\{\mathbf{QTF}_F^-(\omega_j, \omega_k)\} \sin\{(\omega_k - \omega_j) + (\theta_k - \theta_j)\}] \end{aligned} \quad (4.43)$$

where A_j and A_k are the wave's amplitude as defined in eq. (4.41)-(4.42). In this study, the slowly varying force time series is calculated by employing the eq. (4.44), while the wave's elevation time series is calculated by employing the eq. (4.42). The energy spectra can be described in terms of the encounter frequency ω_e or the zero uniform flow frequency ω_0 . The relation between the two can be achieved by the conservation of energy as described in eq.(4.45) below:

$$S_{AA}(\omega_{e_i}) = S_{AA}(\omega_{0_i}) \frac{d\omega_0}{d\omega_e} = S_{AA}(\omega_{0_i}) \left[\frac{g}{g + 2\omega_{0_i} U \cos(\beta_{cw})} \right] \quad (\text{in deepwater}) \quad (4.45)$$

4.5. Validation

The proposed interaction theory for wave with uniform flow is validated through comparisons with experiments and numerical simulation data available from the literature. Also, the approximation omitting the free surface integral in eq.(4.36) is compared against the industry-standard software WAMIT. In this study, a slender ship with forward speed (or a weather-vanning

vessel in head seas) (i.e. $\beta_{cw} = 0^0$ and $\beta = 180^0$) is considered so that the uniform flow assumptions are satisfied. Deepwater condition ($h \gg 0.5\lambda$) is chosen to simplify the problem.

Two types of slender hulls with analytical expression are used for the case study, with one having a slightly larger breadth to length ratio than the other. These hull shapes are also known as Wigley hull, and can be described as $\eta = (1 - \zeta^2)(1 - \xi^2)(1 + a_2\xi^2 + a_4\xi^4) + a\zeta^2(1 - \zeta^8)(1 - \xi^2)^4$. Where $\xi = \frac{2x}{L}$, $\eta = \frac{2y}{B}$, $\zeta = \frac{z}{D}$. L, B, and D are the ship's length, breadth and draft, respectively. The particulars of the two Wigley hulls are given in Table 4.2, and its hull shapes are shown in Fig. 4.1.

Table 4.2. Particulars of the Wigley hulls

Name	a	a_2	a_4	L	B	D
Wigley I (Slender)	1.0	0.2	1.0	2	0.3	0.125
Wigley II (Blunt)	1	0.6	1	2.5	0.5	0.175

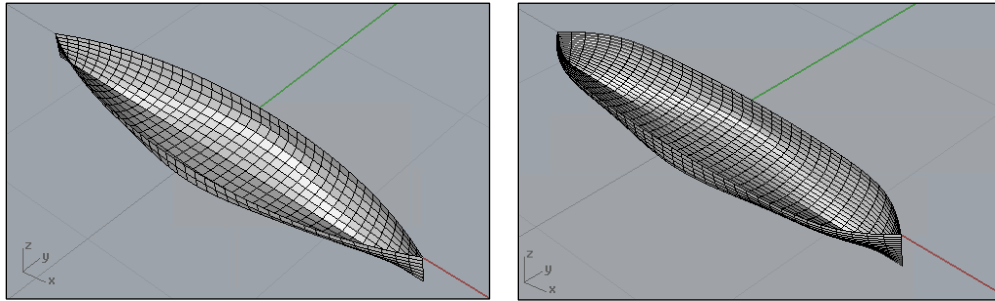


Fig. 4.1. Hull shape of the Wigley I (left) and Wigley II (right)

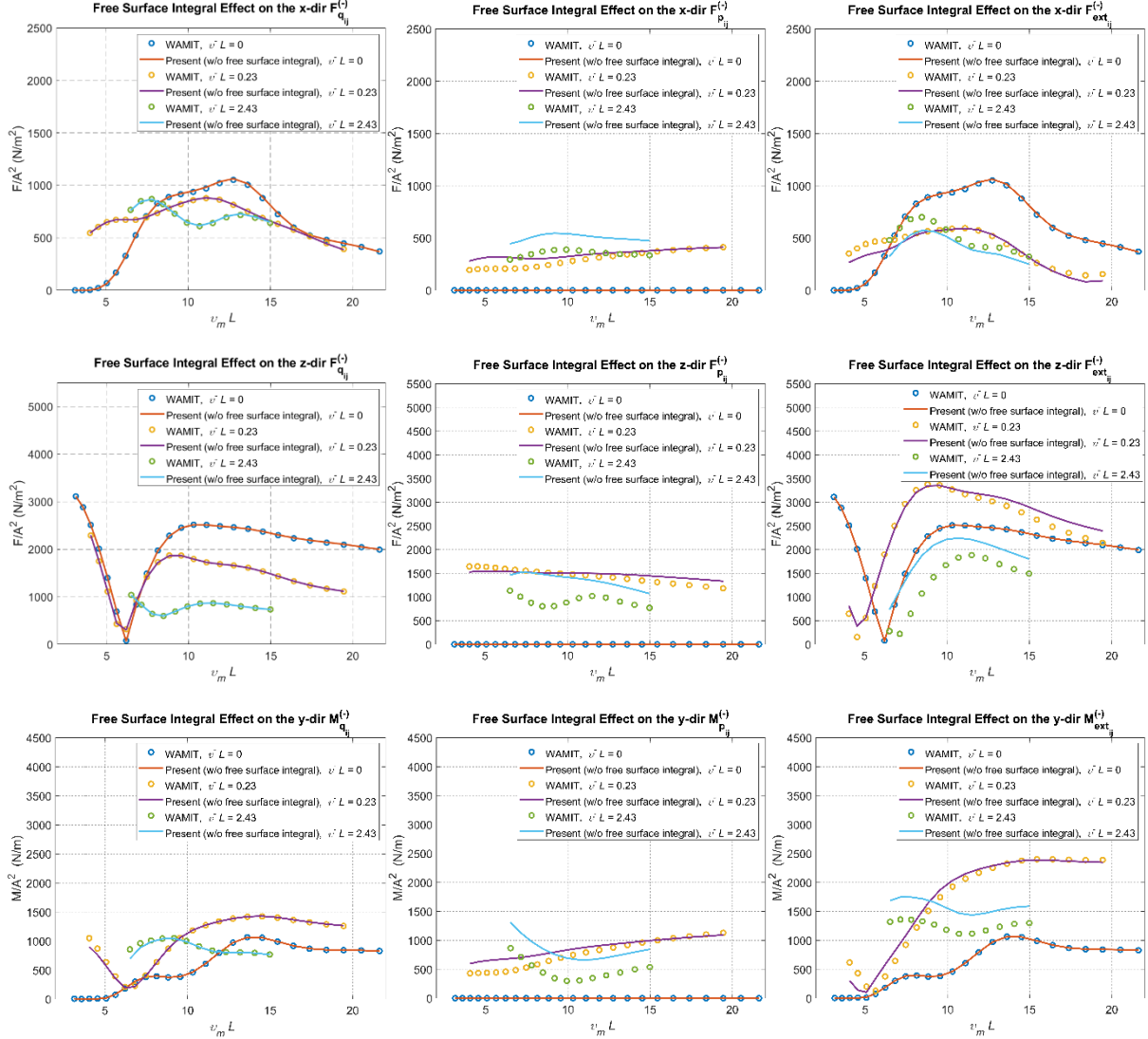


Fig. 4.2. Amplitudes comparisons of the difference frequency force and moment QTFs for Wigley II (Blunt), considering the free surface integral (bullets) and without free surface integral (solid lines)

Fig. 4.2 illustrates the free-surface-integral contribution to the 2nd order force and moment for the case without uniform flow. On the figures, $\nu_m L = (\omega_{0_i} - \omega_{0_j})^2 L / 4g$ is the non-dimensional mean frequency, and $\nu^- L = (\omega_{0_i} - \omega_{0_j})^2 L / g$ is the non-dimensional difference frequency. The results show that the free-surface-integral contribution is negligible in the total 2nd-order wave exciting force $F'_{ext,ij}$, especially when the quadratic force $F'_{q,ij}$ dominates the $F'_{ext,ij}$ close to the

QTF's main diagonal (i.e., $\omega_{0_i} \approx \omega_{0_j}$). In other words, when frequency differences are not large, the present method is reliably applicable. Note that the present results give slightly more conservative values. This conclusion also agrees with [26], which also shows the same trend for bottom-mounted cylinder.

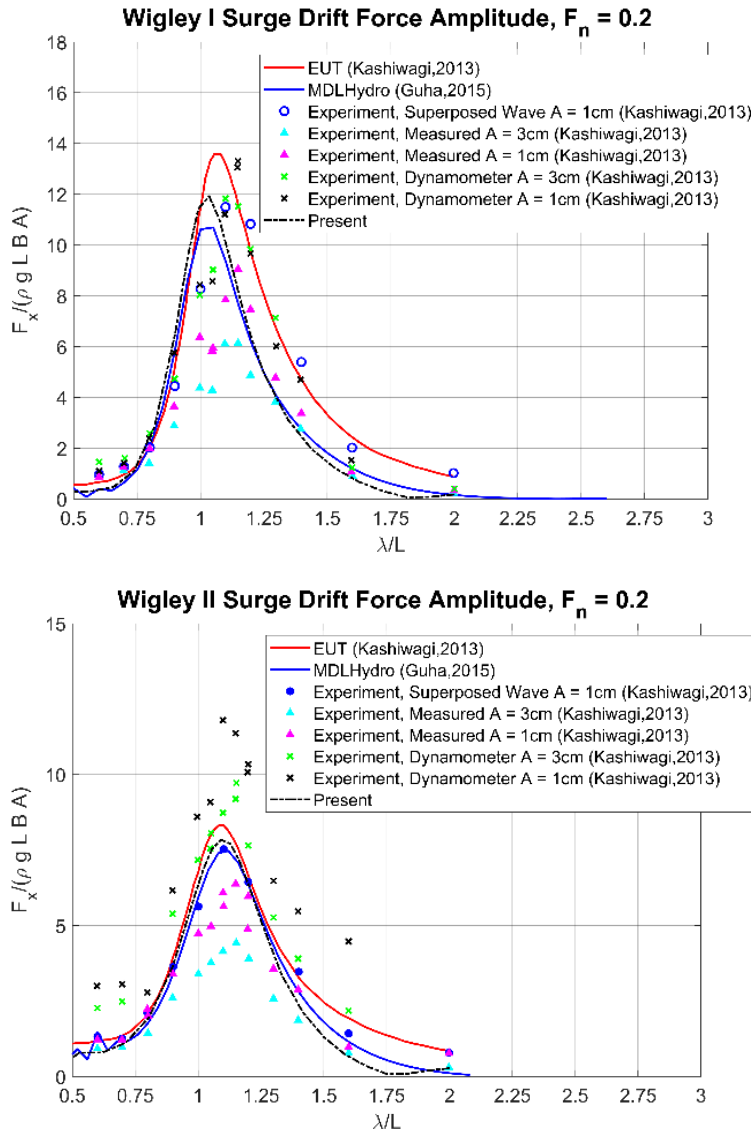


Fig. 4.3. Validation of the main-diagonal QTFs with forward speed. EUT results are from ref.[30], MDLHydro results are from ref.[37], and Experiment results are from ref.[36]

The proposed wave-uniform flow method is validated against experiments and numerical simulation data from the literature [30, 36, 37] in Fig. 4.3. The figure shows the drift force, i.e., 2nd order force in x-dir, with $\omega_{0_i} = \omega_{0_j}$, for various cases of experiments and numerical simulations. This drift force with forward speed is also called the added resistance in some literature. The present results show good agreement with other numerical simulations (EUT and MDLHydro) developed independently by [30] and [37]. The present results also correlate well with the published experimental results. The minor discrepancies may be attributed to higher-order nonlinear and viscous effects. The good comparison in second-order drift force also implies that the first-order solutions are well matched, which was confirmed but not presented here, since the 2nd order forces consist of the products of first-order quantities. It is well known that the added resistance (drift force with forward speed) is a small quantity and thus hard to measure in experiment, as shown in Fig.4. 3.

4.6. Case Study

In the previous two sections, we validated the present approach in calculating the second-order force QTFs without forward speed in bi-frequency domain and those with forward speed (or added resistance) in regular waves. In this section, the effect of the uniform flow on the 2nd-order quadratic, diffraction, and total exciting force QTFs are presented in the bi-frequency domain. The same hull shapes and sea conditions as the previous sections are used. As for the QTFs in the bi-frequency domain with forward speed, there is no published result available for comparison. The present approach is practically important in that it provides reasonably reliable QTF solution with forward speed in random waves with minimal human effort and computational time.

First, the uniform flow effects on the total surge-heave-pitch exciting force QTF for both Wigley I and Wigley II are shown in Fig. 4.4-Fig. 4.5. The figures show that the magnitudes of the QTFs' are generally increased with uniform flow (U). It implies that the added resistance with forward speed is generally larger than mean drift force without forward speed in random waves. Similarly, the mean drift force in head current is larger than that without current in random waves. For both hull shapes, the slopes of the surge-heave-pitch force QTFs near their peaks are also increased. In addition, the peak locations in the QTFs are shifted to the lower frequency region, owing to the additional $-U(\partial\phi_w/\partial x)$ in the pressure formulation.

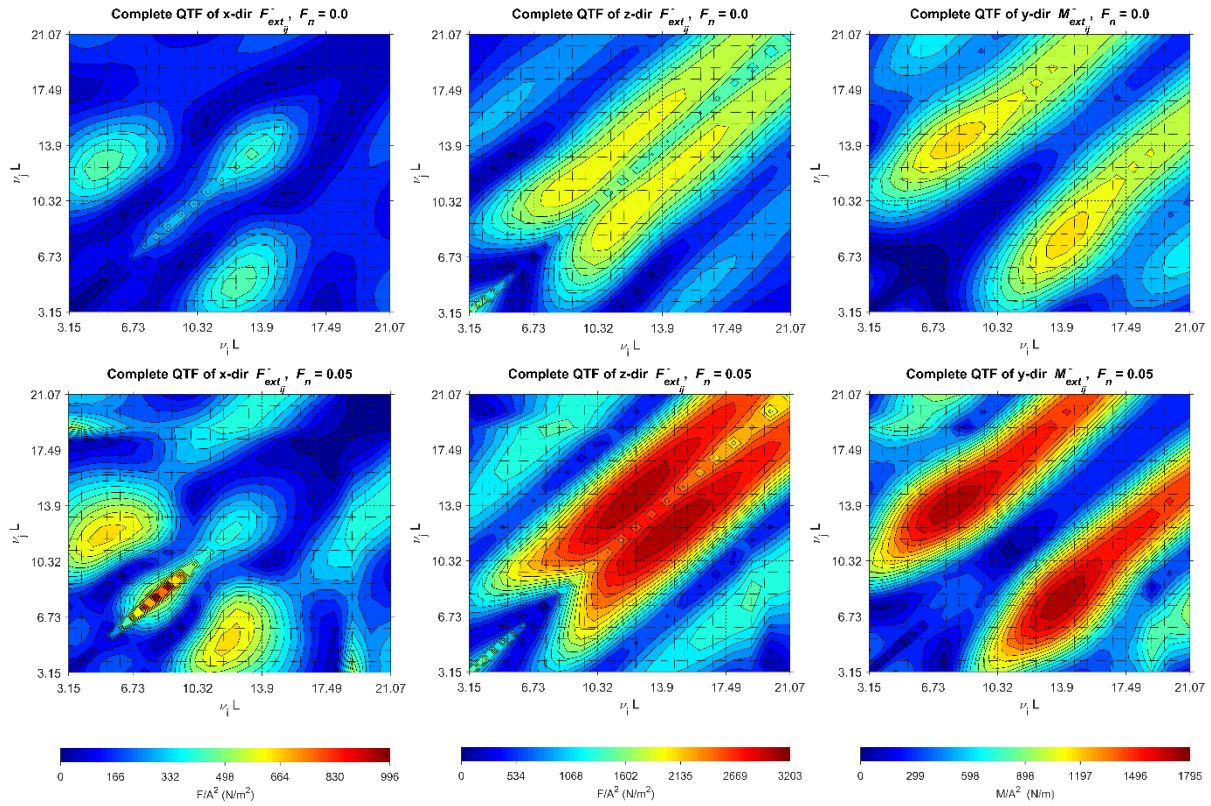


Fig. 4.4. The uniform flow effect on the complete QTF of the total wave loading of Wigley I

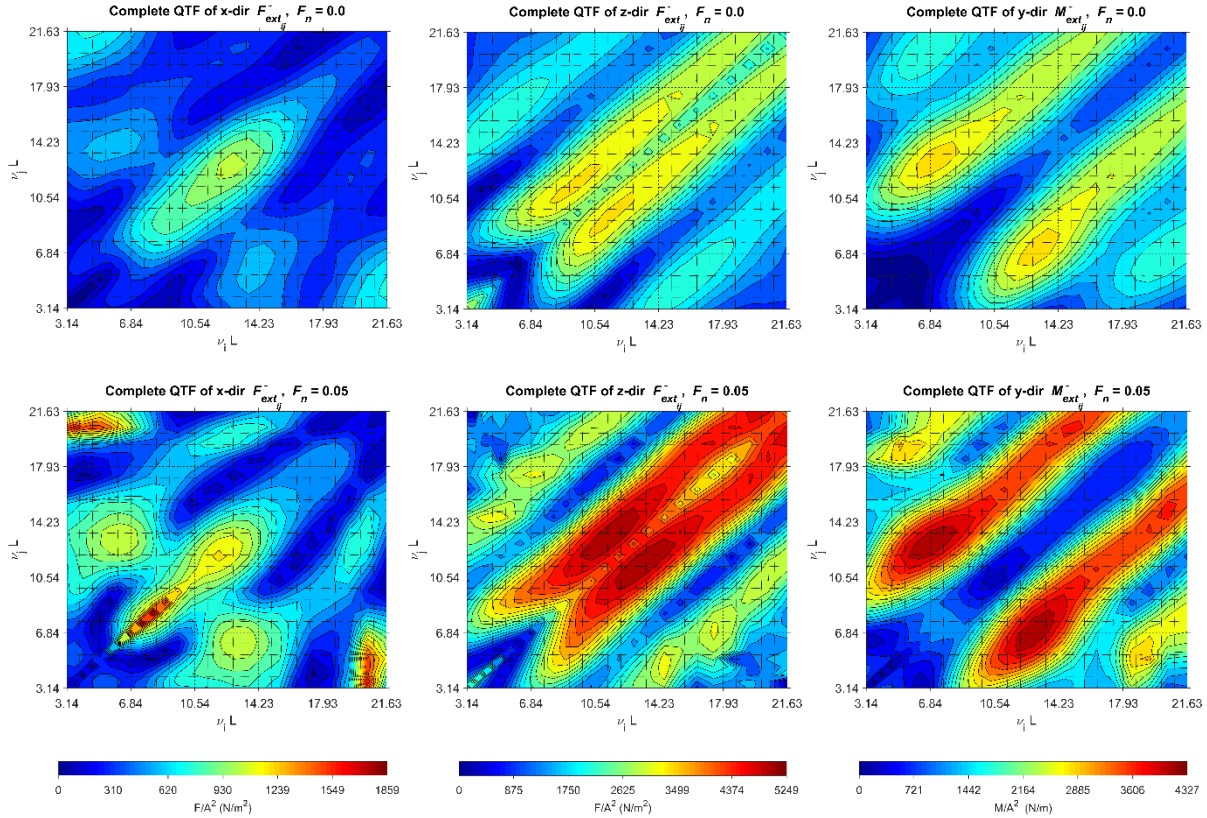


Fig. 4.5. The uniform flow effect on the complete QTF of the total wave loading of Wigley II

To examine the effect of the uniform flow more closely, the QTFs for non-dimensional difference-frequency values of $v^- = 0.00; 0.23; 2.43$ are presented in Fig. 4.6. – 4.8. Small increments of uniform flow magnitude ($F_n = 0.00; 0.02; 0.05$) are chosen to show the gradual change of the QTFs. From these figures, we can see that the total 2nd-order forces increase with U except for the surge force and pitch moment at $v^- = 0.23$ and 0 , respectively. These figures also show that the local peaks on the total exciting force are mainly attributed to the quadratic forces. These local peaks generally increase with U , except for the pitch moment at $v^- = 0.00$. All the figures shown in this section suggest that the uniform flow affects both the 2nd-order quadratic and diffraction forces and its effect is not negligible even for small uniform flow magnitude. Therefore, the importance of the uniform flow effect on the 2nd-order force QTFs cannot be understated.

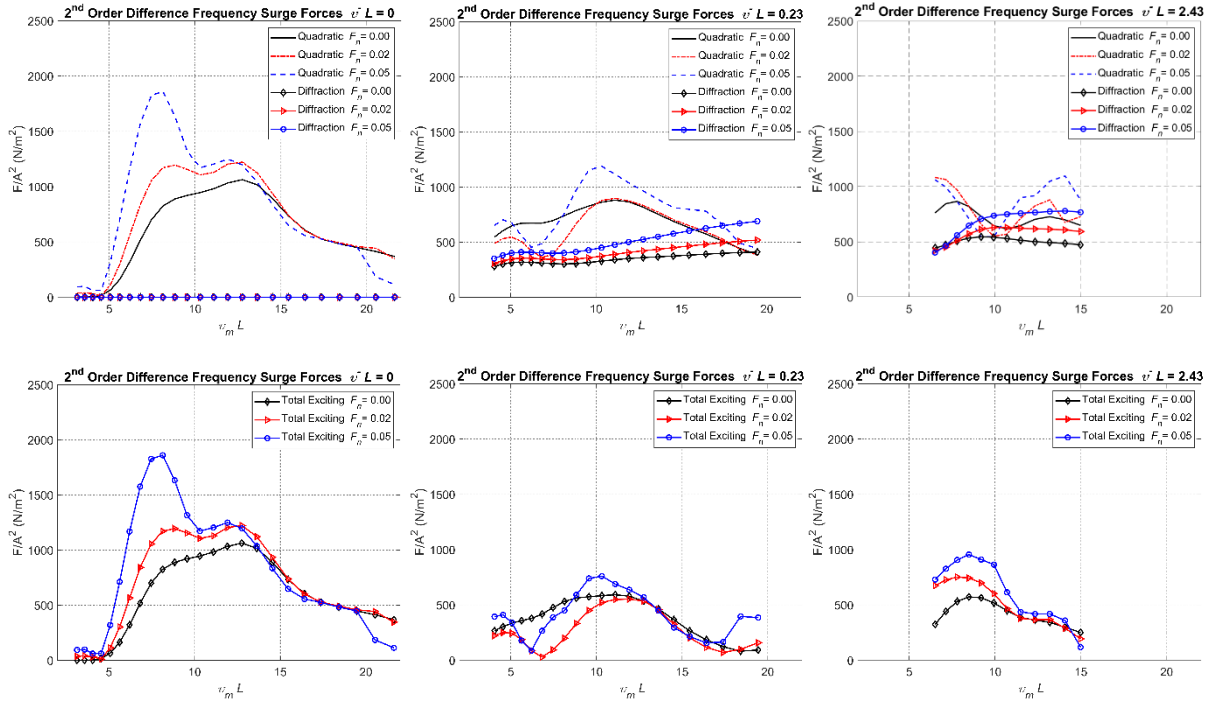


Fig. 4.6. Wigley II – uniform flow effect on difference frequency surge force components and total exciting force

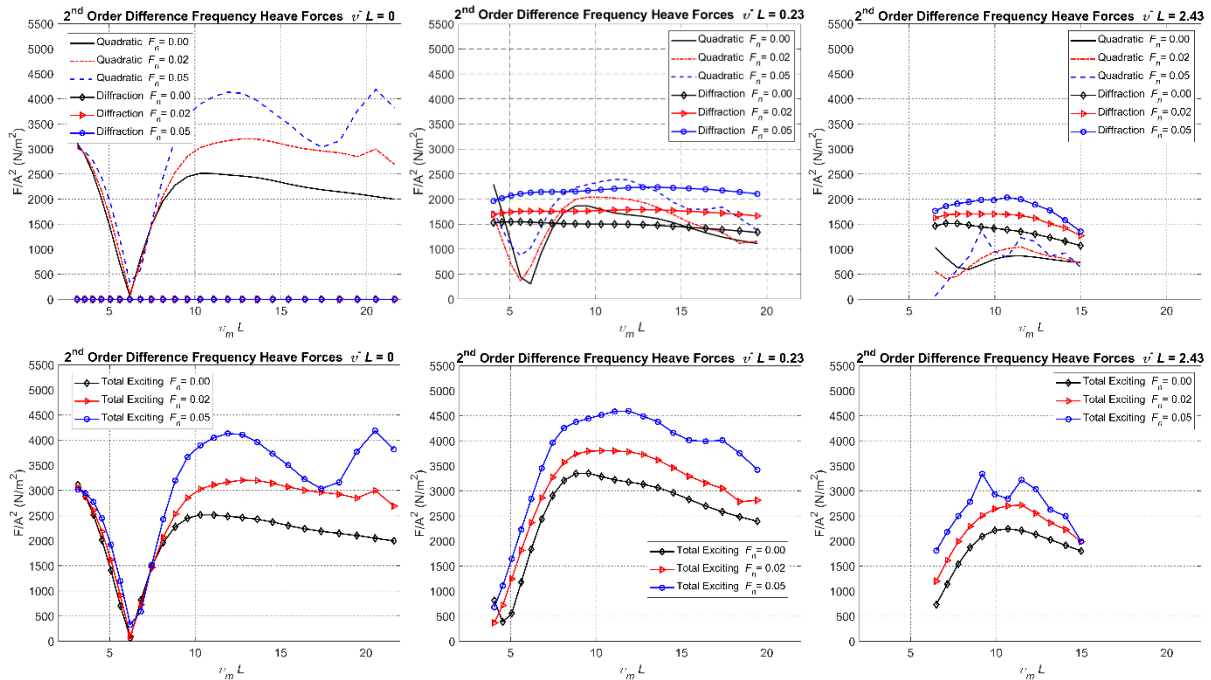


Fig. 4.7. Wigley II – uniform flow effect on difference frequency heave force components and total exciting force

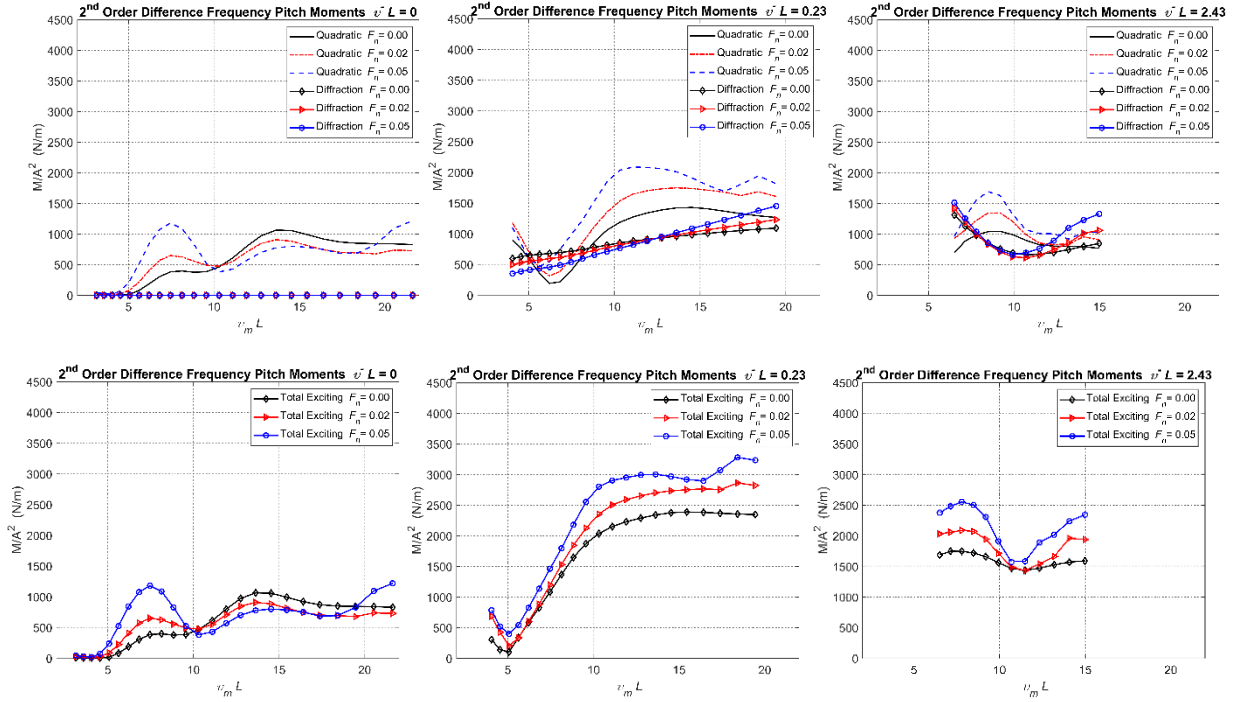


Fig. 4.8. Wigley II – uniform flow effect on difference frequency pitch moment components and total exciting force

4.7. Comparisons with Other Approximation Methods

Considering the importance of the uniform flow effect and that the QTFs' calculation in the previous sections involves a high computation complexity, several less computationally demanding solutions are examined in this section.

First, the far-field solution as presented by Aranha et al. [38] is used to calculate the horizontal drift force in regular waves with uniform flow i.e. along the main diagonal ($\omega_{0_i} = \omega_0$). Aranha et al. derived the correction factors by current to the transmitted and reflected waves acting on a floating body by utilizing the far-field approach. From the difference in energy between the incoming and transmitted waves, the drift force applied to the floating body can be formulated as

$$\mathbf{F}_{ext;ij}^-(\omega_0, U) = \frac{1}{2} \rho g A^2 |R(\omega_e, U)|^2, \text{ where } R(\omega_e, U) \text{ is the wave's reflection coefficient. The}$$

resulting drift force in the presence of current (or uniform flow) can be summarized into:

$$F_{\text{ext}_{kij}}^-(\omega_0, U) = F_{\text{ext}_{kij}}^-(\omega_e, 0)[1 - 4(Ug/\omega_0)] \quad k=1,2,6 \quad (4.46)$$

This method is far less computationally expensive compared to the direct pressure integration method even with the present uniform flow approximation. However, Aranha's far-field method also has disadvantages such as being insensitive to local hull shape variations [37], based on heuristic arguments [39], and providing no solutions for heave-pitch-roll modes. Also, Aranha's formulas were validated by more direct numerical methods by others for fixed bodies but have still been controversial for floating-body cases. A similar study for ship-shaped structures under various wave heading angles was presented by [40].

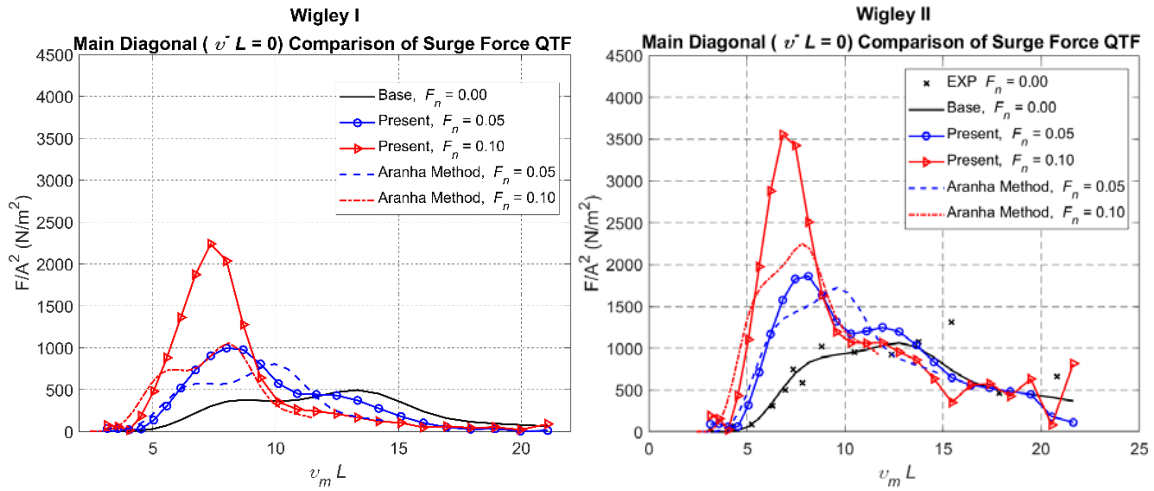


Fig. 4.9. Main diagonal comparisons of the difference frequency surge QTF between the Aranha's method and the present study

The surge drift force comparisons between the present (direct pressure integration with uniform flow approximation) and the Aranha's methods are presented in Fig. 4.9. The base value of $F_n = 0.0$ is also validated with the experiment from [36]. The figure shows that the Aranha's and present methods give comparable results for both hull shapes when the uniform-flow magnitude is relatively small ($F_n \ll 0.1$). However, for higher uniform-flow magnitude, Aranha's method tends to underpredict the maxima of the drift force. Note that the peaks of drift forces with

forward speed $F_n=0.2$ by the present method were validated against experimental results in Fig. 4.3. Xie and Falzarano in [40] also presented the similar conclusion for different hull shapes and various wave heading angles.

Next, we examine a couple of other approximation methods that utilize the main-diagonal values to predict the off-diagonal QTF values, called Newman's approximation [41]. These approximations require less computational effort since only the diagonal values depending only on the quadratic products of linear quantities need to be computed. Similar studies for zero uniform flow case were conducted in [42, 43]. In the present study, two Newman's approximation methods are used to predict the off-diagonal QTFs with uniform flow. These approximation methods use the arithmetic mean or geometric mean, as given in eq.(4.47) and eq.(4.48), respectively.

$$\mathbf{F}_{\text{ext}ij}^- = \frac{\mathbf{F}_{\text{ext}ii}^- + \mathbf{F}_{\text{ext}jj}^-}{2} \quad (4.47)$$

$$\mathbf{F}_{\text{ext}ij}^- = \text{sgn}(\mathbf{F}_{\text{ext}ii}^-) \sqrt{\mathbf{F}_{\text{ext}ii}^- \cdot \mathbf{F}_{\text{ext}jj}^-} \quad (4.48)$$

The effect of the uniform flow on the surge QTFs' diagonal is considered by using both the uniform flow approximation and the Aranha's method. For other degrees of freedom, only the uniform flow approximation method is considered. The Froude number of $F_n = 0.05$ is used so that the Aranha's formula is valid. All of the approximation-method combinations are presented in Table 4.3. From all the cases presented in Table 4.3, the Approx 1 and Approx 2 cases require the least computational effort, while the Def case requires the highest computational effort.

Fig. 4.10-Fig. 4.12 show the off-diagonal QTF results calculated by the methods presented in Table 4.3. It shows that for the same diagonal values, the arithmetic and geometric mean models give similar results. Even for small difference frequency pairs, no approximation methods give

reliable results when compared to the direct pressure integration method. For both the pitch moment and heave force, eq.(4.47) and eq.(4.48) under-predict the actual values. This under-prediction is caused by the positive QTF slopes near the heave and pitch diagonals (see Fig. 4.4-Fig. 4.5). The same conclusion was found in [26] in the case without uniform flow.

According to Fig. 4.4-Fig. 4.5, the slope of the QTFs near the diagonal is also significantly increased by the presence of the uniform flow. These steep slopes cause the eq.(4.47)-eq.(4.48) to over predict the actual value of the off-diagonal surge QTF (see Fig. 4.10 - Fig. 4.12), despite having a negative slope near its main-diagonals. The results show that when the uniform flow is involved, it is important to directly solve the off-diagonal QTFs without using any main-diagonal approximation methods.

Table 4.3. Approximation-methods to calculate the off-diagonal QTFs

Case	Diagonal ($\omega_{0_i} = \omega_{0_j}$)	Off-Diagonal ($\omega_{0_i} \neq \omega_{0_j}$)	DOF
Def	Present model	Present model	Surge, heave, pitch
Approx 1	Present model	Arithmetic mean, eq.(4.47)	Surge, heave, pitch
Approx 2	Present model	Geometric mean, eq.(4.48)	Surge, heave, pitch

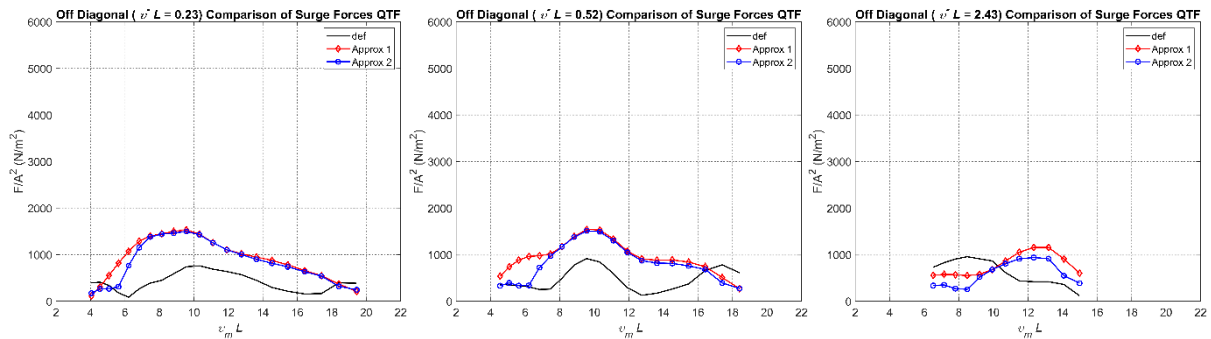


Fig. 4.10. Comparisons of the off-diagonal difference-frequency QTFs between various approximation methods – surge of Wigley II hull

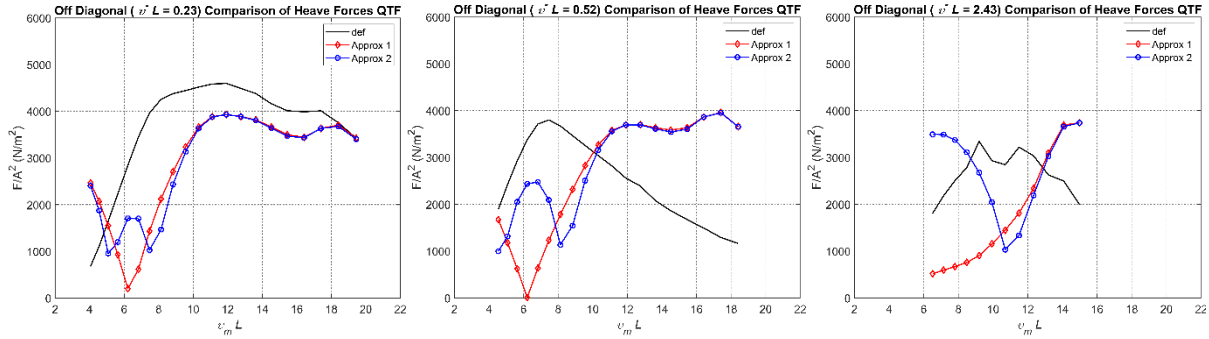


Fig. 4.11. Comparisons of the off-diagonal difference-frequency QTFs between various approximation methods - heave of Wigley II hull

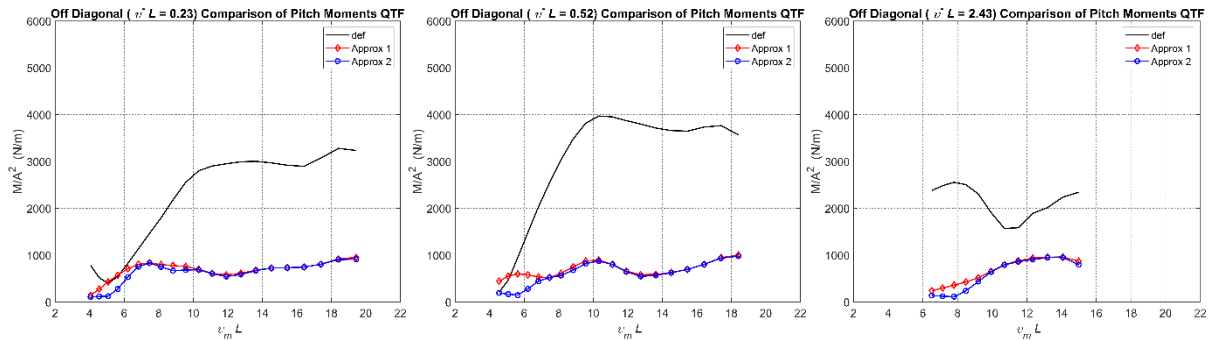


Fig. 4.12. Comparisons of the off-diagonal difference-frequency QTFs between various approximation methods - pitch of Wigley II hull

The importance of solving the off diagonal QTFs is further demonstrated in irregular wave’s analysis (eq.(4. 39)-(4.41)). The case of JONSWAP wave’s spectra with $H_s = 0.075\text{m}$, $T_p = 1.18$ sec, and $\gamma=3$ in head seas condition is simulated for Wigley II hull. In a full scale model ($L_{pp} = 100\text{m}$) this case corresponds to $H_s = 3\text{m}$ and $T_p = 7.5$ sec. The total slowly varying surge force and wave’s spectra can be seen in Fig. 4.13 and the corresponding time series can be seen in Fig. 4.14. The results shows that the Newman’s diagonal approximations tends to over predict the force, especially when uniform flow is present. Ma et.al. [33] also shows the same trend for different type of hull in the case without uniform flow. Note that in the case with uniform flow, a good force estimates close to $\delta\omega = 0$ was not achieved.

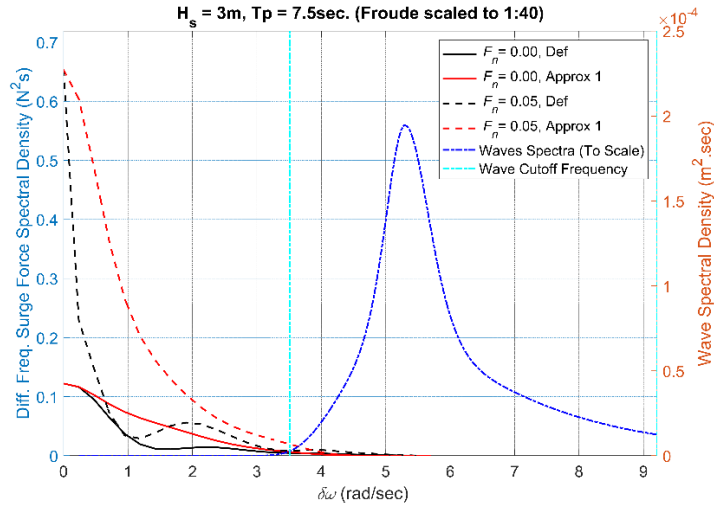


Fig. 4.13. Irregular wave's spectra and the corresponding slowly varying force power spectra density

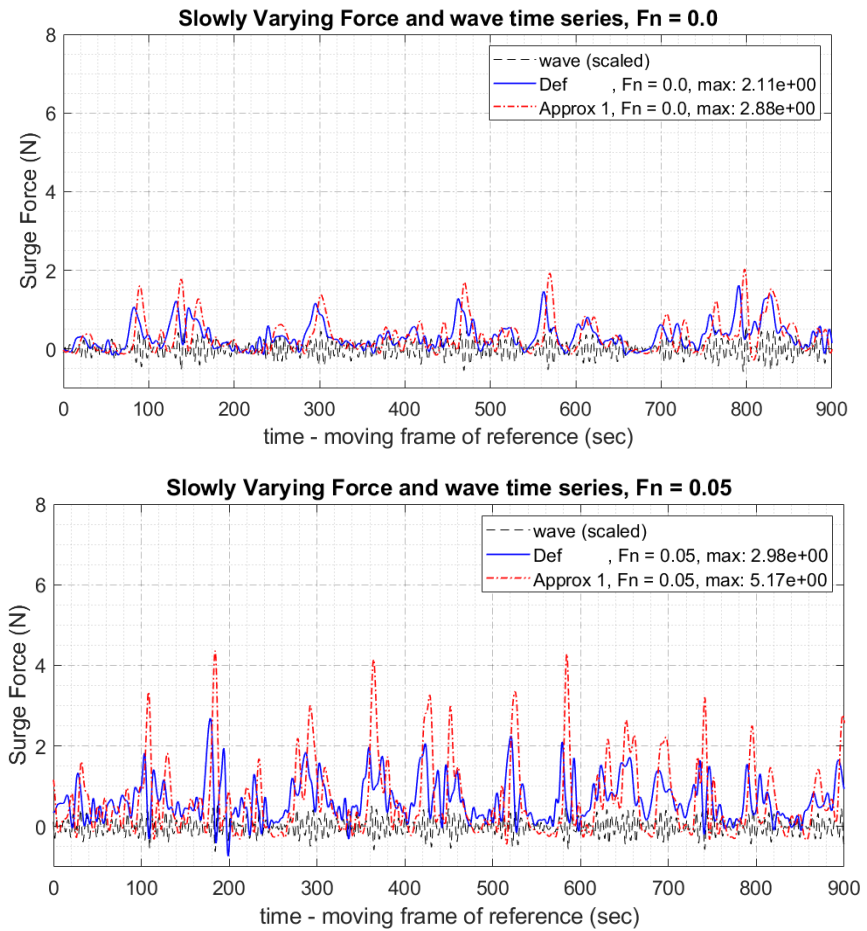


Fig. 4.14. Time series comparison between the present method, and Newman's approximation method

4.8. Conclusions

In this paper, an efficient method to compute second-order difference-frequency wave loads in the presence of uniform flow in the frequency domain was presented. A slender body with small uniform flow magnitude was assumed to reduce the numerical complexity associated with body-disturbance flow and steady Kelvin-ship wave. Under the assumptions, the complete second-order difference-frequency wave loads in uniform current (or forward speed) were obtained except for the term from free-surface integral, which is known to be relatively unimportant in the case of difference-frequency force QTFs. In this regard, the discretization of the free surface was avoided in the proposed method, thus reducing the programming effort and computational burden. In spite of employing those approximations, the present numerical results agreed well against more complete second-order QTF results from a commercial program WAMIT in the case of zero current (or forward speed). As for the second-order mean-drift forces with current, the present results also agreed well against published experimental and more complex numerical results. In the case of the off-diagonals terms of the difference-frequency QTFs with forward speed, no comparison was made since no published results were available.

From our numerical results, it is seen that the uniform flow has a significant influence on both the difference frequency quadratic and diffraction forces. Both the main-diagonal and off-diagonal parts of the difference frequency force QTFs were affected by the uniform flow and the uniform flow generally increased the total force magnitudes and their slopes. The uniform flow also shifted the QTF-peak locations mainly due to the encounter-frequency effect.

Due to the numerical complexity associated with solving the 2nd order boundary problem with uniform flow in the frequency domain, other approximation methods, such as Aranha's method and Newman's approximation, also exist. Aranha's method only showed similar mean-drift-force

results compared with the present method when Froude number is relatively small ($F_n < 0.1$). In addition, the Newman's diagonal approximations that evaluate the off-diagonal QTFs in terms of the diagonal QTFs showed unreliable results when compared to the more exact present solution, especially when the uniform flow is considered. These results further emphasize the importance of the presently developed practical approach incorporating simplified but essential features of the uniform flow effects on difference-frequency force QTFs.

4.9. References

- [1] R. Timman and J. Newman, "The Coupled Damping Coefficients of a Symmetric Ship," *Journal of Ship Research*, 1963.
- [2] N. Salvesen, E. Tuck, and O. Faltinsen, "Ship motions and sea loads," vol. 78, ed, 1970, pp. 250-287.
- [3] T. Ogilvie and E. Tuck, "A rational strip theory of ship motions: part I," ed, 1969, pp. 107-107.
- [4] J. Hess, "Calculation of Nonlifting Potential Flow About Arbitrary Three-Dimensional Bodies," *Journal of Ship Research*, 1964.
- [5] F. R. S. Sir Thomas Havelock, "Waves due to a floating sphere making periodic heaving oscillations," *Proceedings of the Royal Society of London. Series A. Mathematical and Physical Sciences*, vol. 231, no. 1184, pp. 1-7, 1955.
- [6] J. V. Wehausen and E. V. Laitone, "Surface Waves," vol. 9: Springer-Verlag, Berlin, 1960, pp. 446-778.
- [7] C. C. Mei, *The applied dynamics of ocean surface waves*. Singapore ; River Edge, N.J. : World Scientific, 1989.
- [8] J. G. Telste and F. Noblesse, "Numerical evaluation of the Green function of water-wave radiation and diffraction," *Journal of Ship Research*, vol. 30, no. 2, pp. 69-84, 1986.
- [9] R. Zhao and O. Faltinsen, "A discussion of the m-terms in the wave current body interaction problem," ed. Trondheim - Norway: 4th Int. Workshop on Water Waves and Floating Bodies {(IWWWFB)}, 1989.
- [10] A. Papanikolaou and T. Schellin, "A three-dimensional panel method for motions and loads of ships with forward speed," *Ship Technology Research (Schiffstechnik)*, vol. 39, no. 4, pp. 145-155, 1992.

- [11] J. Grue and D. Biberg, "Wave forces on marine structures with small speed in water of restricted depth," *Applied Ocean Research*, vol. 15, no. 3, pp. 121-135, 1993.
- [12] D. J. Kim and M. H. Kim, "Wave-current interaction with a large three-dimensional body by THOBEM," *Journal of Ship Research*, vol. 41, no. 4, pp. 273-285, 1997.
- [13] A. Guha and J. Falzarano, "Estimation of hydrodynamic forces and motion of ships with steady forward speed," *International Shipbuilding Progress*, vol. 62, no. 3-4, pp. 113-138, 2016.
- [14] R. Brard, "Representation of a given ship form by singularity distributions when the boundary condition on the free surface is linearized," *Journal of Ship Research*, vol. 16, no. 1, pp. 79-92, 1972.
- [15] P. Guevel, P. Vaussy, and J. M. Kobus, "Distribution of Singularities Kinematically Equivalent To a Moving Hull in the Presence of a Free Surface," *International Shipbuilding Progress*, vol. 21, no. 243, pp. 311-324, 1974.
- [16] H. Li, L. z. Hao, X. b. Chen, and H. l. Ren, "The computation of forward speed Green function in cylindrical coordinate system," *European Journal of Mechanics, B/Fluids*, vol. 69, pp. 76-86, 2018.
- [17] H. Liang, Z. Ren-chuan, M. Guo-ping, and F. Ju, "Study on Havelock form translating-pulsating source Green's function distributing on horizontal line segments and its applications," *Ocean Engineering*, vol. 124, pp. 306-323, 2016.
- [18] D. Bruzzone, C. Gironi, and A. Grasso, "Nonlinear effects on motions and loads using an iterative time-frequency solver," *International Journal of Naval Architecture and Ocean Engineering*, vol. 3, no. 1, pp. 20-26, 2011.
- [19] X. Chen, R. c. Zhu, J. Zhao, W. j. Zhou, and J. Fan, "Study on weakly nonlinear motions of ship advancing in waves and influences of steady ship wave," *Ocean Engineering*, vol. 150, no. February, pp. 243-257, 2018.
- [20] M. Shen and Y. Liu, "Current effects on global motions of a floating platform in waves," *Ocean Systems Engineering*, vol. 7, no. 2, pp. 121-141, 2017.
- [21] M. S. Celebi, M. H. Kim, and R. F. Beck, "Fully Nonlinear 3-D Numerical Wave Tank Simulation," *Journal of Ship Research*, vol. 42, no. 1, pp. 33-45, 1998.
- [22] O. M. Faltinsen and A. E. Løken, "Slow drift oscillations of a ship in irregular waves," *Applied Ocean Research*, vol. 1, no. 1, pp. 21-31, 1979.
- [23] M. J. Lighthill, "Waves and Hydrodynamic Loading," London, 1979, pp. 1-40.
- [24] B. Molin, "Second-order diffraction loads upon three-dimensional bodies," *Applied Ocean Research*, vol. 1, no. 4, pp. 197-202, 1979.

- [25] M. H. Kim, "Second-order sum-frequency wave loads on large-volume structures," *Applied Ocean Research*, vol. 13, no. 6, pp. 287-296, 1991.
- [26] M. H. Kim, "Difference-frequency wave loads on a large body in multi-directional waves," *Applied Ocean Research*, vol. 14, no. 6, pp. 353-370, 1992.
- [27] M. H. Kim and D. K. P. Yue, "The complete second-order diffraction solution for an axisymmetric body part 2. Bichromatic incident waves and body motions," *Journal of Fluid Mechanics*, vol. 211, pp. 557-593, 1990.
- [28] M. H. Kim and D. K. P. Yue, "Sum- and difference-frequency wave loads on a body in unidirectional Gaussian seas," *Journal of Ship Research*, 1991.
- [29] C. H. Lee and X. Zhu, "Second-order diffraction and radiation solutions on floating bodies," ed, 1993, pp. 61-64.
- [30] M. Kashiwagi, "Prediction of Surge and its Effect on Added Resistance by Means of the Enhanced Unified Theory," *Trans West-Japan Society of Naval Architects*, no. 89, pp. 77-89, 1995.
- [31] J. Skourup, K. F. Cheung, H. B. Bingham, and B. Büchmann, "Loads on a 3D body due to second-order waves and a current," *Ocean Engineering*, vol. 27, no. 7, pp. 707-727, 2000.
- [32] Y. L. Shao and O. M. Faltinsen, "Second-Order Diffraction and Radiation of a Floating Body With Small Forward Speed," *Journal of Offshore Mechanics and Arctic Engineering*, vol. 135, no. 1, 2013.
- [33] S. Ma, M. H. Kim, and S. Shi, "Second-order low-frequency wave forces on a SPM offloading tanker in Shallow Water," *Journal of Offshore Mechanics and Arctic Engineering*, vol. 131, no. 4, pp. 1-6, 2009.
- [34] C. H. Lee, "WAMIT Theory Manual," *WAMIT Theory Manual*, pp. 1-19, 1995.
- [35] R. M. Isherwood, "Technical note: A revised parameterisation of the Jonswap spectrum," *Applied Ocean Research*, vol. 9, no. 1, pp. 47-50, 1987.
- [36] M. Kashiwagi, "Hydrodynamic study on added resistance using unsteady wave analysis," *Journal of Ship Research*, vol. 57, no. 4, pp. 220-240, 2013.
- [37] A. Guha and J. Falzarano, "The effect of hull emergence angle on the near field formulation of added resistance," *Ocean Engineering*, vol. 105, pp. 10-24, 2015.
- [38] J. A. P. Aranha, "A formula for 'wave damping' in the drift of a floating body," *Journal of Fluid Mechanics*, vol. 275, pp. 147-155, 1994.
- [39] D. Trassoudaine and M. Naciri, "A comparison of a heuristic wave drift damping formula with experimental results," vol. 21, pp. 93-97, 1999.

- [40] Z. Xie and J. Falzarano, "Study on 2nd Order Wave Loads With Forward Speed Through Aranha's Formula and Neuman-Kelvin Linearization," in *39th International Conference on Ocean, Offshore & Arctic Engineering*, Virtual, Online, 2020: OMAE
- [41] J. N. Newman, "Second-order slowly varying forces on vessels in irregular waves," London, pp. 182-182.
- [42] A. Somayajula and J. Falzarano, "A comparative assessment of approximate methods to simulate second order roll motion of FPSOs," *Ocean Systems Engineering*, vol. 7, no. 1, pp. 53-74, 2017.
- [43] Z. Xie, Y. Liu, and J. Falzarano, "A Numerical Evaluation of the quadratic transfer function for a floating structure," in *38th International Conference on Ocean, Offshore & Arctic Engineering*, Glasgow, Scotland, UK, 2019, pp. 1-13: OMAE.

5. RANS CFD SIMULATION OF WAVE-UNIFORM CURRENT INTERACTION WITH SLENDER BODY

5.1. Background and Literature Review

CFD is well known for its capabilities for solving non-linear fluid-structure interactions. Although several completely non-linear BEMs were also capable of simulating highly non-linear motions under wave excitations (i.e., [1]), they still assume non-breaking waves and inviscid fluids. On the contrary, the CFD method solved the completely non-linear fluid-structure interaction by considering real fluid conditions, including the viscous effects and breaking waves [2-4]. The viscous effect is typically crucial in the case where flow separation is high (e.g., FPSO's oblique current loads [5]) or when the damping is dominated by viscous effect (e.g., bilge keel roll damping [6]). However, for mild seas condition cases with small wave's heading angle, the forcing and motion is typically pressure dominated, so the inviscid fluid's assumption can still be used in the CFD simulation to save computation time [7].

Many studies show that the CFD gives very reliable results when set up correctly in the wave's radiation-diffraction problems. For instance, [8] shows a good agreement between the CFD and experiment for head seas and oblique wave's condition with 0 forward speed. Seakeeping validation for moderate Froude number $0.1 < F_n < 0.25$ were investigated in [9-11] for both short and long wave's length, and head seas and oblique wave directions. Even more complicated loading conditions were shown in [2], where bi-directional seas are considered in the seakeeping analysis, and in [12], where a high speed ($F_n = 0.7$) trimaran vessel is simulated. All of these

versatility and capabilities comes at a cost, with the RANS method requires considerably larger computational resources compared to the standard BEM. In addition, the typical CFD methods requires many numerical tuning parameters and also require an intensive effort to set it up. When not set up properly, identical problems might yield different solutions. To tackle this problem, several efforts led by the industry were made to standardize the best practice in simulating practical engineering problem by using CFD tools [5, 13].

This section investigates the completely non-linear wave-uniform flow simulation by an industry-standard RANS-based CFD software. Noting that the wave-uniform flow coupling is completely non-linear in the CFD simulation, we can expect a better numerical representation than the BEM method. Special cases of wave periods that excites the pitch resonance are simulated to excite large motion so that the non-linearity effect is pronounced. By comparing the proposed UF approximation method in the previous sections with the CFD solutions, we can also gain a better understanding of its capabilities and limitations.

5.2. Theory and Implementations

5.2.1. Navier-Stokes Equation

An industry-standard CFD software Star-CCM+ is used to model the fully non-linear fluid-structure interaction. Star-CCM+ software capabilities include, but not limited to, solving for the fluid flow problem in both turbulent and laminar regimes by using the Finite Volume Method. The governing equation is based on the mass, momentum, and energy conservation in the form of continuity, Navier-Stokes, and the first law of thermodynamic equations.

$$\frac{\partial \rho}{\partial t} + \nabla \cdot (\rho \mathbf{v}) = 0 \tag{5.1}$$

$$\frac{\partial(\rho\mathbf{v})}{\partial t} + \nabla \cdot (\rho\mathbf{v} \otimes \mathbf{v}) = -\nabla \cdot (p\mathbf{I}) + \nabla \cdot \mathbf{T} + \mathbf{f}_b \quad (5.2)$$

$$\frac{\partial(\rho E)}{\partial t} + \nabla \cdot (\rho E\mathbf{v}) = -\nabla \cdot (\mathbf{v} \cdot p\mathbf{I}) - \nabla \cdot (\mathbf{v} \cdot \mathbf{T}) + \mathbf{f}_b \cdot \mathbf{v} + S_E \quad (5.3)$$

where \otimes is the outer product operator, ρ is the fluid's density per unit volume, \mathbf{v} is the velocity vector, p is the pressure, \mathbf{I} is the identity matrix, \mathbf{f}_b is the resultant body force (such as gravity or centrifugal force), S_E is the energy source per unit volume, and \mathbf{T} is the viscous or shear stress tensor, defined as:

$$\mathbf{T} = \mu \begin{bmatrix} 2 \frac{\partial u_x}{\partial x} & \left(\frac{\partial u_x}{\partial y} + \frac{\partial u_y}{\partial x} \right) & \left(\frac{\partial u_x}{\partial z} + \frac{\partial u_z}{\partial x} \right) \\ & 2 \frac{\partial u_y}{\partial y} & \left(\frac{\partial u_y}{\partial z} + \frac{\partial u_z}{\partial y} \right) \\ \text{Sym} & & 2 \frac{\partial u_z}{\partial z} \end{bmatrix} \quad (5.4)$$

where μ , u_x , u_y , and u_z is the dynamic viscosity of fluid, x-component velocity, y- component velocity, and z-component velocity, respectively. These governing equations are then used to solve the mass, velocity, energy, and stresses over a finite control volume (cell). This is done by solving the weak form (integral form) of the differential equations in each time step. However, most of the cases resulted in more unknown variables than the number of equations. Therefore, several constitutive laws, such as the turbulence model and equation of state, are needed to close the model. For marine application, the fluid's density is kept at a constant value ρ_0 , while other closure models are explained below.

5.2.2. Reynold Averaged Navier-Stokes and Turbulence Closure Model

In the RANS model, the fluctuated variables, e.g., ϕ , can be represented as a mean value and its perturbation, i.e.:

$$\phi = \bar{\phi} + \phi' \quad (5.5)$$

where $\bar{\phi}$ is the average value of ϕ over a particular time or spatial scale, and ϕ' is the perturbation along $\bar{\phi}$, such as illustrated in Fig. 5.1.

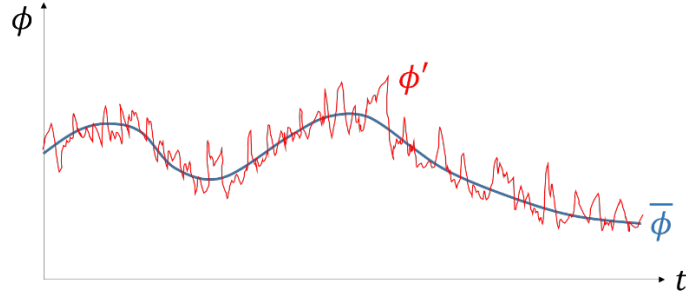


Fig. 5.1. Variables description in RANS formulation

Substituting eq.(5.5) into eq.(5.1)-(5.3), the governing equations for the RANS models are written as:

$$\frac{\partial \rho}{\partial t} + \nabla \cdot (\rho \bar{\mathbf{v}}) = 0 \quad (5.6)$$

$$\frac{\partial(\rho \bar{\mathbf{v}})}{\partial t} + \nabla \cdot (\rho \bar{\mathbf{v}} \otimes \bar{\mathbf{v}}) = -\nabla \cdot (\bar{p} \mathbf{I}) + \nabla \cdot (\bar{\mathbf{T}} + \mathbf{T}_{RANS}) + \mathbf{f}_b \quad (5.7)$$

$$\frac{\partial(\rho \bar{E})}{\partial t} + \nabla \cdot (\rho \bar{E} \bar{\mathbf{v}}) = -\nabla \cdot (\bar{p} \mathbf{I}) \bar{\mathbf{v}} - \nabla \cdot (\bar{\mathbf{T}} + \mathbf{T}_{RANS}) \bar{\mathbf{v}} + \mathbf{f}_b \cdot \bar{\mathbf{v}} + S_E \quad (5.8)$$

Note that eq.(5.1)-(5.3) and eq.(5.6)-(5.8) are almost identical, except for the additional Reynold stress tensor \mathbf{T}_{RANS} in the RANS formulation which is defined as:

$$\mathbf{T}_{RANS} = -\rho \begin{bmatrix} 2k_{TE} + \overline{u'_x u'_x} & \overline{u'_x u'_y} & \overline{u'_x u'_z} \\ \text{Sym} & 2k_{TE} + \overline{u'_y u'_y} & \overline{u'_y u'_z} \\ & & 2k_{TE} + \overline{u'_z u'_z} \end{bmatrix} \quad (5.9)$$

where k_{TE} is the turbulent kinetic energy. Note that \mathbf{T}_{RANS} is a non-linear term, consisting of multiplication between two unknown variables. Therefore, a turbulence closure model to describe

the \mathbf{T}_{RANS} in terms of the mean value is needed to solve the RANS equations. One of the most practical and straight forward approaches is by employing the Boussinesq hypothesis, i.e., the small scale turbulent stress \mathbf{T}_{RANS} is assumed to be linearly proportional to the large scale mean stress \mathbf{T} . In other words, the Boussinesq hypothesis requires that $\overline{u'_x u'_y} \sim \frac{1}{2} \left(\frac{\partial \overline{u_x}}{\partial y} + \frac{\partial \overline{u_y}}{\partial x} \right)$. By employing this hypothesis, the Reynold stress tensor formula (5.9) can be rewritten into:

$$\mathbf{T}_{RANS} = \rho \nu_T \begin{bmatrix} 2 \left(k_{TE} / \nu_T + \frac{\partial \overline{u_x}}{\partial x} \right) & \left(\frac{\partial \overline{u_x}}{\partial y} + \frac{\partial \overline{u_y}}{\partial x} \right) & \left(\frac{\partial \overline{u_x}}{\partial z} + \frac{\partial \overline{u_z}}{\partial x} \right) \\ & 2 \left(k_{TE} / \nu_T + \frac{\partial \overline{u_y}}{\partial y} \right) & \left(\frac{\partial \overline{u_y}}{\partial z} + \frac{\partial \overline{u_z}}{\partial y} \right) \\ \text{Sym} & & 2 \left(k_{TE} / \nu_T + \frac{\partial \overline{u_z}}{\partial z} \right) \end{bmatrix} \quad (5.10)$$

Due to the introduction of the turbulent eddy viscosity ν_T , this approach is also called the Eddy viscosity model. Although it is called ‘viscosity’, ν_T is entirely different from the fluid’s kinematic viscosity $\nu = \mu / \rho$. Where the latter is a fluid’s intrinsic property, the former is a flow property that highly dependent on the flow condition itself. Several different closure models are developed to provide constitutive relations to solve for the turbulent eddy viscosity and turbulent kinetic energy. These closure models include but are not limited to Sparrat Almaras, $k - \epsilon$, and $k - \omega$ model.

According to recent development on the standard CFD practice in the industry [13], $k - \omega$ is the preferred choice of turbulence model when dealing with minimum flow separation and no eddy detachment in marine application involving free surface waves. In summary, the $k - \omega$ model solves for eddy viscosity ν_T by solving the transport equations of two turbulence related variables: the turbulent kinetic energy k_{TE} and the dissipation rate per unit kinetic energy stream ω_{TE} . The detailed derivation, validation, and comparative study of the $k - \omega$ model can be found in [14].

However, from preliminary test cases, it is found that the laminar model is sufficient to solve the diffraction force and ship's motion when the uniform flow is not involved. Therefore, to reduce the computation cost, the laminar model is used for wave only cases while the $k - \omega$ with boundary layer mesh refinement is used for the wave with uniform flow cases.

In real fluids, there exists a small thin layer of fluid close to a boundary where the viscous force is at least of the same magnitude as that of the inertial force. This so-called boundary layer typically has a thickness of much smaller magnitude compared to the stream-wise characteristic length of the flow, i.e., $\delta/L_x \ll 1$, where δ is the boundary layer thickness and L_x is the stream-wise characteristic length. The definition of the boundary layer can be seen in Fig. 5.2.

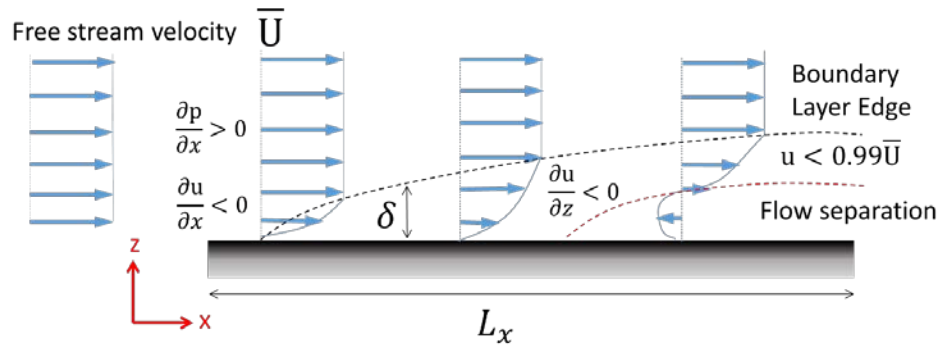


Fig. 5.2. Description of boundary layer

Recalling equation (5.4) and (5.10), the viscous effect in the boundary layer, such as illustrated in Fig. 5.2, causes shear stress along the stream-wise direction of the flow. Note that the boundary layer thickness is proportional to the fluid's viscosity and that the thicker boundary layer causes smaller shear stress (due to smaller velocity gradient).

In turbulent flow, the boundary layer is thinner compared to that of the laminar flow. This is due to the additional turbulent kinetic energy and eddy viscosity, causing higher shear stress in high Reynolds number flow. Furthermore, the shear stress can also cause the flow to separate from

the body when the conditions are met. This separation effectively causes a pressure-driven non-zero resultant force in the stream-wise direction to appear, an important phenomenon that is not considered in the potential flow theory (D’Alambert’s paradox).

To properly account for both flow separation and viscous shear stress effect, the computational cell close to the non-slip surface needs a sufficiently large resolution, especially for turbulent flow. To calculate the boundary layer thickness, first, we introduced a non-dimensional distance and velocity such as follow [15]:

$$y^+ = \frac{u^* y}{\nu} \quad (5.11)$$

$$u^* = \sqrt{\tau_w / \rho} \quad (5.12)$$

where u^* , τ_w , and ν , are the wall friction velocity, wall shear stress, and the fluid’s viscosity, respectively. The y^+ is a non-dimensional distance from the wall that divides the boundary layer regions into several sub layer:

- $y^+ < 5$: Viscous sub-layer. Flows are dominated by the fluid’s intrinsic viscosity, causing the flow to be streamlined and laminar
- $5 < y^+ < 30$: Buffer later. Flows are starting to be affected by the outer flow’s turbulence, but the viscous effect still dominates
- $30 < y^+ < 200$: Inertial sublayer or log law region. The turbulence effect becomes more apparent, and the velocity profile can be estimated by log function.
- $y^+ > 200$: Outer later. Flows are dominated by turbulence

The shear stress can be calculated by its relation to the skin friction coefficient and the skin friction coefficient approximation \bar{C}_f as follow [16]:

$$\bar{C}_f = \frac{2\tau_w}{\rho\bar{U}^2} \quad (5.13)$$

$$\bar{C}_f \cong \frac{0.066}{(\log R_e - 2.03)^2} \quad (5.14)$$

where R_e is the Reynold number, defined as $R_e = \rho\bar{U}L_x/\mu$. The first cell's centroid location can then be calculated Substituting eq. (5.12)-(5.14) into eq. (5.11) and choosing the appropriate value of y^+ that we want to resolves. In marine application without any significant flow separation, [13] suggested that the first cell height has to sufficiently resolve y^+ value of < 10 . The first cell height can then be determined to be twice the y value computed from eq. (5.12)-(5.14) with $y^+ = 10$ such as illustrated in Fig. 5.3.

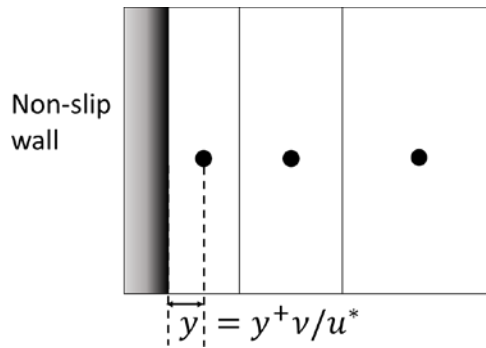


Fig. 5.3. First cell definition with regards to the computed y value

In marine applications, the viscous effect such as turbulence, skin drag, and vortex shedding provides significant additional forcing or damping. For example, in a ship roll resonance motion case where wave-making damping is small, the motion is largely affected by the viscous damping [6].

5.2.3. Volume of Fluid

In CFD, free-surface flow is considered as a non-mixing two-phase flow involving a sharp interface boundary between a heavy fluid (water) and light fluid (air). There are several ways of

treating the free surface (phase interface) in both Eulerian (e.g., the volume of fluid method) and Lagrangian (e.g., smoothed particle hydrodynamics) frame of reference. The Lagrangian approach typically has a straightforward interface definition and can deal with a violent free-surface flow with relative ease. However, this method typically requires a considerable computing effort since the resolution is typically kept the same throughout the domain (no local refinement) and that each computation point's position is changing at each time step [17]. Since we only consider quasi-steady flows with minimum breaking waves, the Eulerian approach is chosen to track the interface to reduce computation cost.

In the volume of fluid method, volume fraction $\alpha_i = \forall_i / \forall_{cell}$ is used to describe the distribution of phases and the location of the interface, with \forall_i defined as the volume of phase i that is located inside a cell with a volume of \forall_{cell} . The volume fractions of all phases in a cell must added up to 1. In two-phase fluid flow, the interface location is located where $\alpha_i = 0.5$ for any i . The volume fraction is also applied to the governing transport equation (5.1)-(5.3) as a multiplication factor.

The transport equation is then solved for only one of the phases in each cell, with the second phase variables are adjusted so that the sum of the volume fraction of all the phases equals one. A detailed description of the volume of fluid method can be found in [18].

This phase tracking approach requires the mesh resolution to be high enough in the interface region to resolve its position and shape, as illustrated in Fig. 5.4. Considering this limitation, free surface mesh refinement is needed to adequately capture the wave's height (H) and wavelength (λ). According to STAR-CCM+ guidelines, the typical value of $\lambda/dx = 80-120$ and $H/dz = 15-40$ is needed in the free surface region.

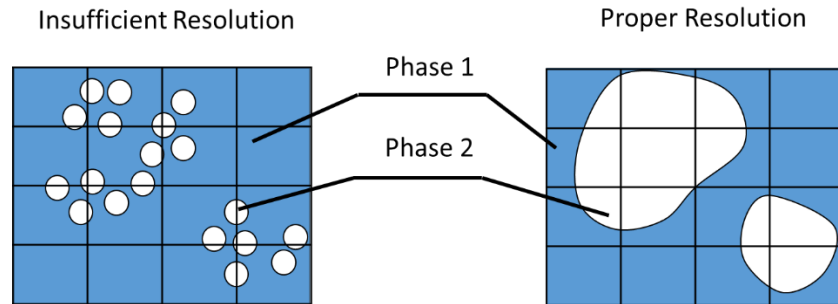


Fig. 5.4. Grid requirements in VOF method

5.2.4. Boundary and Initial Condition

There are five types of boundary condition that are used in this study:

- Velocity inlet:
Used for upstream, top, and side boundary conditions. The x-y-z velocity components are set to match specific values at this boundary.
- Symmetric plane:
Used at the horizontal half-plane of the computation domain. No normal direction velocity is allowed, while the other velocity components are mirrored to the other half-plane. By using this type of boundary condition, we can cut the computation domain to half (saving a large amount of computation cost).
- Pressure outlet:
Used for the downstream boundary condition. The pressure is set to match specific values. The velocity values need to be set as “extrapolated” for flows with a significant tangential velocity to the boundary. Furthermore, due to the periodic nature of the waves, backflow on this boundary is to be expected.
- No-Slip wall:

Used at the bottom boundary and ship's hull. No normal velocity direction is allowed in these boundaries. Furthermore, the boundary layer theory is applied to these boundaries depending on the cell resolution and outer flow conditions.

- **Overset mesh:**

Used at small control volume enclosing the hull and some part of the fluid domain. This boundary is used to communicate the field functions (velocity, pressure, etc.) calculated from the inner, freely moving, computation domain (foreground region) to the outer computation domain (background region) and vice versa. A more detailed explanation of the overset mesh can be found in the Overset Mesh sub-section.

The illustration of the boundary conditions in the present study's computation domain can be found in Fig. 5.5.

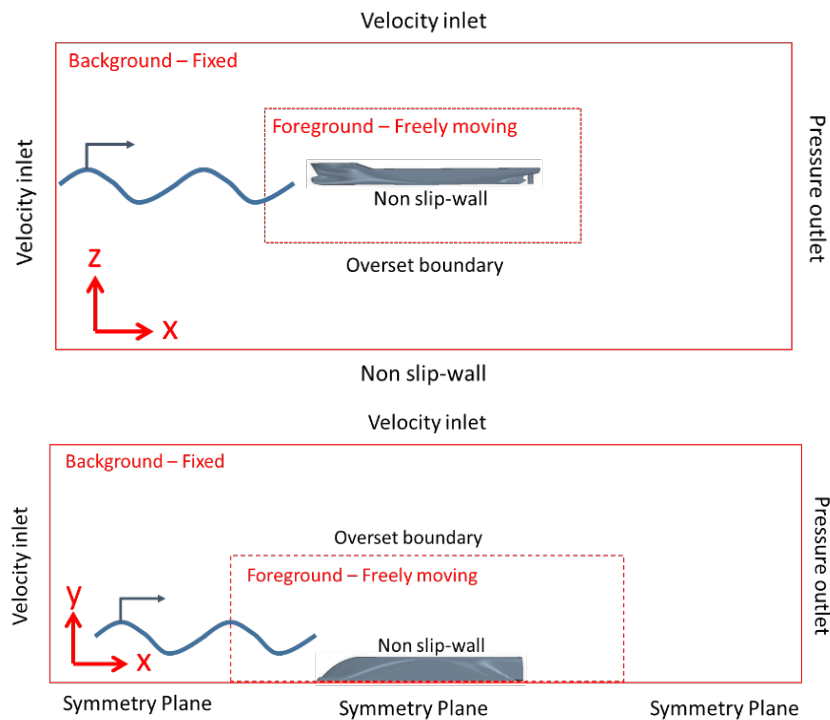


Fig. 5.5. Boundary conditions

Linear (Airy) wave's kinematics (free surface position) and dynamics (fluid's velocity and pressure) is used as the boundary and initial values throughout the fluids. The wave tank is set so that the deepwater condition is fulfilled $d/\lambda > 0.5$. Therefore, the initial and boundary conditions are:

$$u_x = A_w \omega_0 \cos(kx - \omega_0 t) e^{kz} \quad (5.15)$$

$$u_z = A_w \omega_0 \sin(kx - \omega_0 t) e^{kz} \quad (5.16)$$

$$\eta = A_w \sin(kx - \omega_0 t) e^{kz} \quad (5.17)$$

where the wave's related variables definition, including the dispersion relation, follows the previous chapters. The wave's steepness is chosen so that it always falls within the linear wave's theory limit of $H < 0.00625\lambda \tanh(2\pi h/\lambda)$.

The volume fraction of the fluid can be found from the sea level position η by employing the level set function [19] as follows:

$$\alpha_i = \alpha_1 H(\eta^*) + \alpha_2 (1 - H(\eta^*)) \quad (5.18)$$

$$H(\eta^*) = \begin{cases} 0 & \text{if } \eta^* < -\epsilon \\ \frac{1}{2} \left[1 + \frac{\eta^*}{\epsilon} + \frac{1}{\pi} \sin\left(\frac{\pi \eta^*}{\epsilon}\right) \right] & \text{if } |\eta^*| < \epsilon \\ 1 & \text{if } \eta^* > \epsilon \end{cases} \quad (5.19)$$

where $\eta^* = (\eta - z)$ and $\epsilon = 1.6dz$.

5.2.5. Wave Forcing Zone

Even though the boundary values are set to follow the linear wave's field values, it is only enforced at the boundary location. Because of this, the wave's reflection and flow discontinuity can still occur, especially at the pressure outlet and velocity inlet. To avoid this phenomenon, the wave forcing zone is introduced. The wave forcing zone enforced the momentum equation

(velocity values) over a bounded region of the computational domain to follow the predefined theoretical values by using the Euler overlay method [20]. In the Euler overlay method, the following additional forcing term is added to the momentum conservation equation:

$$q_\phi = -\gamma_{wz}\rho(\phi - \phi^*) \quad (5.20)$$

where q_ϕ , γ_{wz} , ϕ , and ϕ^* is the momentum forcing term, forcing coefficient, current solution of the transport equation, and predefined theoretical value which the solution is forced towards. The forcing coefficient γ_{wz} is chosen to be monotonically increasing from the edge of the wave forcing zone to its maximum value at the boundary. In STAR-CCM+, the cosine function is used as the forcing coefficient:

$$\gamma_{wz} = -\gamma_0 \cos^2\left(\frac{\pi x}{2L_{wz}}\right) \quad (5.21)$$

where γ_0 and L_{wz} is the wave forcing coefficient and wave zone distance from the boundary, respectively. Depending on the length of the wave zone and the flow characteristics, typically, γ_0 is chosen to be a large value ($\gamma_0 > 10$). We found that when the wave zone distance is set to be $L_{wz} < 2\lambda$, the waves with smaller wavelength require higher γ_0 compared to that of a longer wavelength. In this study, L_{wz} is chosen to be $\lambda < L_{wz} < 2\lambda$ at the downstream boundary and $0.5\lambda < L_{wz} < \lambda$ at the upstream and side's boundary, and $50 < \gamma_0 < 150$ is used.

5.2.6. Overset Mesh and Dynamic Fluid-Body Interaction

Overset mesh (also called the chimera grid method) is used to discretize the computational domain with several different meshes that overlap each other in an arbitrary manner [16]. Because the mesh regions are independent with each other, the overset method is suitable for problems with large relative motions without the need to regenerate the mesh throughout the whole computation

domain. With this method, only local mesh cutting and regeneration around the enclosed foreground region is needed (see Fig. 5.5 for the definition of foreground region). Furthermore, the majority of overlapping meshes are only solved in the foreground region, while the same mesh in the background region is excluded in the calculation through mesh hole cutting. There are three distinct cell type on the overset mesh method:

- Active cells: Cells where the governing equations are solved.
- Passive cells: Cells where no equations are solved. These cell type is excluded from the background mesh through a hole cutting procedure
- Donor cells: Cells on the overset boundaries which are used to provide interpolation information to the other mesh acceptor cell.
- Acceptor/ghost cells: Cells on the overset boundaries which receives interpolated information from the other mesh donor cells.

For each acceptor cell, there are typically four donor cells that are used to provide the interpolated values to the other mesh. The information exchange between the donor and acceptor cells ensures the continuity and conservation between the meshes. The hole cutting region and cell type in a typical sea keeping analysis set up can be found in Fig. 5.6, while detail information and formulations used in the overset mesh can be found in [21].

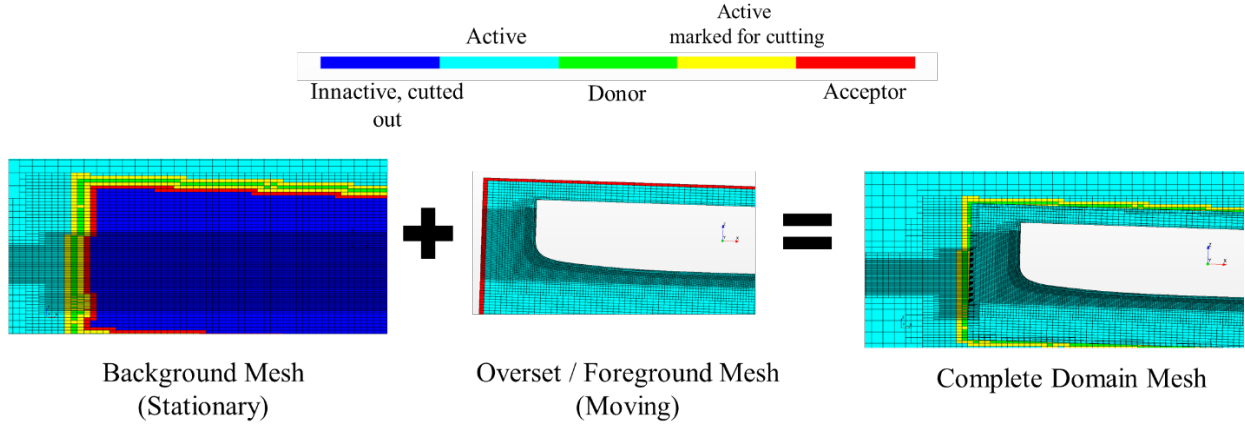


Fig. 5.6. Overset mesh cell type

The Dynamic Fluid Body Interaction (DFBI) models solve for the rigid-body motion of an object exposed to surface forces (e.g., shear and pressure from fluid) as well as body forces (e.g., gravity). DFBI calculates the resultant moment and forces acting on the selected wall boundaries and then updated the body's new position at each inner iteration step until convergence is reached. The equation of motion for translation degree of freedom can be found on eq.(5.22), while the rotation degree of freedom can be found on eq.(5.23).

$$m \frac{\partial v}{\partial t} = \mathbf{F} \quad (5.22)$$

$$\mathbf{I} \frac{\partial \boldsymbol{\omega}}{\partial t} + \boldsymbol{\omega} \times \mathbf{I} \boldsymbol{\omega} = \mathbf{M} \quad (5.23)$$

where m is the body mass, \mathbf{I} is the moment of inertia tensor, and $\boldsymbol{\omega}$ is the rotation vector. The external force vector \mathbf{F} and moment vector \mathbf{M} is calculated by integrating the stresses over the body's surface. Combined with the overset mesh, the DFBI solver provides a robust tool to solve the fully non-linear fluid-body interaction.

For steady flow analysis such as towing tank simulation, the motion solver can be frozen for several time steps until the predetermined convergence criteria are met. After that, the body is moved to a new position, and the same step is repeated until the change of the body's position is

negligible. This quasi-static approach can significantly reduce computation cost in the steady flow analysis and was used in our uniform-flow only simulation.

5.2.7. *Time Stepping Considerations*

A second-order implicit unsteady scheme is recommended for free surface flow with a sharp interface [7]. The stability Courant–Friedrichs–Lewy (CFL) stability requirement of the second-order scheme is higher compared to that of the first order. However, it can properly propagate the free surface with minimum numerical dissipation. The following time-stepping criteria are used to reduce the cost of the computation while maintaining numerical stability:

1. Stopping the inner iteration within one time step and go to the next time step when one of the following conditions are met:
 - Volume fraction residual < 0.001 .
 - Momentum residual < 0.001 .
 - Continuity residual < 0.1 .
 - 15 iteration is reached.
2. Setting reference / initial time step value to be the minimum value of the following criteria:
 - a. $\Delta t = T/(4.8N_x)$: To properly capture the wave's behavior at each period. Where T is the wave's period, and N_x is the number of cells per wavelength
 - b. $\Delta t = 0.5\Delta x_{min} \max(C_g, [U + |\mathbf{v}|])$: from CFL requirement to restrict the flow so that in only propagates half the smallest cell size (Δx_{min}). Where C_g is the wave's group velocity, U is the uniform flow speed, and $|\mathbf{v}|$ is the magnitude of the wave's particle velocity.

- The built-in automatic adaptive time step is set to keep the maximum instantaneous CFL number to be < 0.54 . The minimum allowable time step is set to be $1/10^3$ of the reference time step from point number 2.

5.2.8. Computational Domain and Meshing Considerations

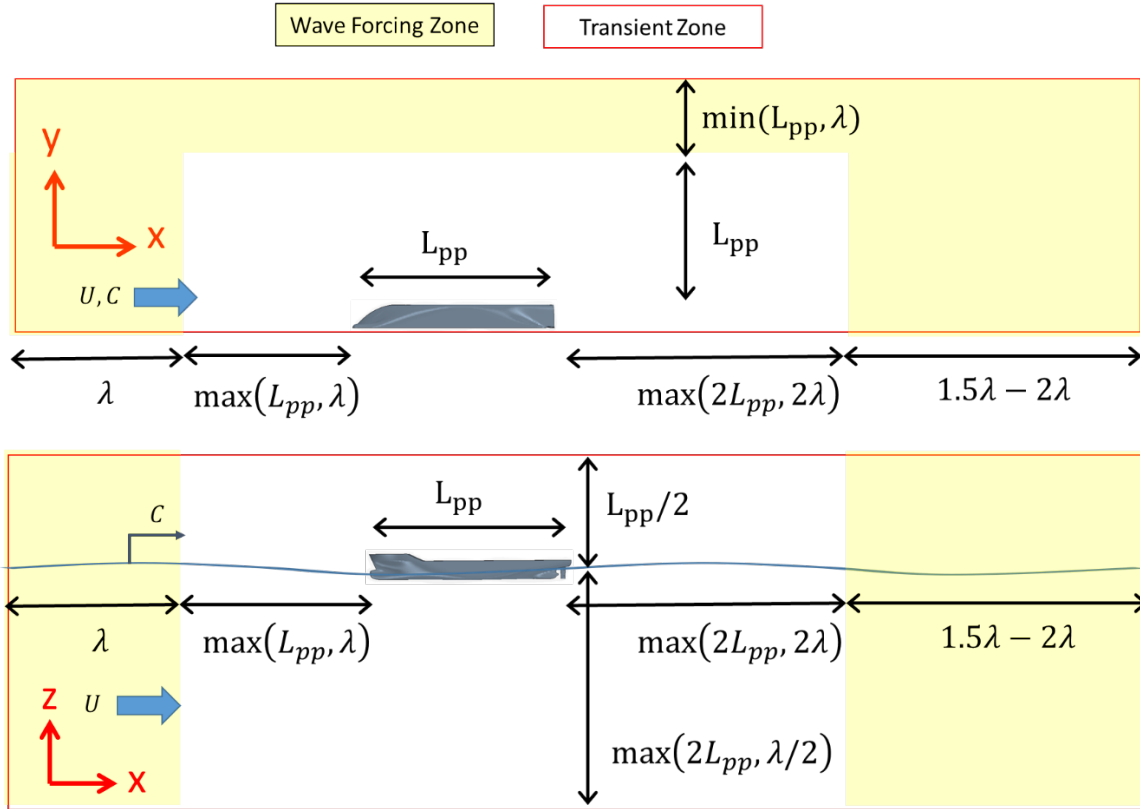


Fig. 5.7. Computational domain

The computation domain needs to be large enough to incorporate the wave forcing region without significantly changing the free surface profile close to the body. Furthermore, it needs to be large enough so that the body's local flow field perturbation does not reach the boundaries to avoid reflection. The water depth also needs to be deep enough ($d > 0.5\lambda$) so that deep water assumption can be maintained. However, the computation domain needs to be kept as small as

possible to reduce the computational cost. Considering all of the above, the computation domain size is kept at a particular ship's and wave's length ratio, as illustrated in Fig. 5.7.

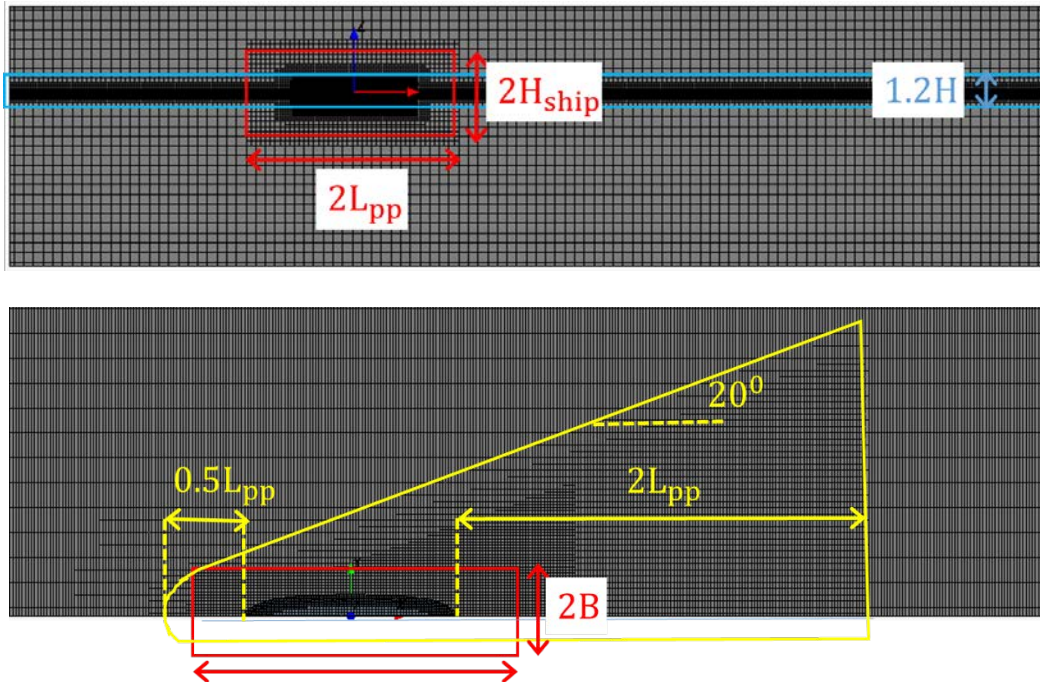


Fig. 5.8. Mesh refinement regions

To properly capture the free surface and non-linear body motion, mesh refinements are applied to certain vital regions, as shown in Fig. 5.8. In summary, each of the mesh refinement regions objectives is:

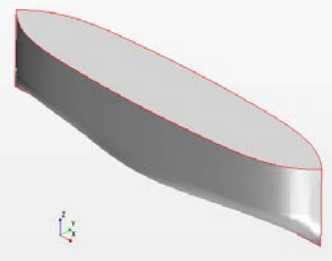
- Free surface refinement (blue line): To adequately capture the incoming, diffracted, and radiated wave's interface. Since the body is streamlined in the head seas condition, the refinements are only done in x and z directions (see VoF subsection for details).
- Wake refinement (yellow line): To adequately capture the steady ship waves (Kelvin wave). Since the waves are radiated outward from the body with 20° angle, the refinements are done in x and y direction, while the z refinement follows the free surface refinement

- Near overset boundary refinement (red line): To provide sufficient interpolation cells for the overset mesh and to resolve local perturbation such as the bow and stern waves and wave run-up close to the body (see overset and VoF subsection for details).

5.3. Case Definition

Modified blunt Wigley hull as defined in Table 5.1. This hull is similar to the blunt Wigley hull used in [22] with a 1:2 Froude scaling ratio. Furthermore, the hull is extended vertically upward from the water line to reach the desirable total depth so that the wave's run-up can be properly accounted. To validate all of the body's input (e.g., displaced volume, inertia, the center of gravity), we first did the hydrostatic test with a freely floating body. The body's input is considered correct when the body is at the equilibrium position, e.g., no pitch or heave motion (or static offset) is observed. Note that since we use a symmetric computation domain, all the mass properties need to be halved, while all the resulting forces need to be multiplied by two. We also need to calibrate the wave's height so that the comparison with other methods can be appropriately made. This calibration is done by simulating the waves without the presence of the body.

Table 5.1. Hull's particulars

Hull Shape	Item	Notation	Value	Unit
	Length	L	5	m
	Breadth	B	1	m
	Total Depth	h_{bm}	0.85	m
	Draft	d	0.35	m
	Displaced Volume	∇	1.109	m^3
	Vertical CoG	KG	0.062	m
	y - Radii of Gyration	r_{yy}/L	0.236	m

The wave's slope of $H/\lambda = 0.03$ is chosen to match the experiment condition [22]. Three wave's length condition is simulated, the first, $\lambda/L = 2$ is the long wave condition that is far from any resonance or cancellation frequency (i.e., easier to simulate), $\lambda/L = 1.25$ is the pitch resonance condition (in the case of $F_n = 0.2$, according to BEM simulation) to see the large amplitude motion effect on the dynamics. Lastly, $\lambda/L = 1.1$ is the maximum added resistance load condition according to Kashiwagi's experiment [22]. In these simulations, the body is fixed in the surge direction, but allowed to move in the pitch and heave direction, similar to the towing tank experiment with waves. A fixed body (diffraction only) simulation is also simulated for the $\lambda/L = 2$ case to validate our simulation. Since shorter waves requires higher resolution but smaller total domain size, three type of tanks are created to reduce the computation cost. All the simulated cases can be seen in Table 5.2.

Table 5.2. Case definitions

Case Name	F_n	H (m)	λ (m)	T_e (sec)	Body	Wave Tank
Tow	0.2	N/A	N/A	N/A	Yes	Tank0
Wave1_Only	0.0	0.3	10	2.53	No	Tank1
Wave1_Mot0	0.0	0.3	10	2.53	Yes	Tank1
Wave1_MotU	0.2	0.3	10	1.87	Yes	Tank1
Wave2_Only	0.0	0.1875	6.25	2.00	No	Tank2
Wave2_Mot0	0.0	0.1875	6.25	2.00	Yes	Tank2
Wave2_MotU	0.2	0.1875	6.25	1.38	Yes	Tank2
Wave3_Only	0.0	0.1875	5.5	1.88	No	Tank2
Wave3_Mot0	0.0	0.1875	5.5	1.88	Yes	Tank2
Wave3_MotU	0.2	0.1875	5.5	1.27	Yes	Tank2

5.4. Results and Discussion

5.4.1. Wave Height Calibration

Wave height calibration is done to record the simulated wave height at the ship's center of gravity location to be used as the non-dimensionalization factor. The recorded sea-level elevation and the corresponding wave's height can be found in Fig. 5.9 and Table 5.3 Recorded wave's height and period for each of λ/L cases, respectively. The wave's height is calculated by zero crossing method and then averaging them over several wave's cycles (>5 cycles). The smaller simulated wave's height compared to the target wave's height does not cause complication as long as the wave's height is stable and target wavelength (therefore, period) is achieved. As can be seen from the figures, these conditions are successfully achieved.

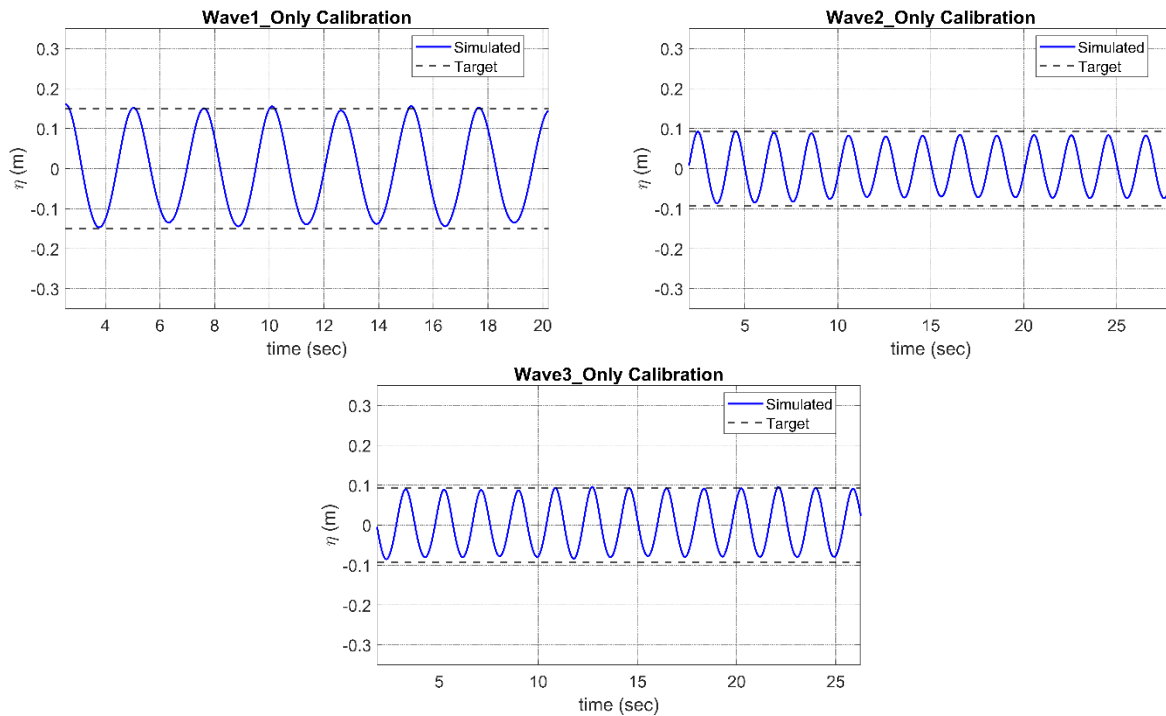


Fig. 5.9. Calibration of the simulated wave's height and period.

Table 5.3. Recorded wave's height and period for each of λ/L cases

Case	H (m)			T (sec)		
	Simulated	Target	Diff.	Simulated	Target	Diff.
Wave1_Only	0.289	0.3	-4%	2.53	2.53	0%
Wave2_Only	0.162	0.1875	-13%	2.00	2.00	0%
Wave3_Only	0.171	0.1875	-9%	1.88	1.88	0%

5.4.2. Uniform Flow Problem

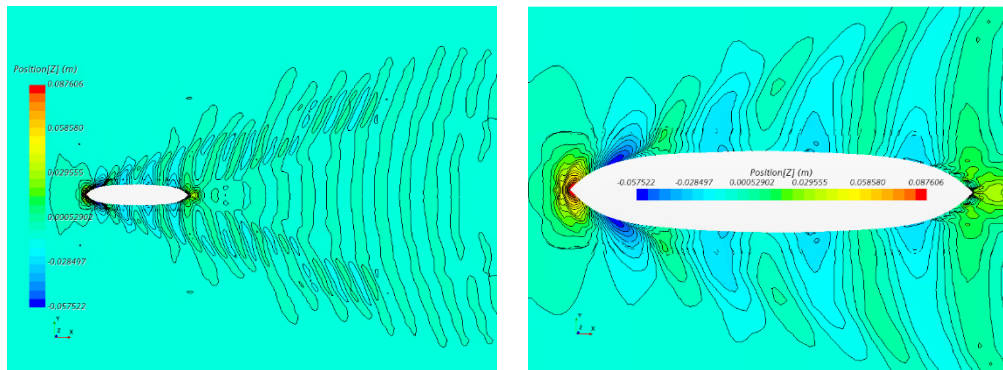


Fig. 5.10. Steady waves (Kelvin-ship wave) pattern illustration (Tow Case)

Towing tank (uniform flow simulation without waves) simulation is done to see the uniform flow effect on the steady wave's pattern (Fig. 5.10) and the corresponding run up along the hull (Fig. 5.11). As expected, the diverging Kelvin ship waves at $\sim 19^\circ$ angle from the ship's hull along with the transverse waves is observed. From Fig. 5.10, we can see that the sea surface elevation at the bow is larger than that of the stern, which confirms that this might cause discrepancies in our hydroelectricity analysis close to the bow in Chapter 3. The difference in the steady wave run-up elevation between the bow and the stern coupled with the dynamic pressure caused a steady sinkage and trim on the ship, which can be seen in Table 5.4.

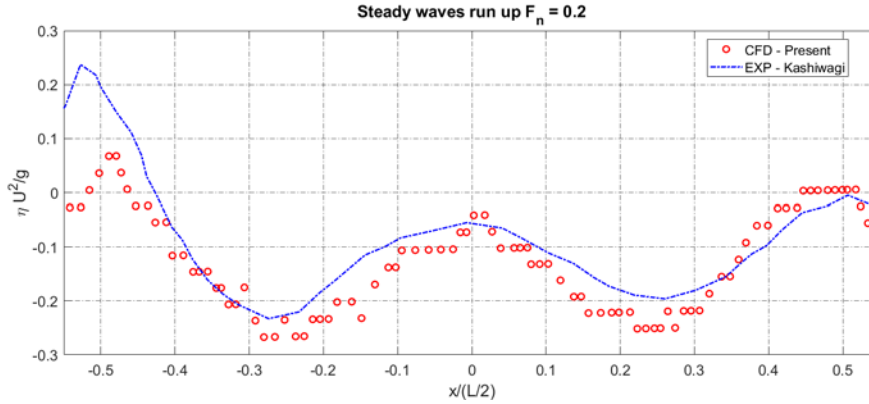


Fig. 5.11. Steady waves run up along the Wigley hull. Experiment result is from ref.[22]

Table 5.4. Steady displacements

Trim (Pitch)	0.128°
Sinkage (Heave)	0.01851m

A comparison with Kashiwagi [22] experiment shows that the wave's run-up along the hull agrees well with the present CFD method. Minor discrepancies can be found in the bow that was caused by the method in which the wave's run-up position is extracted from the simulation results, which was done manually. Confirming that all of the essential phenomena of the steady flow problem were properly captured, we can then confidently incorporate waves into our simulation.

5.4.3. Wave and Uniform Flow Interaction Problem

Both waves only problem and waves-uniform flow interaction problem was simulated in this section. The resulting wave's pattern for the unrestricted heave-pitch degree of freedom simulation can be seen in Fig. 5.12. From the waves only problem, we can clearly see the radiating waves because of the heave and pitch motion that is moving outwards from the hull. The diffracted wave cannot be clearly seen since the hull is slender, and the wave is coming from the head seas direction. On the other hand, we can see that the wave's pattern in the case with the uniform flow

is highly affected by the flow. Both maxima and the minima of the wave's height were both increased due to the uniform flow.

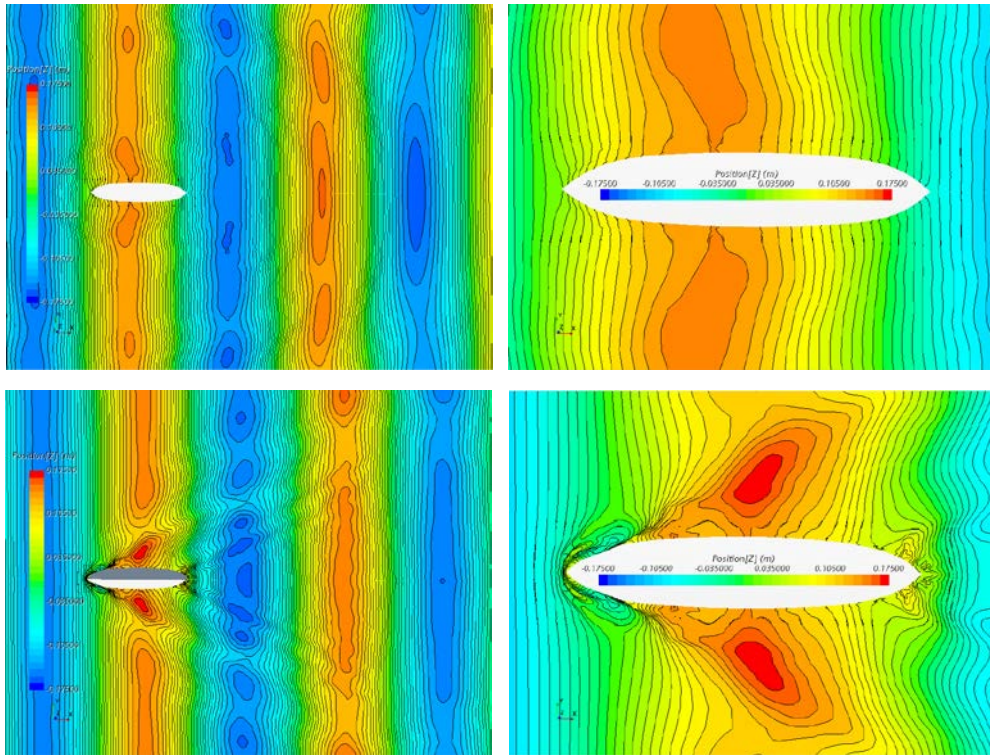


Fig. 5.12. Wave's profile when the body is at the wave's peak for $\lambda/L = 2$, without (top) and with uniform flow (bottom) effect

The forces and moment time-series validation for a fixed body (diffraction problem) is shown in Fig. 5.13. The experiment (Kashiwagi, [22]) and the BEM time series are reconstructed from the frequency domain results using simple sinusoidal functions. From the figure, we can see that both the amplitude and the frequency of the current CFD model matched well with the experiment. In the case with forward speed, the encounter frequency effect is observed, and the force increase due to additional convective pressure is also observed. Small non-linearities can be seen in the CFD results where their profile does not match precisely with sinusoidal functions (sharper peaks and milder slopes).

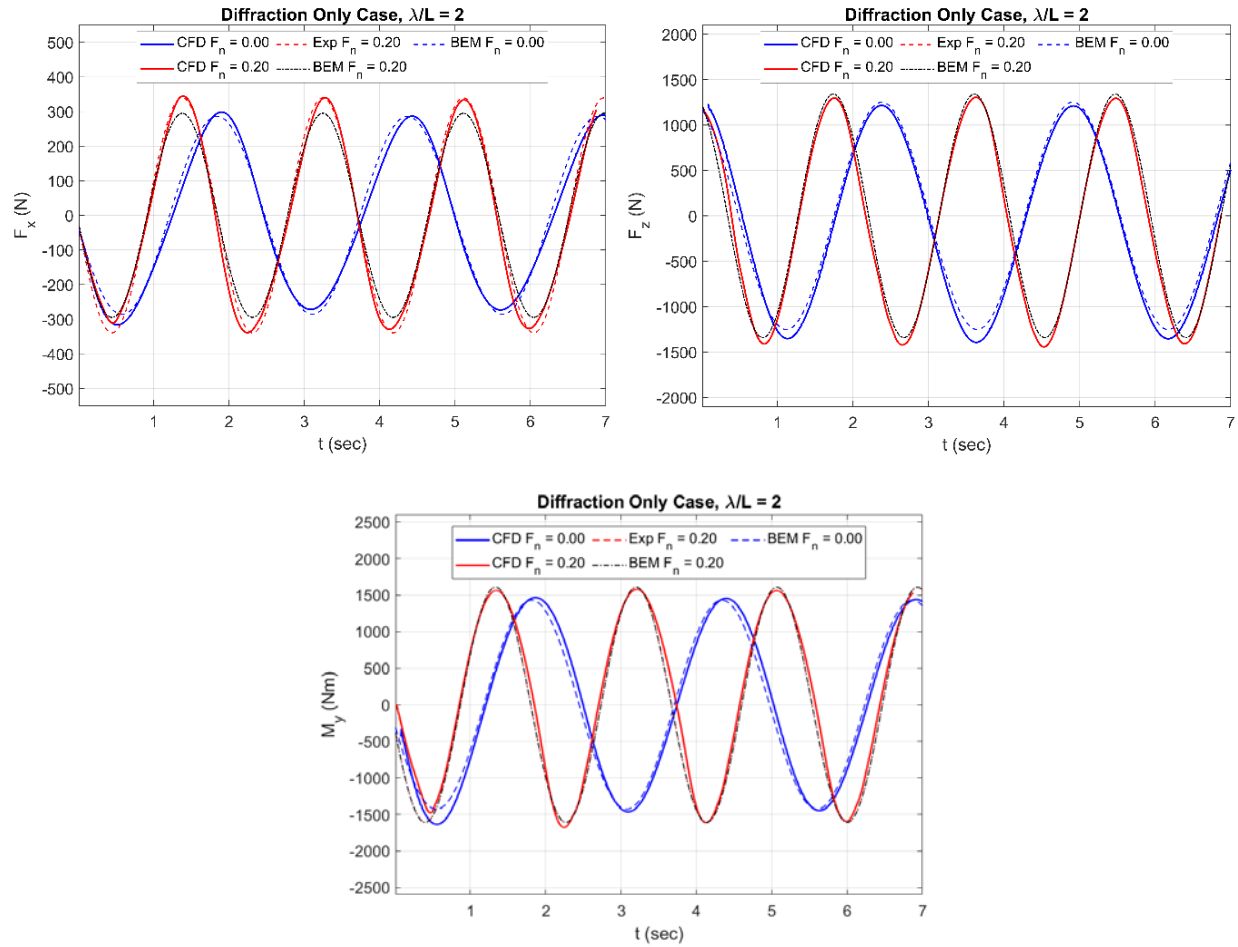


Fig. 5.13. Forces and moment time series for $\lambda/L=2$. Experiment result is from ref.[22]

The ship's pitch and heave motion are compared against the experiment and BEM simulation in Fig. 5.14. The results show a good agreement with both the BEM and the experiment, except for the $\lambda/L = 1.25$ case with $F_n = 0.2$. The reason for this discrepancies is that when resonance motion is excited (i.e., $\lambda/L = 1.25$, based on the BEM analysis in Chapter 1), the problem becomes more complicated. Because of the large pitch motion, non-linearity in the form of impact loading and breaking waves occurs, as shown in Fig. 5.15-Fig. 5.16. this non-linearity is not considered in the BEM method but is well documented in the experiment [22]. Kashiwagi also stated that these phenomena caused the added resistance experiment data to be widely spread close to the resonance frequency.

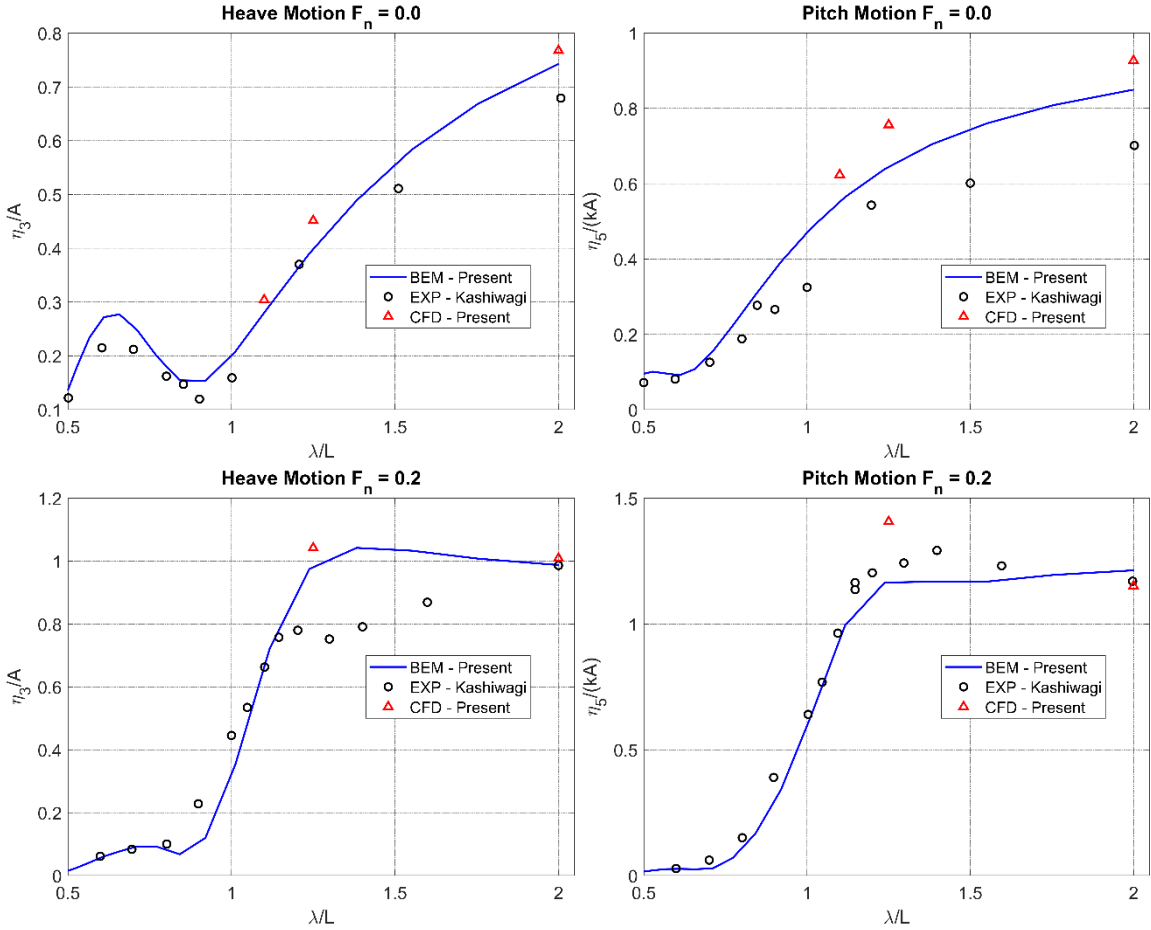


Fig. 5.14. Motion comparisons between the present CFD simulation with the present BEM method and experiment results from ref.[22]

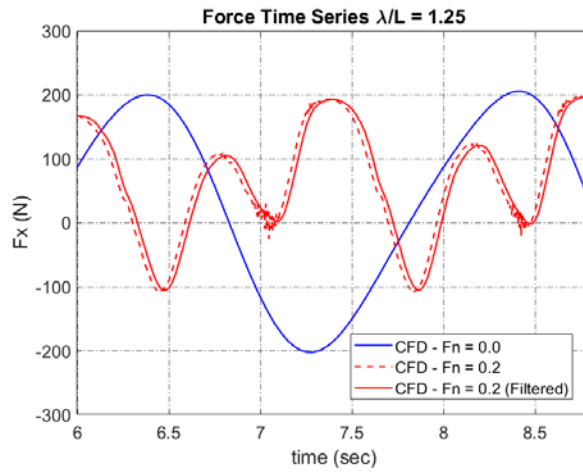


Fig. 5.15. Non-linearity in surge force time series for unrestrained heave and pitch for $\lambda/L=1.25$ (pitch and heave resonance frequency)

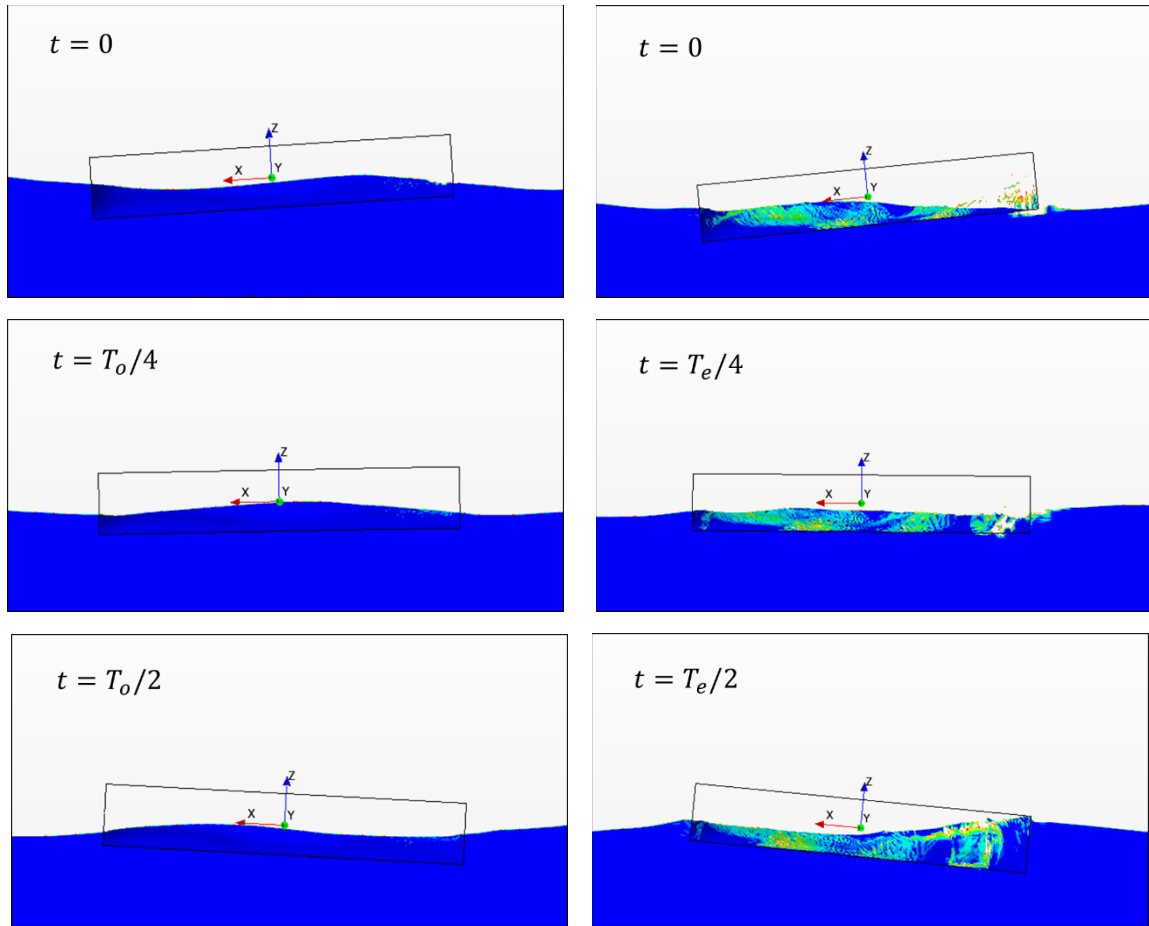


Fig. 5.16. Motion visualization comparison between wave only case (left) and wave with uniform flow case (right) for $\lambda/L = 1.25$

Despite the highly non-linear nature of the problem, the CFD simulation was able to capture all the essential dynamics properly. This claim is strengthened by comparing the slowly varying non-linear force in the form of added resistance of the current CFD model against the experiment and BEM results in Fig. 5.17-Fig. 5.18. The added resistance is calculated by time-averaging the surge force time series over several cycles after the quasi-static state is reached. From these results, we see that the current CFD results compare well with both the BEM and experiments.

Even though the CFD simulation was able to capture all the non-linear interactions, it requires a very high computation cost. For illustration, in the case of highly non-linear physics (e.g.,

breaking waves), 100 CPU hours typically only yield 0.5 sec of simulation time. Therefore, the BEM method is still preferred in many engineering practices. The results from the BEM can serve as a benchmark to choose cases with high non-linearity or viscous effect (e.g., close to resonance frequency), to be simulated with the CFD method.

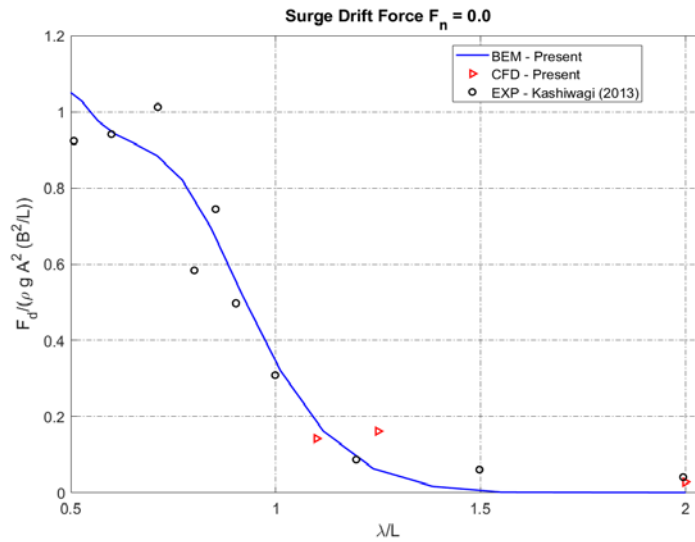


Fig. 5.17. Surge drift force for $F_n = 0.0$ case. Experiment result is from ref.[22]

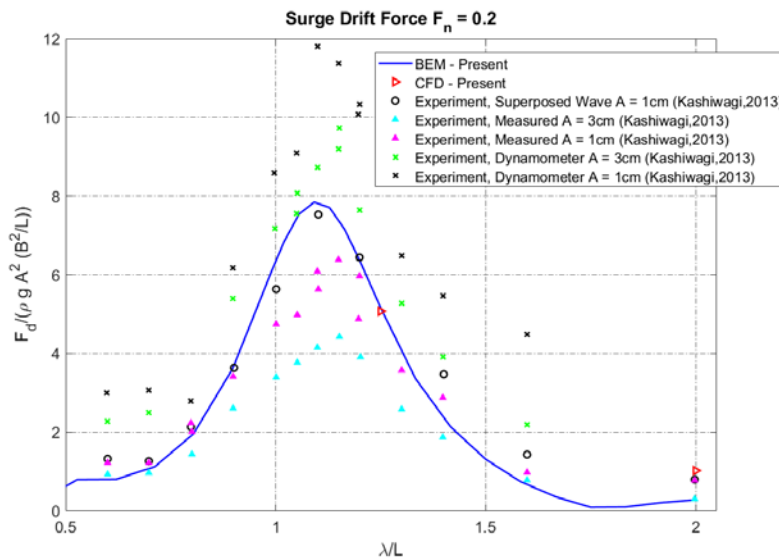


Fig. 5.18. Surge drift force for $F_n = 0.2$ case. Experiment result is from ref.[22]

5.5. Conclusion

RANS based CFD simulation was conducted for theoretical Wigley hull shape to reproduce the real flow condition with minimum simplifications. The Step-by-step set up of the model was explained to ensure the reproducibility of the model. Several quality assurances, including static wave tank, wave only case, and steady towing simulation, were also conducted to ensure the model's fidelity before wave excitation can be introduced to the model.

The CFD results for both zero and non-zero current simulations show a good agreement with either the BEM method (with UF approximation) or the experiment results. Highly non-linear dynamics involving wave's breaking and large motions are observed for $\lambda/L = 1.25$ with $F_n = 0.2$ case due to pitch resonance. CFD simulation was also able to capture the second order mean drift loading successfully. Even though the CFD simulation was able to capture all the non-linear interactions, it requires a very high computation cost. On the contrary, the BEM shows comparable results, with significantly less computational cost.. Therefore, in most cases, BEM is proven to be the more reliable tool, except for several special cases (i.e., at resonance frequency). Therefore, the BEM can be used as a guide in choosing these special cases to be simulated with CFD so that the computation requirement in solving the completely non-linear simulations can be decreased.

5.6. References

- [1] S. J. Kim and W. Koo, "Development of a three-dimensional fully non-linear potential numerical wave tank for a heaving buoy wave energy converter," *Mathematical Problems in Engineering*, vol. 2019, no. i, 2019.
- [2] J. Jiao and S. Huang, "CFD simulation of ship seakeeping performance and slamming loads in Bi-directional cross wave," *Journal of Marine Science and Engineering*, vol. 8, no. 5, pp. 1-24, 2020.
- [3] H. Bandringa and J. A. Helder, "On the Validity of CFD for Simulating Extreme Green Water Loads," in *39th International Conference on Ocean, Offshore & Arctic Engineering*, Virtual, Online, 2020: OMAE

- [4] N. F. Heilskov and O. S. Petersen, "Non-Linear 3D Hydrodynamics of Floating Wind Turbine Compared Against Wave Tank Tests," Busan, South Korea, 2016, pp. 1-14: OMAE2016.
- [5] K. Arjen *et al.*, "Development and Verification of Modeling Practice for CFD Calculations to Obtain Current Loads on FPSO," *39th International Conference on Ocean, Offshore & Arctic Engineering*, pp. 1-9, 2020.
- [6] M. A. R. Irkal, S. Nallayarasu, and S. K. Bhattacharyya, "CFD approach to roll damping of ship with bilge keel with experimental validation," *Applied Ocean Research*, vol. 55, pp. 1-17, 2016.
- [7] J. T. Vigsnes, "Seakeeping Analysis Comparison Between Viscous And Inviscid CFD Joakim Tveiten Vigsnes," 2018.
- [8] Y. Jin, S. Chai, J. Duffy, C. Chin, and N. Bose, "URANS predictions of wave induced loads and motions on ships in regular head and oblique waves at zero forward speed," *Journal of Fluids and Structures*, vol. 74, pp. 178-204, 2017.
- [9] H. Orihara, "Comparison of CFD simulations with experimental data for a tanker model advancing in waves," *International Journal of Naval Architecture and Ocean Engineering*, vol. 3, no. 1, pp. 1-8, 2011.
- [10] H. Islam, M. Rahaman, and H. Akimoto, "Added Resistance Prediction of KVLCC2 in Oblique Waves," *American Journal of Fluid Dynamics*, vol. 9, no. 1, pp. 13-26, 2019.
- [11] H. Sadat-Hosseini, P. C. Wu, P. M. Carrica, H. Kim, Y. Toda, and F. Stern, "CFD verification and validation of added resistance and motions of KVLCC2 with fixed and free surge in short and long head waves," *Ocean Engineering*, vol. 59, pp. 240-273, 2013.
- [12] C.-s. Wu, D.-c. Zhou, L. Gao, and Q.-m. Miao, "CFD computation of ship motions and added resistance for a high speed trimaran in regular head waves," *International Journal of Naval Architecture and Ocean Engineering*, vol. 3, no. 1, pp. 105-110, 2011.
- [13] B. Bouscasse, A. Bockman, and G. Ducrozet, "Development of A Protocol to Couple Wave and CFD Solvers Towards Potential Wave Kinematic Solver," Virtual, Online, pp. 1-8: OMAE2020.
- [14] D. C. Wilcox, *Turbulence Modeling for CFD*, 2nd ed. La Canada, California: DCW Industries, 1998.
- [15] F. M. White, *Viscous fluid flow*, 3rd ed. New York: McGraw-Hill, 2006.
- [16] C. D. Adapco, "STAR CCM+ Users Manual. <http://www.cd-adapco.com/products/star-ccm>," ed, 2020.

- [17] F. P. Bakti, M. H. Kim, J. C. Park, and K. S. Kim, "Comparative study of standard WC-SPH and MPS solvers for free surface academic problems," *International Journal of Offshore and Polar Engineering*, vol. 26, no. 3, pp. 235-243, 2016.
- [18] S. Muzaferija and M. Peric, "Computation of free-surface flows using interface-tracking and interface- capturing methods," 2017.
- [19] H. Bihs, A. Kamath, M. Alagan Chella, A. Aggarwal, and Ø. A. Arntsen, "A new level set numerical wave tank with improved density interpolation for complex wave hydrodynamics," *Computers and Fluids*, vol. 140, pp. 191-208, 2016.
- [20] J. Kim, J. O'Sullivan, and A. Read, "Ringing analysis of a vertical cylinder by Euler overlay method," Rio de Janeiro, Brazil, 2012, vol. 4, pp. 855-866: OMAE2012.
- [21] H. Hadzic, "Development and Application of a Finite Volume Method for the Computation of Flows Around Moving Bodies on Unstructured , Overlapping Grids," 1, 2005.
- [22] M. Kashiwagi, "Hydrodynamic study on added resistance using unsteady wave analysis," *Journal of Ship Research*, vol. 57, no. 4, pp. 220-240, 2013.

6. GENERAL CONCLUSIONS

An in-house linear wave-current interaction simulation tool is developed by considering UF approximation in the frequency domain - 3D BEM framework. An in-house program originally developed for a linear zero speed wave diffraction-radiation problem was used as a base. The program is then extended to include the source formulation to calculate velocity more accurately and also extended to include the linear wave-current interaction effect.

The linear UF wave-uniform flow interaction model was proven to be robust enough to solve typical fluid-structure interaction problems, especially when the structure is considered to be slender. The UF approximation was also proven to be straightly applicable to any BEM simulation tools since all interaction terms were reduced to correction terms obtained from zero uniform speed simulation. Due to the ease of implementation in the linear problem, there are still rooms for this method to be applied to a broader range of problems.

In the third chapter, a multi-body uniform-flow-based wave-current interaction hydrodynamic model was developed. Coupled with the DMB (Discrete-Module-Beam)-based hydro-elasticity method, the aforementioned model can be used as a practical and efficient numerical tool for the hydro-elastic analyses with forward-speed effect. The developed model shows comparable results with more exhaustive methods. The developed model also successfully captured the increase of elastic responses and bending moments by forward speed, especially due to the resonance at the first bending mode. Several parametric studies were conducted to show the forward speed effect on the elastic behavior of the structure, and several key findings were found as follow:

- The forward speed effect (up to $F_n = 0.3$) on the natural period and mode shape was nontrivial at the first bending mode but negligible at higher bending modes.
- The maximum dynamic bending moment occurred at the mid-ship section when $\lambda \gg 0.5L$. However, when $\lambda < 0.5L$, higher elastic modes can be excited to change the location of the maximum bending moment.
- The increase of bending moments with a forward speed in the operational sea was more pronounced than the swell sea because of the encounter frequencies getting close to the first bending resonance.
- Modification to local elasticity parameter was straightforward, as shown by damaged hull case.

In the fourth chapter, an efficient method to compute second-order difference-frequency wave loads in the presence of uniform flow in the frequency domain was presented. From our numerical results, it is seen that the uniform flow has a significant influence on both the difference frequency quadratic and diffraction forces. Both the main-diagonal and off-diagonal parts of the difference frequency force QTFs were affected by the uniform flow, and the uniform flow generally increased the total force magnitudes and slopes. The uniform flow also shifted the QTF-peak locations, mainly due to the encounter-frequency effect. The comparison results with other approximations, such as the Aranha's added resistance method and Newman's QTF approximation, further emphasize the importance of the presently developed practical approach incorporating simplified but essential features of the uniform flow effects on difference-frequency force QTFs.

In the fifth chapter, RANS based CFD simulation was conducted for theoretical Wigley hull shape to reproduce the real flow condition with minimum simplifications. The CFD results for both zero and non-zero current simulations show a good agreement with either the BEM method (with UF approximation) or the experiment results. The CFD simulation was able to capture the

non-linear dynamics involving breaking waves and large motions that are not considered in the potential theory based-3D BEM. However, because of the very high computation cost associated with the CFD method, the BEM simulation results is still needed to provide the information on which specific cases need to be simulated.

In summary, the presently developed UF approximation model to account for the wave-current interaction showed a promise to be a highly efficient, practical tool to solve complicated problems. These problems include the currently presented hydro-elasticity problem with forward speed and the second-order slowly varying force under small uniform flow. Nonetheless, due to several pragmatic approximations, care should be exercised when applying the proposed method, especially when the steady free surface effect is not negligible (e.g., local dynamics close to the bow), the hull shape is not slender, uniform flow speed is large, or in the case of second-order sum-frequency wave loadings.